

Master's Thesis : Image-based mechanical analysis of tendon-to-bone attachment

Auteur : Volders, Tim

Promoteur(s) : Ruffoni, Davide

Faculté : Faculté des Sciences appliquées

Diplôme : Master en ingénieur civil biomédical, à finalité spécialisée

Année académique : 2019-2020

URI/URL : <http://hdl.handle.net/2268.2/10895>

Avertissement à l'attention des usagers :

Tous les documents placés en accès ouvert sur le site le site MatheO sont protégés par le droit d'auteur. Conformément aux principes énoncés par la "Budapest Open Access Initiative"(BOAI, 2002), l'utilisateur du site peut lire, télécharger, copier, transmettre, imprimer, chercher ou faire un lien vers le texte intégral de ces documents, les disséquer pour les indexer, s'en servir de données pour un logiciel, ou s'en servir à toute autre fin légale (ou prévue par la réglementation relative au droit d'auteur). Toute utilisation du document à des fins commerciales est strictement interdite.

Par ailleurs, l'utilisateur s'engage à respecter les droits moraux de l'auteur, principalement le droit à l'intégrité de l'oeuvre et le droit de paternité et ce dans toute utilisation que l'utilisateur entreprend. Ainsi, à titre d'exemple, lorsqu'il reproduira un document par extrait ou dans son intégralité, l'utilisateur citera de manière complète les sources telles que mentionnées ci-dessus. Toute utilisation non explicitement autorisée ci-avant (telle que par exemple, la modification du document ou son résumé) nécessite l'autorisation préalable et expresse des auteurs ou de leurs ayants droit.

UNIVERSITY OF LIEGE
FACULTY OF APPLIED SCIENCES



IMAGE-BASED MECHANICAL ANALYSIS OF TENDON-TO-BONE ATTACHMENT

Master thesis conducted by

TIMOTHY VOLDERS

with the aim of obtaining the degree of Master in Biomedical Engineering

SUPERVISOR:

Davide Ruffoni

PHD STUDENT SUPERVISOR :

Alexandra Tits

Liesbet Geris Jean-François Kaux Cédric Schwartz

ACADEMIC YEAR 2019-2020

Abstract

The attachment between soft and hard tissues such as tendon and bone, also called the enthesis, exhibits multiple gradients in composition, structure and mechanical properties. This project is focused on the attachment of the Achilles tendon to the calcaneus bone. Specifically, the bone side of the interface is studied.

Multiple disorders can affect the bone near the attachment site, such as enthesophytes (apparition of bone spur) and avulsion fractures. Moreover, pathologies linked to the enthesis often require the reattachment of the tendon to the bone. Unfortunately, such procedure exhibits high rate of failure. One possible common issue among different clinically relevant disorders is the local stress concentration at the interface and within the bony region close to it. Therefore, a better understanding of the stress distribution at the tendon interface and inside the bone beneath the attachment is required to better understand enthesis related pathologies.

This thesis proposes a computational framework based on experimental data to achieve this goal. The main focus is to study the morphological and mechanical adaptation of the bone beneath the Achilles tendon and plantar fascia insertion and more particularly the bony tuberosity. The experimental dataset comprises low and high resolution micro-computed tomography (μ CT) images of the calcaneus bone of rats.

Firstly, the influence of a staining process on the samples before scanning is assessed. Our results show that staining is not necessary to clearly identify the Achilles tendon and plantar fascia attachment locations on the resulting images. Due to the additional noise (unwanted stained tissues) that it introduces, we choose to work with the unstained samples.

A computational image processing method is then developed to compute the attachment surfaces of both Achilles and the plantar fascia using these μ CT images. The values of the resulting surface areas are very consistent across all the analyzed samples, despite some variability in the samples whole morphology. Moreover, by visualizing the attachment of both soft tissues on the two sides of the tuberosity, it appears that such bony protrusion could favor the force transmission from tendon to bone and then to the plantar ligament.

The major part of this thesis is devoted to the development of multiple finite element (FE) models of the calcaneus bone to evaluate its bio-mechanical behavior under different loading conditions. Using a continuum FE approach, we explored the link between the pulling direction of the tendon and the corresponding stresses flowing into the bone. We also demonstrate a substantial impact of the plantar fascia on the stress distribution within the tuberosity, despite carrying much smaller forces than the Achilles tendon. Using micro-structural models, we highlight that a change of bone size along the cranio-caudal direction does not impact the mechanical environment in the tuberosity region. A progressive inclusion of different degrees of porosity leads to a redistribution of stresses and strain energies and induces local concentrations around the micro-pores. Nevertheless, the tuberosity still remains the highest stressed region, maybe acting as a protective structure to avoid high stresses within the entire bone. Finally, the inclusion of gradients in elastic properties is explored based on experimental measures of the local mineral content. Results show only a minor impact of the gradients on the local stress distributions, which are predominately influenced by the microporosity.

Acknowledgments

This Project has been a very enriching experience. From the sample extraction to the final report redaction, I have never stopped learning new skills and knowledge. I particularly enjoyed facing all the challenges encountered, especially the computing part to obtain the attachment surface areas as well as creating my own custom meshing procedure for the high resolution micro-computed tomography images.

I would like to hugely thanks Pr. Ruffoni for the master thesis subject as well as for the time consecrated with all the weekly online meetings despite the complicated pandemic situation. Huge thanks to Alexandra which was always present to guide me through the multiples parts of this project and to advise and help me for the report redaction.

I would like to thank the CHU of Liège for letting me extract my samples as well as the KU Leuven for the use of their infrastructures to scan them. Thanks also to Peter which allowed me to get the first insight of the Finite Element simulation for a three-dimensional low resolution bone model.

Multiple actors were also present in the shadows of this project: my friends, Marianne, Astrid, Timothée, Grégoire and Jeremy, thanks for their support and help even when I was working late in the night.

Contents

Abstract

Acknowledgments

Introduction	1
1 Theoretical background	2
1 Region of interest	2
2 Enthesis: from tendon to bone	4
3 Bone	6
4 Clinical relevance	13
5 Main aims of the thesis	17
2 Experimental part	18
1 Introduction	18
2 Sample preparation	18
3 Image acquisition	20
3 Morphology and image analysis	22
1 Introduction	22
2 Preliminary analysis of the μ CT images	22
3 Insertion site morphology	26
4 Discussion and conclusions	32
4 Global parameters analysis (continuum model)	33
1 Introduction	33
2 Methods	33
3 Results	38
4 Discussion and conclusions	45
5 Micro-architecture influence (micro-structural model)	46
1 Introduction	46
2 Methods	46
3 Results	51
4 Discussion and conclusions	56
6 Material properties investigation (micro-structural model)	57
1 Introduction	57
2 Mineral content assessment	57
3 Methods	58
4 Results	63
5 Discussion and conclusions	67
Conclusion and perspectives	68
Appendix	70
Bibliography	73

Introduction

Tendon-to-bone attachment, also known as the enthesis is a nice example of how the nature has managed to make the junction between two very dissimilar biological tissues: tendon and bone which are respectively soft and hard tissues. Tensile Young's Modulus can reach 2.3 [GPa] in tendons, whereas bone shows a value up to 20 [GPa]. Thus, a gap of at least two orders of magnitude is observed between the two tissues which constitutes one of the greatest interfacial material mismatches found in nature [59].

Studying such interface has multiple purposes. One commonly discussed in the literature is the clinical relevance. In case of failure, a fracture at the interface could be logically assumed as it can be considered as the weakest point between the two dissimilar materials. In fact, tendon fractures or bone fractures close to the interface are often observed.

For example, considering both immature and mature skeletons, avulsion fractures, which are the bone fractures close to the enthesis, are common disorders. In both cases, the cause of such fracture is the subchondral bone underlying the enthesis becoming weaker than the tendon-to-bone transition zone. For instance, in mature skeleton, this imbalance is created by the osteoporosis apparition [16] [52]. Another kind of pathology of interest is the formation of bone spurs. They are mainly due to a mechanical traction at the enthesis which induces an osteogenesis [5].

For this project, the bone side of such interface constitutes the region of interest. The aim is to understand how the stress distribution is characterized under different loading conditions.

This thesis contains six main chapters. The first one is focused on giving all the theoretical background in relation with our subject. Chapter two describes the experimental part of the project, from the sample preparation to the image acquisition process with and without contrast agent staining.

The third chapter is dedicated to the first main part of this thesis. It presents how the images are treated and used to different purposes. This chapter is divided into several parts. First, the impact of the contrast agent on the images quality is investigated. Then, two surfaces are computed for multiple samples using the raw data images : the Achilles tendon and the plantar tendon insertion sites. The complete methodology to achieve these tasks is detailed in this chapter.

The three next chapters are entirely dedicated to several biomechanical studies based on finite elements models of the bone region of interest. Chapter four focuses on a continuous model, two sensitivity analyses are presented. One on the angle of the force application at the Achilles side and a second one on the ratio of force application between Achilles side and Plantar Fascia side. Chapter five presents the influence of model size and micro-architecture on the calculated stress patterns. Finally, Chapter six investigates the influence of local material properties changes at the insertion obtained by introducing gradients in local tissue elastic properties.

The last chapter discusses the main findings and provides suggestions for possible future works. Three dimensional micro-structural models are notably discussed to have a more realistic approach.

Chapter 1

Theoretical background

This chapter introduces the theoretical background required for the reading of this report. The region of interest, the Achilles tendon attachment to bone and surroundings are firstly described from a general anatomical point of view. A comparison between the human and rat anatomy at the same location is also done. Then, the enthesis itself, where the tendon meets the bone, is discussed in terms of structure and functions. Because our study focuses on the bony side of the insertion, a section is dedicated to bone tissue. Its micro-structure, composition, remodelling process and mechanical properties are described. The clinical relevance of studying such interface, particularly the bone side of it, is finally be demonstrated. The main aims of the project are detailed in a last section.

1 Region of interest

For this work, a particular anatomical site is analyzed: the insertion of the Achilles tendon into the calcaneus. The goal of this section is to describe the anatomy of this region for the human case but also for the rat. Indeed, the rat is the animal model on which the entire project is based on.

The ankle makes the junction between the foot and the leg. Four bones are mainly constituting the ankle (Figure 1.1): the tibia and the fibula from the leg side, the talus and the calcaneus from the foot side. From this bony architecture, three main joints can be distinguished: the subtalar joint, the talocrural joint and the transverse joint [34] [27].

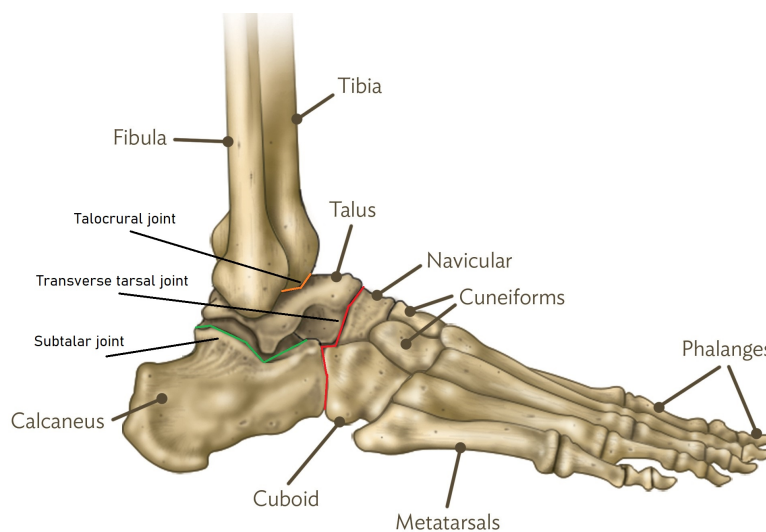


Figure 1.1: Lateral schematic view representing the biggest bones as well as the main joints of the ankle region (image adapted from [34] using [27]).

For this project, the calcaneus bone is particularly focused. It is the largest bone in the foot. On its posterior surface, the Achilles tendon comes to attach at a part of the bone called posterior calcaneal tuberosity. On the

opposite side, at the medial calcaneal tuberosity, the plantar fascia attaches. It is the fusion of multiple other ligaments, much smaller, coming from the metatarsal bones. These two are focused during the creation of finite element models later. Of course, there are still a lot of other ligaments attaching to the calcaneus but the purpose here is not to go into the details [35].



Figure 1.2: Schematic lateral view of human ankle showing Achilles tendon as well as the plantar fascia attachments into the calcaneus [63].

The Achilles tendon is the thickest and the strongest of the human body. Its role as a tendon is to attach muscle to the bone. In this case, the related muscles are the following: the soleus, the plantaris and the gastrocnemius muscles (Figure 1.3) [89]. Small sacs of fluid called bursae cushions are present at the interface between the tendon and the bone at the heel to bring support during the motion. The first one called subcutaneous bursa is located at the caudal side of the Achilles tendon. The second one, the retro-calcaneal bursa, is situated above the superior calcaneal tuberosity (Figure 1.4) [87].

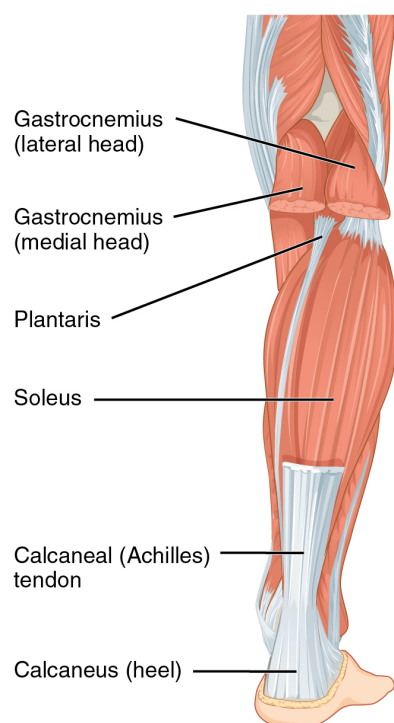


Figure 1.3: Schematic representation of the muscles present in the posterior leg (calf muscles and Achilles tendon) [89].

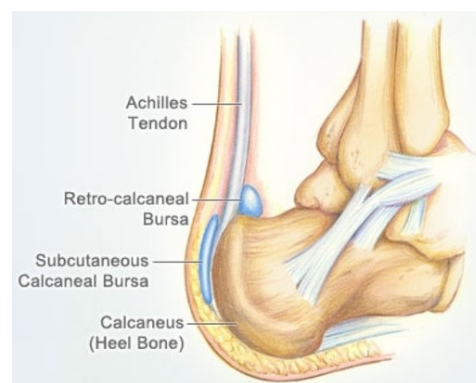


Figure 1.4: Lateral schematic representation of the ankle: localization of the bursa [87].

The plantar fascia is described as a strong layer of fibrous tissue located on the foot sole just beneath the skin.

It is divided into three main zones: a lateral portion overlying the muscles to the little toe, a medial section overlying the muscles to the big toe and finally the most important, the central section also called the plantar aponeurosis. Starting from its attachment zone at the calcaneus bone, this tissue is subdivided into five sections at the mid-metatarsal level. Each section corresponds to a specific toe. The central part is the most important from a structural and functional point of view. Indeed, it stabilizes the arch of the foot during heel rise to toe off steps of the walking cycle. This allows the first metatarsal flexion to carry a major part of the body weight. It also provides some shock absorption. [36]

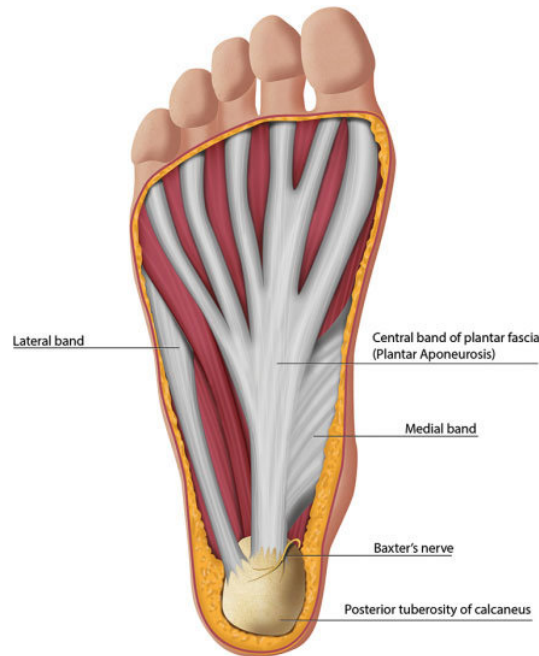


Figure 1.5: Schematic representation of the plantar fascia anatomy [47].

The rat shows very similar ankle anatomy which makes it a good start for a biomechanical study. Figures 1.6 and 1.7 are X-Ray images comparing a human foot and a rat foot. Several differences can still be spotted. The orientation of the calcaneus bone is more horizontally oriented than what is observed for a human. A consequence of that is that there is a difference in the angle of the Achilles tendon insertion. This is induced by the difference in terms of locomotion of the two species (biped for humans and quadruped for rats). In terms of movements, it is also similar for both cases. The Achilles tendon is solicited by stretching for both species. Dorsi- and plantar flexion are also dominating the gait cycle.



Figure 1.6: Ankle lateral X-ray for a human (Scale bars: 5 [cm]) [37].



Figure 1.7: Ankle lateral X-ray for a rat (Scale bars: 0.5 [cm]) [4].

2 Entesis: from tendon to bone

The goal of this section is to describe the entesis (which is the attachment zone between the tendon and the bone) in terms of its structure and functions.

The enthesis can be described as a dense fibrous connective tissue or fibrocartilage depending on the nature and the attachment location. An example of fibrous enthesis is the attachment between the humerus and the deltoid. This kind of attachment is described as a bundle of perforating mineralized fibres directly inserting in the bone or into the periosteum. Fibrocartilage enthesis is another kind, mostly discussed in the literature and the one of interest for this project. It is linked to common injuries at the Achilles tendon or rotator cuff [39].

Fibrocartilaginous entheses can be studied at different length scales [39] [6]. Firstly, from a macro scale point of view, the enthesis is divided into four main zones. Starting from the tendon site, there is the pure dense fibrous connective tissue which means that the presence of tendon is heavily populated by fibroblasts. It is composed mainly of linearly arranged type I collagen but also of type III collagen, elastin and proteoglycans. Moving from this zone, closer to the bone, there is an uncalcified fibrocartilage region which is an avascular zone populated by fibrochondrocytes, proteoglycan aggrecan as well as type I, II, III collagen. This zone functions as a force damper. It dissipates stresses generated in the collagen fibres of the tendon. Since the stress generation in the tendon depends on its angle insertion in the bone during the joint movement, the relative presence of uncalcified fibrocartilage in the enthesis is also linked to this insertion angle range to efficiently dissipate the stresses [6]. A relatively straight tidemark separates this zone from the next one, which signals a chemical transition between soft and hard tissue.

Indeed, the last zone before bone is called calcified fibrocartilage which is an avascular zone of calcified fibrocartilage. It is composed predominantly of type II collagen but also aggrecans and type I and X collagen. This zone constitutes the boundary with the highly irregular subchondral bone. It also provides the mechanical integrity of the enthesis. The gradient of mineralization is linked to a gradual transition in stress. This gradual transition in mineralization allows to avoid stress concentration in the enthesis. Bone, which is the last region, is fully described in a following section. These zones are illustrated in Figure 1.8 [39] [6].

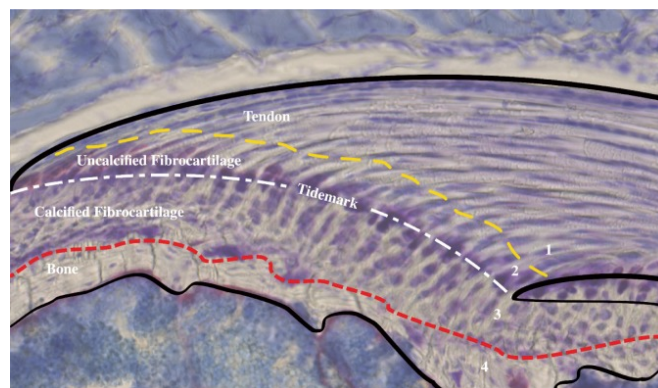


Figure 1.8: Illustration of the four zones defining the enthesis based on a histological section of a mouse. After staining, both fibrocartilage zones as well as the proteoglycans present in the tendons are depicted in purple [39].

Secondly, at the micro scale, two competing gradients can be observed [74]. The first one is arising from the alignment degree of the collagen fibres. Starting from the tendon, collagen fibres are very well aligned but they become progressively disorganized across the fibrocartilage zones and close to the bone. This progressive direction variability in the fibres induces a decrease in stiffness across the enthesis, it becomes more compliant.

On the other side, there is the presence of a mineral gradient, with a progressive accumulation of biapatite from the tendon to the bone. It induces an increase in stiffness across the enthesis. The balance between these two gradients is well optimized to finally, supposedly, reduce the stress concentration across the tissue. Moreover, it allows the existence of a compliant zone inside the enthesis [31].

Beside these gradients, a rough interface between the mineralized fibrocartilage and the bone is observed. This roughness contributes to stress concentration and a loss of strength but a gain in toughness is obtained in return. This could be more important for the insertion integrity [92].

The last scale of interest is the nanoscale. Collagen fibres are composed of complex structures of collagen molecules consisting of three amino chains organized as a helix. Each molecule has a length of 300 [nm] and a diameter of 1.5 [nm]. They are arranged in a staggered quaternary pattern to form the fibres. These fibres are linked to each other thanks to proteoglycans. Constitutive molecules are separated by a 35-45 [nm] gap. These gaps are increasingly filled by biapatite from the tendon (no biapatite) to the bone (50% in the volume fraction of

biopatite) which constitutes the mineral gradient. It is believed that nanoscale arrangement can have an impact on higher scale behavior [39] [6].

As a conclusion, through this multiple scale organization, the enthesis is an optimized, tough and compliant tissue.

3 Bone

Because our study focuses on the bone side of the entheses, this section concentrates on bone. The goal of this section is to introduce all the specificities of this tissue of interest. Its microstructure, composition, remodeling process and mechanical properties is discussed.

The human skeleton is composed of 213 bones which belong to four main different categories: long, short, flat or irregular bones. Each category has its specific biomechanical functions. For example, while long bones provide stability against bending and buckling, short bones provide stability against compression. Flat bone are responsible for the protection for vital organs and muscle attachment.

Besides these specific category functions, skeleton provides other general functions. It gives a structural support for the rest of the body, allowing locomotion and movement by providing levers for the muscles. It has a major role in the maintenance of acid-base balance and mineral homoeostasis. Finally, it serves as a reservoir for different growth factors and allows haematopoiesis to take place within the marrow spaces present in the bones [28].

3.1 Microstructure

Long bones are nice examples to understand all the structural components of a bone. They are composed of three main regions : diaphysis, metaphysis and epiphysis.

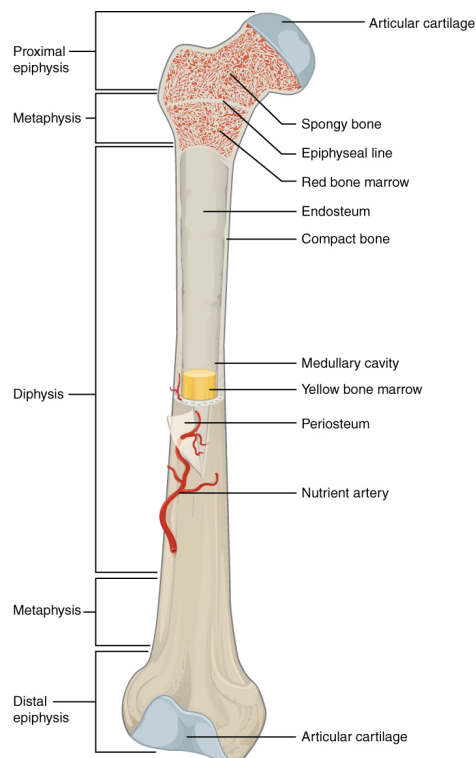


Figure 1.9: Schematic representation of long bone structure [90].

The diaphysis is the major part of a long bone. It is composed of cortical bone, a solid and dense material which surrounds the marrow space. In addition, it contains an outer periosteal surface and inner endosteal surface.

These two surfaces undergo both under remodelling but not in the same way. Bone formation exceeds bone resorption in the periosteal surface. The contrary is observed in the endosteal surface. This is explained by the greater biomechanical strain in the adjacent bone marrow compartment. As a consequence, with aging, the diaphysis tends to increase in diameter and the marrow compartment tends to expand.

In cortical bone, there are osteons, also called Haversian systems. They are described as a branching network within the cortical bone of cylindrical rods. Each osteon is formed of 10 to 15 concentric lamellae around a central Haversian canal with a diameter of 50 μm . The osteon diameter varies from 100 to 200 μm and its length from 1 to 3 μm . These sequential concentric lamellae present fibre orientations alternating on each concentric layer, forming a spiral around the central canal. Indeed, by using a circularly polarized light microscope, lamellae with alternate orientations are seen alternately dark, intermediate and bright. The intensity of the transmitted light depends on collagen alignment degree to the light beam axis as well as section orientation [76] [29] [18].

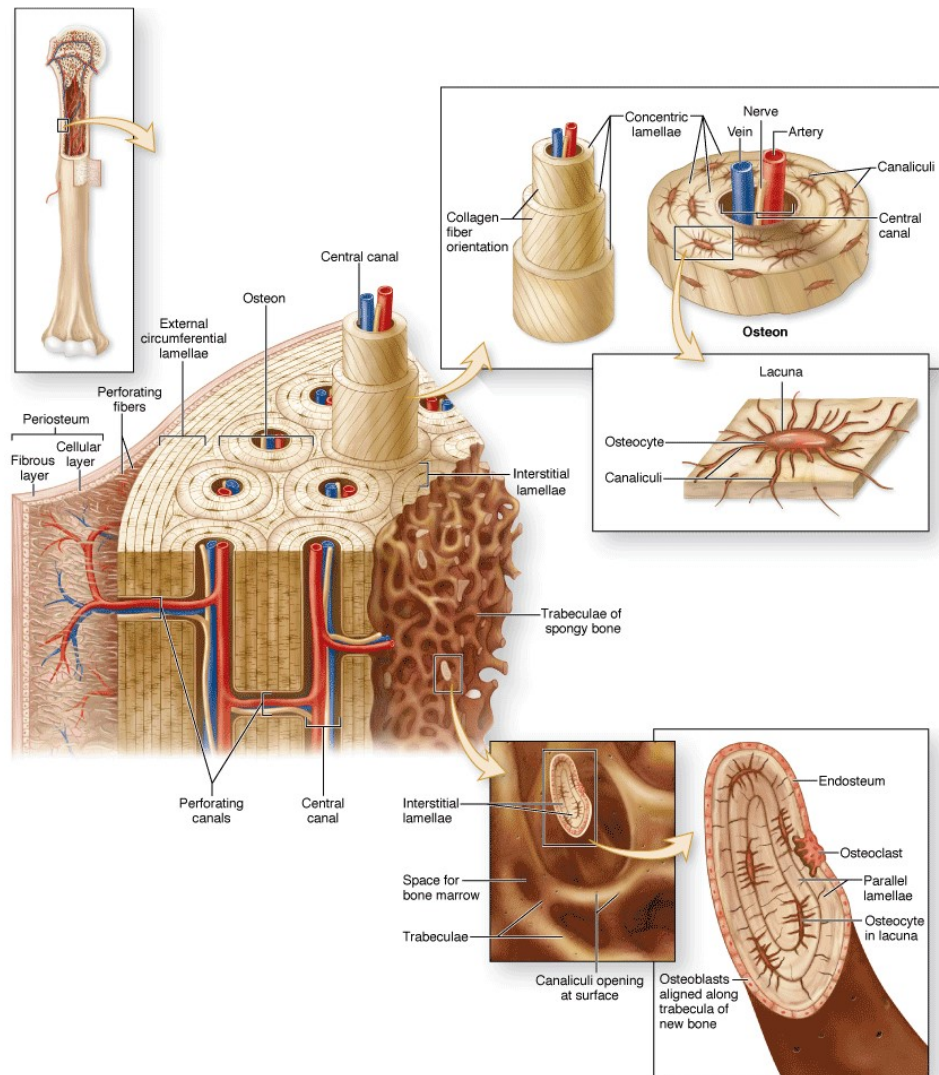


Figure 1.10: Detailed schematic structure of cortical and trabecular bone [61].

Cortical bone is metabolically active: the Haversian canal is used as protective empty space to embed the lymphatic vessel and the blood vessels which contributes to bring nutriment and other vital substances to the bone. The connection between the osteons to each other as well to the periosteum is ensured by transverse channels called Volkmann's canals. In addition to the osteonal bone described above, there is the lamellar bone surrounding the osteons. It is a well-organized bundle of large concentric rings of lamellae with a thickness of 5 to 10 μm around the outer 2-3 [mm] of the diaphysis. A second kind of lamellar bone is present in between these osteons. There are so-called interstitial lamellae where localized demineralized zones are present. They contain osteocytes, lacunae and canaliculi. They also form a network within the bone. This specific network could be the sensor of strain activity within the bone and so an initiator of the bone remodelling activity [76] [29] [18].

The growth plate makes the limit between the metaphysis (below it, next to the diaphysis) and the epiphysis (above it). These two last regions are composed of cancellous bone which doesn't contain osteon but a trabecular bone network surrounded by a thin shell of dense cortical bone instead. Trabecular bone looks like an open cell porous network with thin bone rods or plates included in a bone marrow compartment. For trabecular bone, they are

so-called bone packets. They are described as semilunar in shape, approximately 35 μm in thickness and also composed of concentric lamellae. Cortical and trabecular bone exhibit great differences in terms of porosity due to their respective architecture: 5% for cortical bone and up to 85% for trabecular bone. These values depend on the skeletal region and on the age. Indeed, porosity in both tissues increase with age [76] [29] [18].

In addition to these regions, a fibrous connective tissue surrounds the outer (cortical) surface of the bone, except at joints where articular cartilage is present called periosteum. This tissue contains nerve fibres, blood vessels, osteoclasts and osteoblasts. It is attached to the outer cortical surface thanks to thick collagenous fibres called Sharpeys fibres. In parallel, there also is a membranous structure tissue, called endosteum, which covers the inner surface of cortical and trabecular bone, the blood vessel canals and the Volkmann canals present in bone [76] [29] [18].

Figure 1.10 illustrates what has been exposed in this section. A general cut in a long bone is shown on the right part while the osteon and trabecular bone are shown in detail on the right part.

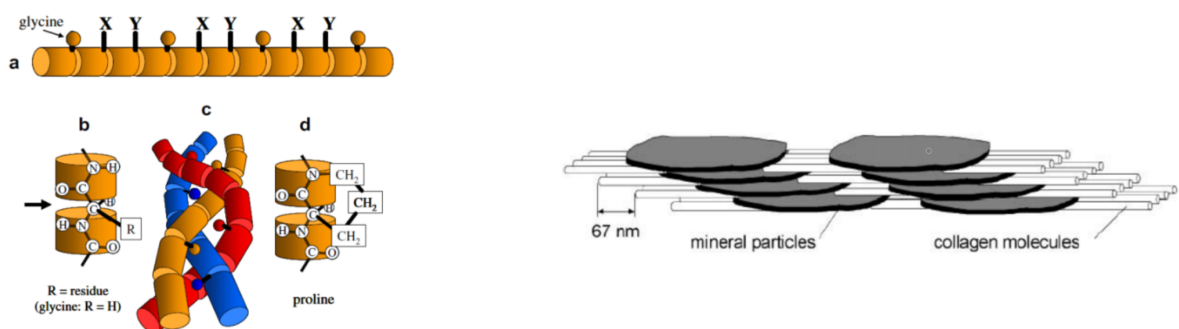
3.2 Composition

Bone is composed of three phases : an organic, an inorganic and a water phase. The weight (wet) and volume ratio are provided in Table 1.1.

Weight [wet]	Volume
Inorganic: 60%	Inorganic: 40%
Organic: 30%	Organic: 35%
Water: 10%	Water: 25%

Table 1.1: Bone phases [76].

The organic phase, also called matrix, is composed of collagen type I which represents 90% of the organic weight, collagen type III and IV but also non-collagenous proteins like osteocalcin, osteonectin and osteopontin, for example. These noncollagenous proteins are associated with the bone matrix mineralization and maturation. Collagen type I is the strongest and most abundant protein present in the body. It is composed of a highly repetitive amino acid sequence defined by Glycine-X-Y in which X means proline and Y means hydroxyproline. The collagen molecule forms a three polypeptide chain called alpha chain folded into a triple-helical structure. Type I collagen is composed of two alpha-1 and one alpha-2 chains. The dimensions of a collagen molecule are 300 [nm] in length and 1.5 [nm] in diameter [76] [10].



(a) Collagen type I structure schematic. On the top: simple polypeptide chain, on the bottom: triple-helical structure.

(b) Tiny platelets of hydroxyapatite in between collagen molecules schematic.

Figure 1.11: Illustration of two important components of the bone: the collagen type I and the hydroxyapatite [76].

The inorganic phase of the bone is composed of a form of naturally occurring calcium phosphate so-called hydroxyapatite ($\text{Ca}_{10}(\text{PO}_4)_6(\text{OH})_2$). These hydroxyapatite crystals may contain impurities like small amounts of carbonate, acid phosphate, potassium, magnesium or sodium, for example.

They are defined as tiny platelets which form within the collagen molecules by nucleating in the gap regions. This process is conducted by extracellular vesicles which are synthesized by chondrocytes and osteoblasts. They serve as micro medium allowing the phosphate and calcium concentrations to increase. When they are high enough to precipitate, they form crystals thanks to the presence of a nucleational core in the extracellular vesicles. These mineral particles are 3 [nm] thick, 15 [nm] wide and 50 [nm] long [76] [10].

In conclusion, the combination of minerals and collagen (with water) forms mineralized collagen fibrils which are the basic building block of the bone.

Hierarchical material

As a conclusion for the two first sections, it can be observed that bone is organized as a hierarchical material through different length scales. At the [cm] length scale, there is the organ level or bone shape composed of trabecular or cortical bone depending on the zone ([mm] length scale). In turn, these two kinds of bone are composed either of bone packets or osteons ([μ m] length scale) described by arrangement of lamellar bone (few [μ m] length scale) built from mineralized collagen fibrils ([nm] length scale).

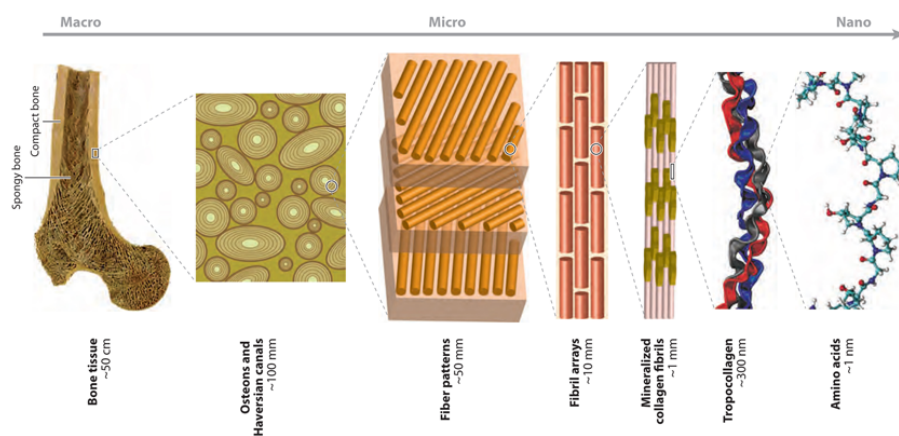


Figure 1.12: Hierarchical description of the bone material [8].

3.3 Remodeling

Bone remodeling allows bone to deal with several processes. First, it allows to renew damaged bone with new one in case of micro-damage or major fracture.

From a biochemical point of view, it regulates the calcium homoeostasis. Bone is a primordial storage site for calcium. Indeed, it contains almost the totality (99%) of the body calcium. The calcium release from bone is regulated by the parathyroid hormone while calcitonin acts as stimulus for calcium incorporation in bone [49].

It also allows adaptation to changes in the loading environment. For instance, in case of an increased loading repeatedly (during sport sessions for example), an increased bone mass and reinforcement of its architecture are observed (up to 40% increase in cortical thickness). The contrary is also observed: decreasing load conditions (e.g. long time immobilization, space flights) induces a decreased bone mass and a weakened bone architecture [76]. In addition to this mass adaptation, a finer adaptation mechanism exists. This mechanism is based on the mechanotransduction, it translates the signal coming from mechanical stresses inside the bone into appropriate adaptation in its architecture. This hypothesis is born more than one century ago with Roux and Wolff [91] [75]. Wolff assumed that mathematics laws governed the bone architecture. The number and the thickness of the trabeculae, in other term their distribution of mass, would be linked to the quantitative distribution of the mechanical stresses. Moreover, the trabeculae must be stressed axially in tension or compression. The theory was based regarding the correlation between stress trajectories and trabecular architecture in the proximal femur [91] [84]. Nowadays, bone remodeling is assumed to rely to a stochastic process which is under mechanical control.

There are three major actors in the remodelling process : osteoclasts, osteoblasts and osteocytes.

Osteoclasts are cells derived from monocyte-macrophage lineage which are the only ones capable of resorbing bone. Two cytokines are responsible for the osteoclast formation: RANKL (Receptor activator of nuclear factor

kappa-B ligand) and M-CSF (macrophage CSF). RANKL is more responsible of the formation itself. M-CSF is required for the proliferation, differentiation and survival of the osteoclast precursors but also for the survival of osteoclasts itself and the cytoskeletal rearrangement needed for the bone resorption.

Osteoclastogenesis happens in the bone marrow with the presence of stromal cells and osteoblasts thanks to the binding of RANKL and M-CSF to their respective receptor: RANK and c-Fms. The osteoclast differentiation is inhibited in presence of osteoprotegerin (OPG). OPG is produced by osteoblasts and binds to RANKL to prevent any interaction with RANKL cytokines [33] [82].

The bone resorption is possible thanks the hydrogen ions and cathepsin K enzyme secreted by the osteoclasts. They have both different but complementary duties: H^+ ions acidify the resorption zone of interest and so dissolve the mineral component of the bone matrix while cathepsin K has the role to digest the proteinaceous part of the matrix which is, like said before, mostly composed of collagen type I.

The resorption mechanism is composed of several steps. Osteoclasts bind to bone matrix thanks to integrin receptors which make the link between the osteoclasts membrane cell and the bone peptides. As a safety system to not resorb unwanted bone surface, the fibrillar actin cytoskeleton of the osteoclast organizes itself into an actin ring which allows to set a sealing zone around attachment surface. By binding to the bone matrix, the osteoclasts become polarized which in turn secrete H^+ ions thanks to H^+ -ATPase which causes the exocytosis of capsules containing the cathepsin K enzyme and thus induce the bone resorption. The process is ended when the actin rings block the resorption [33] [82].

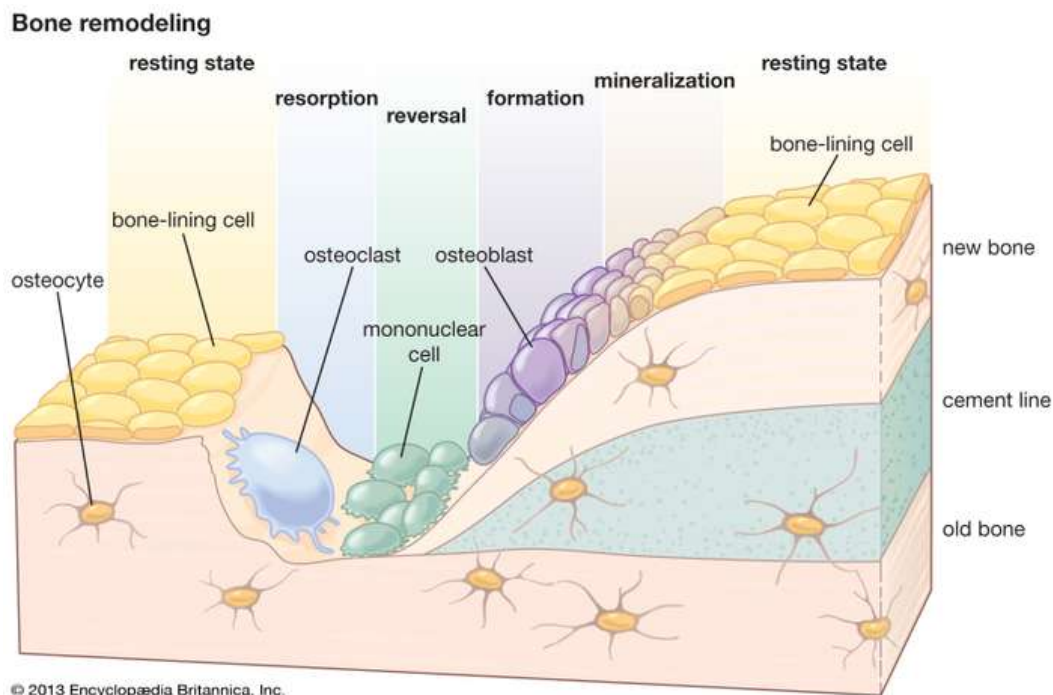


Figure 1.13: Bone remodelling schematic : illustration of the different possible states including resting, resorption, reversal, formation and mineralization states [12].

In contrast with osteoclasts, osteoblasts synthesize new bone matrix by secreting type I collagen as well as other matrix proteins at the bone surface. Osteoblasts arise from the differentiation of mesenchymal stem cells (MSC). In case of trabecular bone, they are secreted in rings called lamellae that expand outward as the trabeculae get larger. The calcium phosphate, a hard ceramic material, begins to surround the cells as the new tissue grows around the osteoblast. Each osteoblast stops making new bone tissue and is transformed into an osteocyte if it becomes surrounded completely by the new hard bone tissue [17].

Alternatively, when a group of osteoblasts has finished filling in a cavity, the cells change in shape and become flat, lining at the surface of the bone. They are now called lining cells. These lining cells have several goals including the flow regulation of calcium from and into the bone but also responding to particular hormones in order to make special proteins that activate the osteoclasts activity previously described [13].

Finally, the osteocytes, like just said, are terminally differentiated osteoblasts. They are essential in the bone

structure and metabolism. They lie within a syncytial network. This network is located in the lacunae and the canaliculi connecting them together. Osteocytes have also extensions called gap junctions going through these canaliculi. Thanks to these extensions, osteocytes are able to "communicate" with each other.

Several matrix proteins are expressed by the osteocytes. These proteins have two main roles: the regulation of the mineral exchanges within the bone fluid circulating in the canalicular and lacuna network as well as to support intercellular adhesion [11]. Osteocyte, osteoblasts and lining cell syncytium work in combination as a mechanosensation system. A stress signal coming from the bending or stretching of bone is transduced by the osteocyte into a variation in fluid flow transported through the gap junctions. These variations of fluid flow act as a stimulus for bone resorption or deposition.

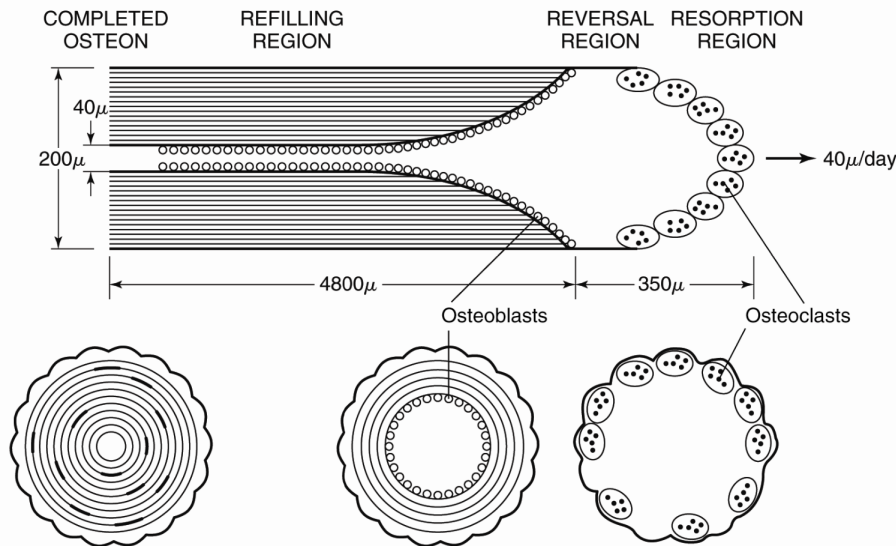


Figure 1.14: Bone remodelling schematic for an osteon : longitudinal view [76].

Figure 1.13 shows the different possible states in the bone remodelling process. This process ensures through the alternation of these states, a homeostatic equilibrium in order to fulfil all the previously described functions. Figure 1.14 depicts a schematic representation of the bone remodelling process for the creation of an osteon. Several states can be distinguished through the main direction of the osteon. From the right to the left, a first region is occupied by osteoclasts which are resorbing the bone. A reversal region separates the first one from the refilling region where osteoblasts are acting to fulfil the hole of bone while keeping a space at its centre. This hole is defined as a Haversian canal. Finally, on the left side, a completed osteon is shown.

3.4 Mechanical properties

Bone is a relatively ductile material. Figure 1.15 presents the typical stress-strain curve which is obtained with a sample of compact bone loaded in tension. From this curve, two regions can be identified: a linear elastic phase separated from a plastic region by a yield point with a brittle fracture of the material at the end. From the linear elastic region, the Young's modulus of the bone, representing its stiffness, can be deduced from the slope of the line. From the yield point, a yield stress corresponding to a certain yield strain can be deduced. These values correspond to the stress-strain combination delineating elastic from plastic behavior. Finally, at the failure point, the ultimate stress and strain can be identified.

Regarding cortical bone, the tissue shows anisotropic behaviour. Indeed, the longitudinal and transverse mechanical response to different loading conditions are different (Figure 1.16).

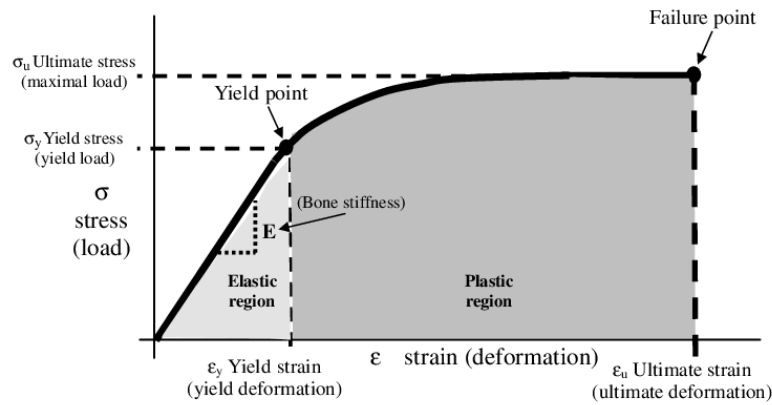


Figure 1.15: The stress-strain curve obtained by loading a sample of compact bone in tension [79].

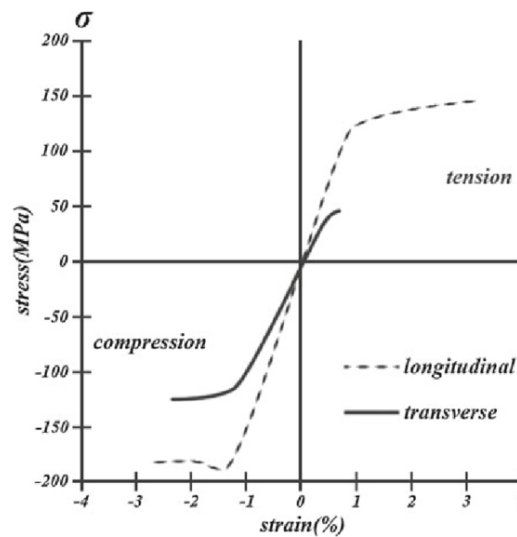


Figure 1.16: Stress-strain behaviour of adult human cortical bone samples [53].

Several observations can be done. For both transverse and longitudinal directions, Young moduli in compression and tension are very similar. The values are 18 [GPa] for the longitudinal modulus and 10 [GPa] for the transverse modulus. The strength is clearly asymmetric: cortical bone shows higher ultimate stress in compression than in tension. More specifically, ultimate stress is higher for both loading conditions in the longitudinal direction than in the transverse direction. Indeed, ultimate stress reaches 190 [MPa] in longitudinal compression and 150 [MPa] in longitudinal tension. In contrast, ultimate stress reaches 130 [MPa] in transverse compression and only 50 [MPa] in transverse tension [76].

These values can be understood by observing the crack propagation along the two main directions in a cortical bone sample. If the sample is loaded in tension along the longitudinal direction, crack propagates along the transverse direction. In contrary, if the sample is loaded in tension along the transverse direction, crack propagates along the longitudinal direction. Taking the architecture of cortical bone into consideration, a crack has more difficulty to propagate in the transverse direction than in the longitudinal direction due to the multiple concentric layers of lamellar bone along the longitudinal direction. It acts as multiple layers of protection, deflecting the crack.

More specifically, when a crack, in the transverse direction, starts to grow under an increasing load (Figure 1.17), multiple micro-cracks are created ahead of it. These micro-cracks align parallel to the cement sheaths that surround the osteons, and consequently in a perpendicular way to the crack initial path. In contrary, when there is a crack in the longitudinal direction, it can more easily propagate in between the osteon layers and the material can show catastrophic failure [46] [76].

As a conclusion, the bone architecture is optimized to dissipate the crack energy, considering that the long bone is longitudinally loaded. This explains the highest values for ultimate stress mentioned before.

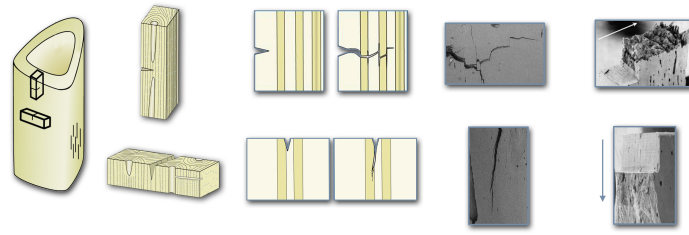


Figure 1.17: Illustration of the crack propagation in a cortical bone sample loaded along the longitudinal axis. Longitudinal (on the top) and transverse (on the bottom) cases depicted [46].

4 Clinical relevance

The goal of this section is to demonstrate the clinical relevance of studying such interface between soft and hard tissues. Moreover, this project being concentrated on the bone side of the interface, the clinical relevance on this side is highlighted as well. The pathologies linked to the enthesis are multiple. A lot of injuries require the reattachment of the tendon to the bone. This kind of procedure exhibits poor results, with a high rate of failure after surgery. This rate of failure could be linked to the local stresses developed at the interface which are not well dissipated in reattached enthesis. The knowledge about entheses remains still limited and a lot of questions remain about the mechanisms underlying the pathologies. Several aspects are discussed in this section. The pathologies affecting the interface itself are firstly described. After that, diseases affecting in particular the bone side are more extensively discussed, with notably the enthesophytes and avulsion fractures.

4.1 Achilles Tendon Enthesopathy

Achilles tendon enthesopathy refers to disorders affecting the Achilles tendon enthesis. It is a common disorder find in adults especially older people and females, with up to 16% of the general population affected [25].

The main causes of enthesopathy are either an overuse situation by chronic traction like for example in case of athletes, a contracted or shortened calf muscles (group of muscles composed of the gastrocnemius and the soleus muscle located on the back of the lower leg) in a situation of obesity or sedentary lifestyle, autoimmune diseases (such as inflammatory conditions or rheumatoid arthritis) but also genetic factors [59].

Enthesopathies could also be a secondary effect to a change of stiffness of the muscle-tendon unit after exercise, fatigue or injury. For an athlete, a practical situation in which a micro-damage can be induced is for example during a run on a hard surface like concrete. Hard surfaces induce much greater reaction force than running on soft surfaces. This reaction force is superior to the force induced by the muscle and repetitively landing on such surface send shock waves which are partly absorbed by the Achilles tendon but also at its interface to the bone. This can create micro-damage, especially if the movement is not correctly controlled. For example, an insufficient strength generated by the calf muscles results in a poor control of feet during landing phase of the running cycle. Such situation induces a change in the alignment between the insertion angle of the Achilles tendon and the calcaneus which could lead in turn to a vulnerability to injury [51].

The main symptom of enthesopathy is pain felt during walking at the posterior heel. There are also joint stiffness and therefore difficulties of moving the affected joint, swelling and warmth feeling near the affected joint. During diagnose, a palpation of the patient's Achilles tendon close to its insertion as well as a manual dorsiflexion of the ankle causes pain. Additional tools like imagery (MRI, X-ray) in combination with contrast agent injection can be used, especially when another condition might be the cause. These images are then analysed to visualize any swelling or damage at the enthesis [59].

Several treatments exist to enhance the patient's condition. Medications are a first resource such as arthritis medication or also NSAIDs (non-steroidal anti-inflammatory drugs). Physical therapy is also another way to reduce the pain and the stiffness of the affected joints, the goal is to bring back the flexibility next to the enthesis. For instance, for Achilles tendon enthesopathy, stretching the calf muscles multiple time per day relieve the pain

on a long time perspective. Finally, orthotic devices, for example a heel cup which insert in the shoe or a splint, can help to reduce pain and also prevent further injury [59].

Enthesopathies include the enthesitis, which is related to the inflammation of the enthesis. It is associated with joint diseases such as rheumatoid arthritis (RA) or spondyloarthritis (SpA). SpA usually affects the spine but also sacroiliac and hip joints while RA affects mainly the peripheral joints [24].

Complications of such pathology are the bursitis (inflammation of the bursa), ossification or calcification (see next section) or also fibrosis affecting the enthesis as well as the Achilles tendon [88].

Figure 1.18 shows the case of an 18-year-old man. He has been diagnosed with juvenile spondyloarthritis. The part A of Figure 1.18 show MRI image without contrast agent while the part B shows the MRI image after contrast injection. Several observations can be done: the irregular form of the Achilles tendon with an increased signal intensity, retrocalcaneal bursitis (main arrow), a localized calcaneal bone marrow oedema (top arrowheads) and also a calcaneal erosion (bottom arrowheads) [7] coming from [23].

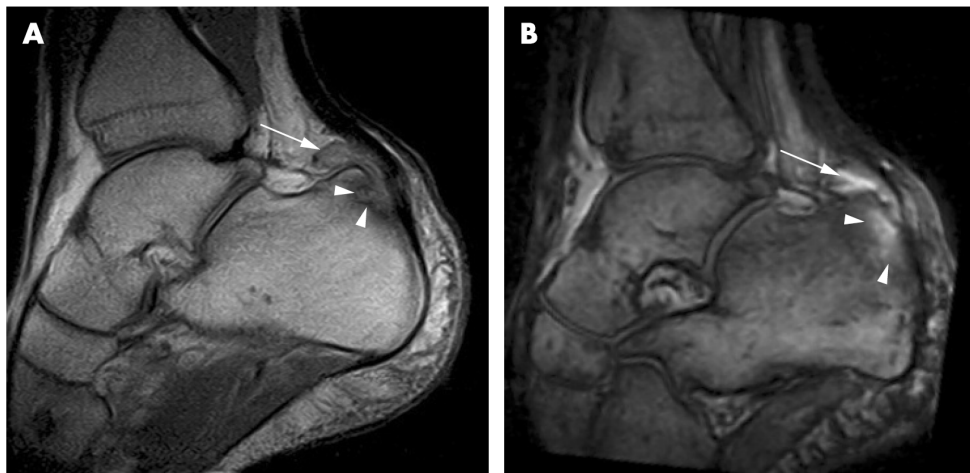


Figure 1.18: Achilles tendon enthesitis of an 18-year-old man diagnosed with juvenile spondyloarthritis. (A) MRI image without contrast agent (B) MRI image with contrast agent [7] coming from [23].

4.2 Enthesophytes

Entesophytes are abnormal bony projections (or bony spurs) that grow at the entheses where the tendon attaches to the bone. They are different from osteophytes which are also bony projections but in this case in the joint spaces. At the ankle region, the bone spurs can appear in both attachment of the Achille tendon and the plantar fascia.

This pathology is linked with a high level of physical activity and often combined with a specific condition of the patient like seronegative spondyloarthropathy and calcium idiopathic skeletal hyperostosis (DISH). In other words, entesophyte is characterized by a bony response (traction spurs) to a significant enthesis localized high tensile stress. Seronegative spondyloarthropathy is a family of rheumatologic auto-immune disorders linked to a genetic factor (HLA-B27). DISH is characterized by a hardening of the ligaments in areas where they attach to the spine [51] [5].



Figure 1.19: X ray image of a calcaneal spur [44].

This disorder is more common with an increasing age, as demonstrated in the study [64]. From the 1335 patients participating to this study, 32.2% present plantar fascia spurs and 13.1% present Achilles spurs. Another study [44], mentioned that 25 % of the population is estimated to form a bone spur either at the Achilles or plantar fascia attachment but a proportion of this affected population could be asymptotic. From a genetics basis, some patients are called "bone former" which means that such individuals form bone at mechanical stress level lower than the one triggering comparable osteogenesis in other individuals. Therefore, this kind of patients is more prone to form bone spurs. Enthesophyte can also be triggered to induce a bone adaptation to an injury. For example, if injury leads to an abnormal movement at the ankle level, the bone spur helps to restore a functional joint surface [5].

Enthesophytes can be treated in a non-surgical or surgical way.

Orthotic devices can again be used as a non-surgical way to relieve pain and enhance the condition of the patient. Heel lifts are used to reduce the stress on the Achilles tendon and therefore the pain. In a same way, shoes with cushioned soles can help in decreasing the friction and therefore reduce significantly the irritation of inflamed tissues from the heel spurs [60].

In case of surgical approach, the Achilles SpeedBridge technique can be used, for example. The aim is to partially detach the tendon and remove any diseased parts of the tendon and also calcific deposits around the affected zone. The retrocalcaneal bursa in front of the bone is also removed during the procedure. Once this first part is done, the bony bump on the back of the heel bone is then removed by using a saw. Finally, the tendon is reattached back to the bone thanks to very small bone screws and synthetic material pieces. The tendon and the skin incision are finally stitched up with absorbable sutures. After surgery, the foot is placed in a below-knee plaster backslab for a certain period. This surgical technique has a 90% of success rate, 10% failure rate and 1% of the cases are aggravated by the surgery [81]. The surgical approach is infrequently used and it is reserved for patients which have not respond to the non-surgical treatment or which suffer from chronically inflamed spurs [80]. The study [44] shows that over 26 patients operated all with a same similar technique, 69% of the surgery outcomes have been successful, 25% have been moderate (residual minor symptoms) and 6% have been a failure with a second surgery required to remove a bone spur regrowth appeared 1 to 4 years later.

A quite close condition to enthesophytes is observed in Haglund deformities (Figure 1.20). It is often a disorder which appears in association to a bone spur formation as observed in [44]. This term is used for the apparition of abnormalities at the bone and the soft tissues located at the Achilles tendon attachment level, on the back on the foot. This abnormality is a round enlargement of the ankle bone at the enthesis level. An irritation of the soft tissues by the friction with the bony spur is induced when it rubs against the interior of the shoe (rigid) [72].



Figure 1.20: Haglund Deformity example : bony prominence over the back of the heel on a 15-year-old girl [86].

4.3 Avulsion fractures

When a piece of bone is pulled away from a tendinous or ligamentous attachment, it is called an avulsion fracture. Notice that this disorder can occur at numerous sites but some areas are more likely to be affected, such as the ankle notably. At this location, it happens mostly at the base of the fifth metatarsal, at the talus or at the calcaneus, our zone of interest. Because this kind fracture often crosses into the surface of a joint, it is also referred to as an intra-articular fracture [69].

In terms of incidence, tarsal fractures (it includes fracture at the bones of the ankle and heel) account for 2% of all fractures, the calcaneal fractures represent 50 to 60% of all fractured tarsal bones, and the avulsion fractures at the calcaneal tuberosity are counted for 1.3-2.7% of all calcaneal fractures [16] [30] [20].

The pathophysiology factors linked to the avulsion fracture are multiple. The major one is a poor bone quality induced by osteoporosis. Indeed, the peak incidence of such fracture concerns females in their seventh decade for who diminished bone mineral density is observed. The combination of osteoporosis with a violent contraction of the triceps surae with a forced dorsiflexion or strong concentric contraction of the triceps surae with a knee in full extension leads to such a fracture [16]. The avulsion fracture can also be caused by an accident evolving high stresses situation. The most common ones are: an intense ankle dorsiflexion caused by a fall from height inducing a direct loading of the calcaneal tuberosity (also called Lovers Fracture derived from the old fact of a lover jumping from the balcony trying to escape from the lady's spouse [73]), an extensive plantar flexion of the ankle joint creating a collision between the posterior malleolus and the tuberosity or a direct compression of the calcaneal tuberosity in case of an vehicle accident for example [30].

Symptoms linked are pain associated with swelling and inability to bear weight. A large deformity can be observed at the ankle [16].

The treatment of such fracture can be conservative or operative. A long-term functional disability can be induced if the avulsion fracture is inappropriately managed. The conservative way is possible if the piece broken piece of bone is slightly displaced. An immobilization is required, by a cast or a brace to hold the foot bones in proper position pending the fracture resorption [66].

The operative way is required when a significant displacement of the fractured piece of bone is observed. It involves the surgical intervention with the reestablishment of the calcaneal original dimensions and alignment. The goal is to improve post-operative gait mechanics but also decrease post-traumatic subtalar arthritis. Depending of the fractured zone, the surgical procedure differs. If the fracture does not involve the subtalar joint, only two screws are placed. The first screw is placed perpendicularly to the fracture to fix the piece of bone with the contralateral cortex and the second one perpendicularly oriented with respect to the Achilles tendon in order to resist the traction forces coming from it. If the fracture does involve the subtalar joint, a calcaneal plate in addition to the two screws is used to increase the stability [30].

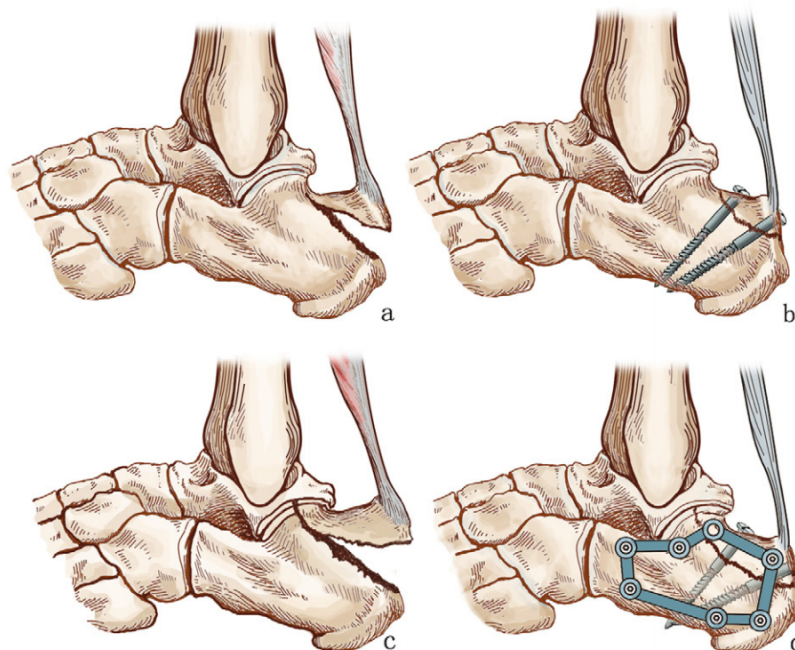


Figure 1.21: The schematic representation of the avulsion fractures and the surgical procedures linked. (A) The fracture does not involve the subtalar joint (B) surgical procedure involved for this first kind of fracture (C) the fracture does involve the subtalar joint (D) surgical procedure involved for this second kind of fracture [30].

These two last examples of pathologies show nicely the clinical relevance of studying the bone side of such interface. Indeed, analysing how the stresses are locally distributed inside the bone under a stress configuration

close to what is really happening allows to better understand how mechanical constraints can induce either a bone spur formation or a catastrophic injury such as the avulsion fracture.

5 Main aims of the thesis

From the literature, it can be observed that there is quite a lot of studies focused on the enthesis itself. Its structure and functions are deeply discussed. But few of them focus to the bone side of the interface. Our main goal is to assess local stresses within bone at the insertion with image-based micro-finite element analysis.

Because we want to visualize the insertion of the Achilles tendon, a preliminary part focuses on whether the use of a contrast agent on the sample before imaging induces a better visibility on what is happening at the interface. And therefore, if it is improving the quality of the image for later use.

After that, surface area of both Achilles tendon and plantar fascia attachment is computed quantitatively in order to have an accurate assessment to use as an input for Finite Element simulations. Multiple bone samples are used and compared.

Finally, the main part of the thesis is a biomechanical study of the local bone stresses beneath the enthesis thanks to Finite Element models. To begin, two sensitivity analyses are done on a continuum model. One considering different angles of force applications on the Achilles side and a second one considering different ratios between loads applied at the Fascia side and Achilles side.

Then, micro-structural models are investigated. The question of the impact of the length of bone on the local stresses within the tuberosity is answered. The tuberosity is defined as the protuberance at the calcaneus bone where the Achilles tendon and plantar fascia attach. After that, three versions on the same sample model are compared : no porosity (continuum version), trabecular porosity only and micro-porosity (complete micro-architecture) models. Finally, the insertion of a gradient along the Achilles tendon side is investigated. Two kinds of gradients are tested : linear and hyperbolic, the latter being based on real measurements of the mineral content.

Chapter 2

Experimental part

1 Introduction

This second chapter describes the very first step of this project. Starting from sample extraction and preparation, the goal is to acquire images, thanks to micro-computed tomography. This scanning method has been selected because of its nondestructive and noninvasive approach. This method produces accurate results in comparison with, for example, conventional histology on both animals [68], [62], [40], [42], [1] and humans [41], [70], [26], [50], [19]. Additionally, it has a great efficiency in terms of amount of time required to scan large amount of volume. The scanning process has been focused on imaging the bone side with high resolution because, as described in Chapter 1, it is our main region of interest. These images will serve to compute different attachment surfaces as well as to build models for finite element analysis. The addition of a contrast agent to the sample is also investigated in order to evaluate its impact to the image quality in terms of distinction between the tendon and the bone. This chapter presents the sample extraction and preparation as well as the image acquisition procedure. Also note that this section only presents the procedure followed for the new samples assessed during this project. The experimental process regarding already acquired data can be found in [83].

2 Sample preparation

The sample preparation is a very important step before scanning. Indeed, the samples need to be well extracted in order to have only the tissues of interest remaining. In this case, contrast agent will also be used. Proper preparation methodology is therefore required to obtain exploitable results.

Extraction

The extraction process has been conducted on a 3 months-old Sprague-Dawley rat (born 19/08/2019), weighting 448g. The animal was available at the university hospital of Liege (CHU) and aimed to be used in another study for which ethical approval had already been received. The posterior left and right leg were extracted at the same time at the CHU of Liège. The Figure 2.1 (A) shows the rat leg sample before any extraction step.

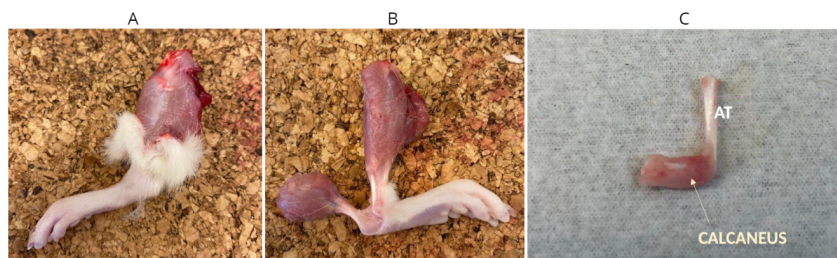


Figure 2.1: (A) The rat leg sample before any extraction step (B) Result of the incision to separate the gastrocnemius and fibularis groups (C) Final result of the extraction process: AT = Achilles tendon and the calcaneus are shown.

The process for one leg follows several steps (which are repeated for the second leg as well). First, the leg is cut from the rat. Then, the skin is removed from the cut leg in order to visualize the muscles. An incision is made to separate the gastrocnemius and fibularis groups (Figure 2.1 (B)). The goal is then to spot the calcaneus and the Achilles tendon and remove very carefully more skin around the calcaneus. In a same way, the next step is to remove cautiously the paratenon layer (sheath surrounding the tendon). The tibia is cut above the articulation in a first time. The region around the articulation is then cleaned and the tibia is cut again now closer to the calcaneus. The gastrocnemius is finally removed. It was voluntarily kept until now to facilitate the manipulation of the tissues. The final step is to clean the calcaneus in order to spot the beginning of the metatarsals and make a final cut to get the result shown in Figure 2.1 (C).

Preparation methodology

After the extraction process, the samples were stocked in tubes (Figure 2.2) and treated before imaging following a defined preparation methodology.

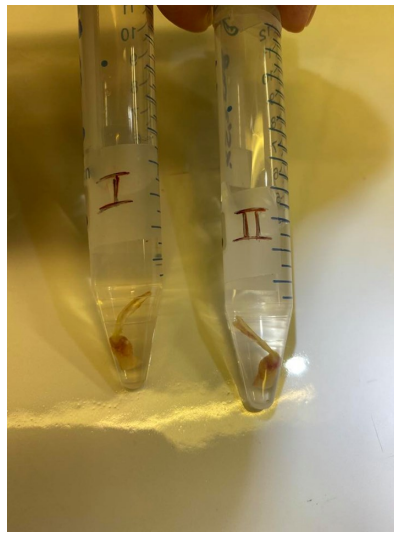


Figure 2.2: Samples within the tubes used for chemical treatment and conservation.

The preparation methodology schedule is described in the table 2.1.

For both samples (in total two), the first step was to fix the tissues with a first fixation solution 1 (glutaraldéhyde 2.5%, 0.1 M Na acetate buffer, pH = 7.2). The aim of this solution is to avoid the degradation of the biological tissue by canceling all the ongoing left biochemical reactions. After that, the samples were conserved in a second solution before a first μ CT scan. This second solution is an acetate buffer (0.2 M, pH 8.0 with acetate buffer, pH 8.0 with an additional 20mM of NaN₃) used for rinsing and conservation. Finally, the samples were treated with a third solution before a second μ CT scan. This final solution is the contrast agent: wPTA 1 %, pH 1.4-2.0.

Day 1	Extraction of the tendon-to-bone interface for two samples Immersion in solution 1 for four hours for both samples
From day 2 to day 9	Immersion in solution 2 for both
Day 9	Scan of sample 1 (without contrast agent)
From day 9 to day 16	For sample 1: immersion in solution 3
Day 16	Scan of sample 1 (with contrast agent) Scan of sample 2 (without contrast agent)
From day 17 to day 23	For sample 2: immersion in solution 3
Day 23	Scan of sample 2 (with contrast agent)

Table 2.1: Methodology schedule followed during this experimental procedure.

3 Image acquisition

In this section, the scanning process is detailed. The scanner and its specific working parameters for the acquisition and reconstruction of the images are presented.

Scanner

For this study, a scanner SkyScan-1272 from Bruker company was used at the K.U. Leuven University. This scanner is depicted in Figure 2.3. This scanner can be used for multiple applications from 2D/3D image analysis for surface and volume rendering.



Figure 2.3: SkyScan-1272 from Bruker company [14].

A CT scanner uses motorized X-ray sources which are able to rotate around a circular opening called a gantry. Special X-ray detectors are placed directly in opposite to the X-ray source while it is rotating. Practically, X-rays are sent to the sample, some are absorbed, some other pass through the sample and are received by the X-ray detector. The information is in turn transmitted to a computer. This computer uses a particular algorithm in order to reconstruct the images slice by slice. The device is able not to only rotate but also move in order to capture slice by slice the sample images.

Acquisition parameters

An additional preparation step is required before scanning. Letting wet biological tissues in contact with the air during a scan is not recommended. Indeed, it leads to a shrinking phenomenon. The moist surface of the sample will dry due to the high temperature present inside the scanner. This dynamic shrinking induces movement artifacts during scanning session and therefore results in poor quality images. To address this issue, the solution is to put the samples in a closed plastic tube before placing them in the scanner, what we did for our two samples.

The table 2.2 contains the values of the acquisition parameters. Distance between the camera and the source and between the object and the source are kept the same through the scans as well as the source voltage and the source current notably. Another important parameter is the resolution of the scan or, in other words, the image pixel size. For these scans, we choose to work at a low resolution of $5\text{ }\mu\text{m}$. Four scans are performed in total, two for both samples: one without contrast agent and one with contrast agent.

Regarding the reconstruction parameters, the important values are shown in Table 2.3 for sample 1 (T1) and Table 2.4 for sample 2 (T2). There is a size difference for the resulting images between the two samples: sample 2 got larger images than sample 1. A consequence of that is an increasing time in the reconstruction duration per slice and so in the total reconstruction time as well. More slices are created for the case without contrast agent than with contrast agent for both samples which also influenced the total reconstruction time.

Acquisition	
Parameter	Value
Camera to source [mm]	171.87562
Object to source [mm]	95.48650
Source Voltage [kV]	55
Source Current [μ A]	181
Image pixel size [μ m]	5.000002
Depth [bits]	16
Exposure [ms]	2200

Table 2.2: Key parameters of the μ CT scan acquisition (same for all the scans).

Reconstruction		
Parameter	Value	
	T1 no CA	T1 CA
Reconstruction duration per slice [s]	0.798806	0.650657
Total reconstruction time [s]	2140	1734
Sections Count [slices]	2679	2665
Result Image Width [pixel]	2604	
Result Image Height [pixel]	2536	

Table 2.3: Key parameters of the μ CT scan reconstruction (for sample 1: (T1): with and without contrast agent (CA) cases).

Reconstruction		
Parameter	Value	
	T2 no CA	T2 CA
Reconstruction duration per slice [s]	1.013050	0.993766
Total reconstruction time [s]	2717	2391
Sections Count [slices]	2682	2406
Result Image Width [pixel]	2848	
Result Image Height [pixel]	2628	

Table 2.4: Key parameters of the μ CT scan reconstruction (for sample 2: (T2): with and without contrast agent (CA) cases).

Chapter 3

Morphology and image analysis

1 Introduction

The first part of the project consists in the analysis of morphological aspects of the attachment region, based on the micro-computed tomography (μ CT) images obtained with the experimental part presented in Chapter 2.

The first question we address is to qualitatively investigate the impact of the contrast agent staining on μ CT images. The aim is to know whether the staining provides a significant improvement in the enthesis and the attachment region visualization. To achieve this goal, the software CTVox (Skyscan, Bruker) is used. It proposes several tools to enable the manipulation of the 3D volume reconstructed from the μ CT images.

Our second aim is to visualize and quantify the attachment area of the two main soft tissues inserting into calcaneus: the Achilles tendon and the plantar fascia. In addition to being a valuable input for our further finite element model, this procedure allows us to understand the adaptation of the bone global morphology to the insertion sites. A combination of three softwares: ImageJ, CTAn (Skyscan, Bruker) and Matlab is used. ImageJ and CTAn are strong tools for image treatment, the second is specifically dedicated to μ CT images treatment. Matlab is exploited for the quantification part of the analysis, consisting in the last steps of the image processing as well as the actual measurement of the surfaces of attachment.

2 Preliminary analysis of the μ CT images

The aim of this section is to present the different steps constituting the preliminary analysis of the μ CT images.

2.1 Post acquisition processing

In order to ensure a fair comparison among samples, a first processing step of realignment is applied. To achieve this step, ImageJ is used and in particular a specific plugin called BoneJ [38]. It proposes an option to realign an entire stack of slices (the μ CT images). The principal axes and corresponding moments of inertia are computed, and the whole stack is rotated so that the three-dimensional axes of the image are parallel to the principal ones [9].

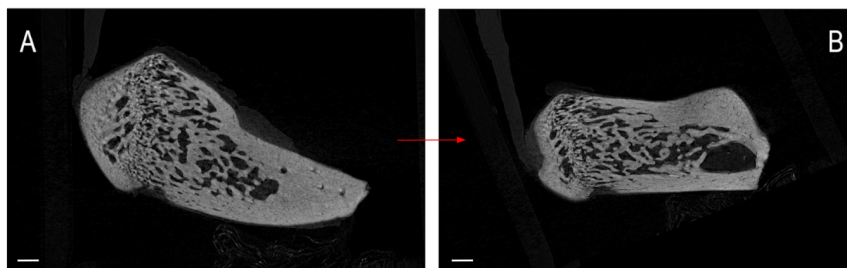


Figure 3.1: Comparison between non-realigned version (A) and aligned version (B) of an example slice. (T1 sample, sagittal plane) Scale bar: 500 μ m.

Eventually, some cropping is also realized in order to already remove useless parts of the images for this project. They parts include void pixels at the each side of the image. As an example, Figure 3.1 shows on the left (A) the non-realigned version of a slice from T1 sample while the right part (B) shows the realigned version.

2.2 Whole bone morphology and deduction of the insertion site

Figure 3.2 (sample T1) and 3.3 (sample T2) were obtained using ImageJ and more specifically with the orthogonal projection tool.

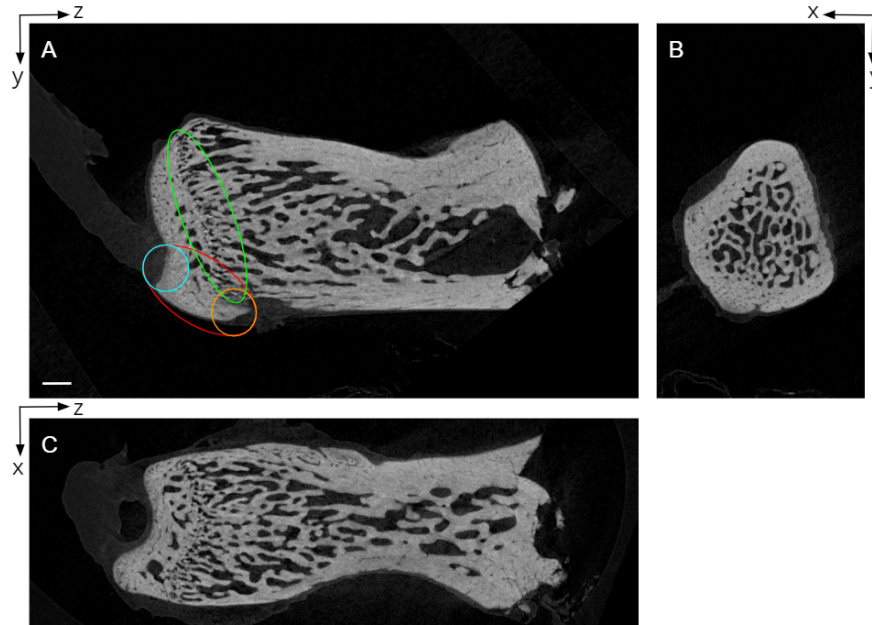


Figure 3.2: For an example slice of T1 sample (without contrast agent): Visualization of the three possible sections using ImageJ and its orthogonal projection tool : (A) Sagittal plane, (B) Coronal plane, (C) Transverse plane. Several zones are highlighted: **Tuberosity**, **Achilles Tendon attachment zone**, **plantar fascia attachment**, **Growth plate**. Scale bar: 500 μm .

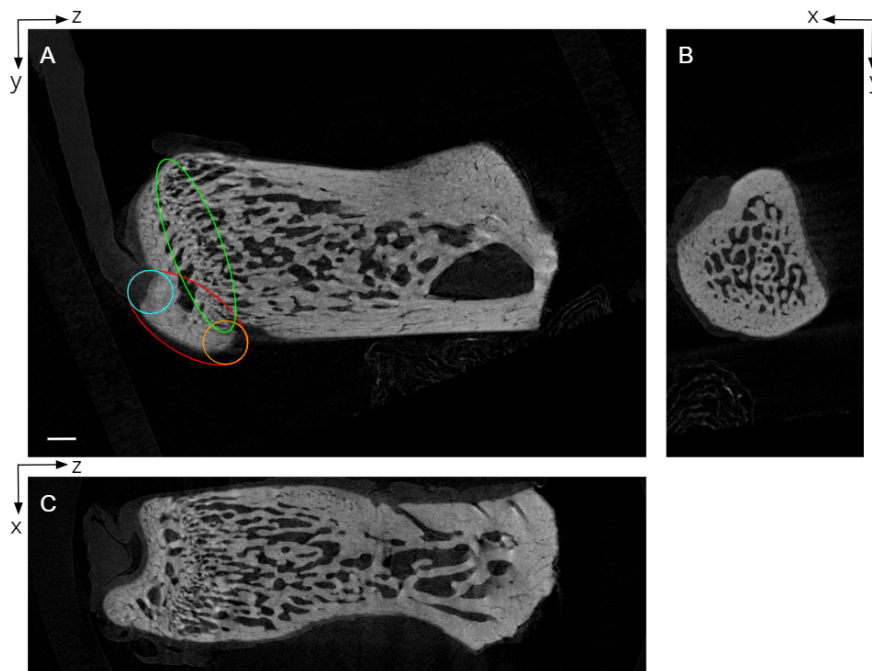


Figure 3.3: For an example slice of T2 sample (without contrast agent): Visualization of the three possible sections using ImageJ and its orthogonal projection tool: (A) Sagittal plane, (B) Coronal plane, (C) Transverse plane. Several zones are highlighted: **Tuberosity**, **Achilles Tendon attachment zone**, **plantar fascia attachment**, **Growth plate**. Scale bar: 500 μm .

The three plane sections for an example slice for both samples are presented. The majority of the bone observed is in fact the subchondral bone. As described in Chapter 1 (in the section about the region of interest), the Achilles tendon and plantar fascia attachment zone are located at the calcaneus. This particular region is clearly visible in the sagittal plane (encircled in red in the part (A) of both Figures) and it is also called the tuberosity here. Therefore, the slices from this section plane are used for the rest of this project. The two attachment zones are encircled in blue for Achilles tendon and orange for the plantar fascia in the part (A) of both figures. The growth plate, area of growing tissue near the ends of the long bones, is encircled in green in the part (A) of both figures. In part (B) (coronal plane section) of both figures, a relatively large layer of cortical bone surrounding the trabecular bone compartment can be assumed. Notice that the cut in sample 1 was coarser than in sample 2.

2.3 Assessment of the effect of the contrast agent

The next step is to analyze the impact of the contrast agent on the image quality. A second software is used: CTvox. Figure 3.4 shows a first comparison where the four different cases of scans (global view of the bone) without any additional filter. The only parameter modified is the contrast. In a first time, it has been calibrated in order to have the tendon and the bone visible on the same image for the case without staining. Then, the same parameter of contrast has been kept for the staining case. The difference between with and without contrast agent cases is already visible. The rendering with contrast agent delivers more details, the tendon is clearly as much visible as the bone. It is proof that the staining has been successfully. This staining also affects undesired tissue like fat tissue for example.

Figure 3.5 is a sliced bone version of the first comparison shown in Figure 3.4. It is already possible to notice some blurring effect in sample 2 with contrast agent, potentially due to possible micro-movements during the scan. Nevertheless, more contrast is visible in the cases with the contrast agent. In these cases, two main shades of gray can be observed. A light gray is associated to the regions where the contrast agent is present while a dark gray is associated to pure bone. This difference of gray intensity is explained by the fact that the stained tissue absorbs less x-ray than the bone during the scan. In both case, the insertion of the Achilles tendon is visible but it is clearly more visible with the contrast agent.

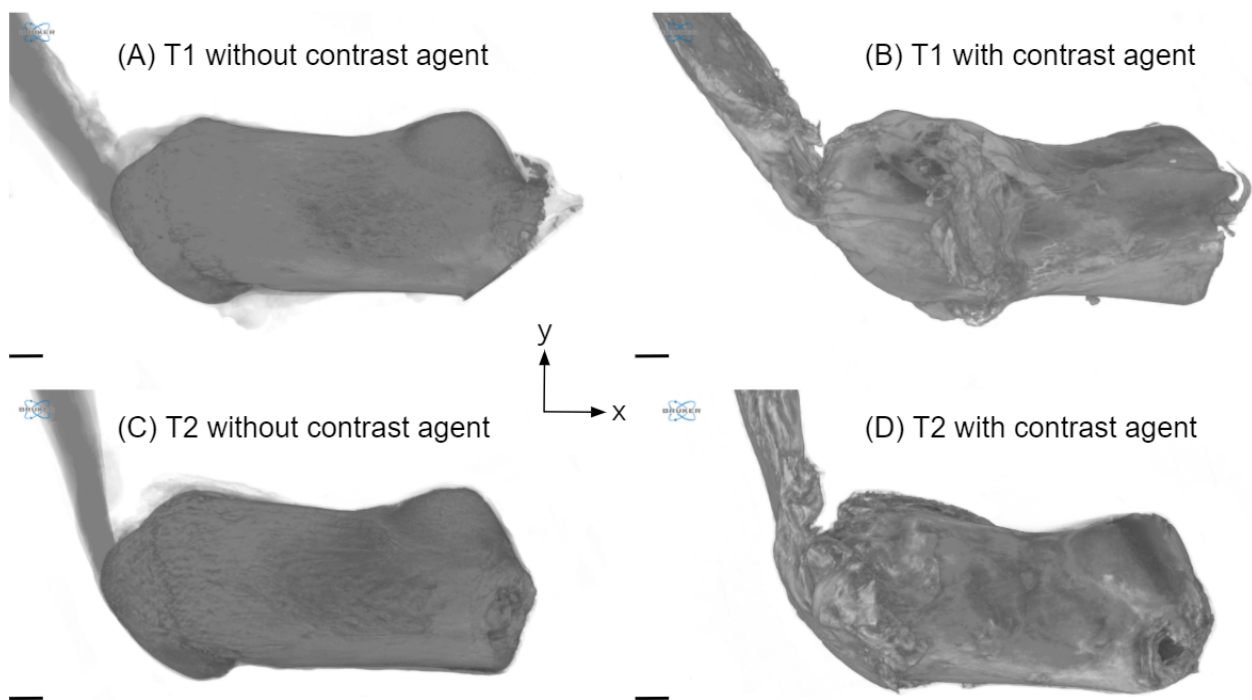


Figure 3.4: Global view without any cut for both samples: with and without contrast agent cases for two samples (T1 and T2) (no filter). Scale bar: 500 μm .

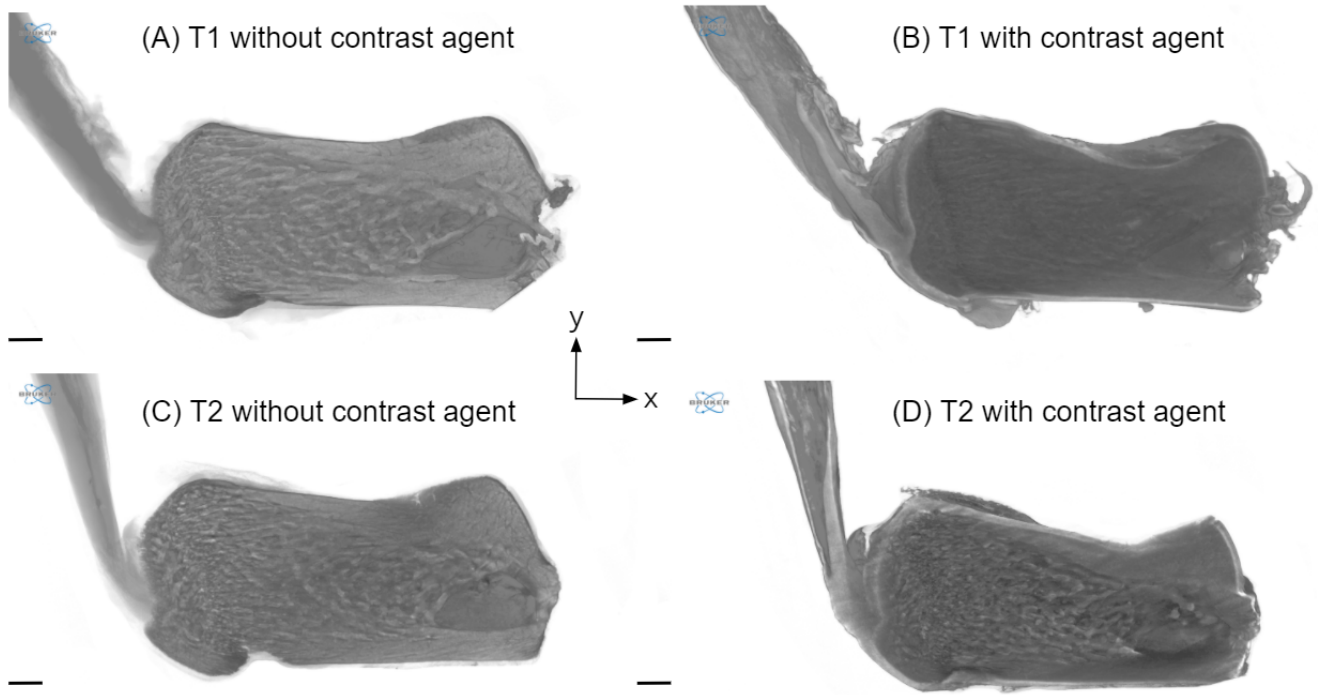


Figure 3.5: Global view with a cut for both samples: with and without contrast agent cases for two samples (T1 and T2) (no filter). Scale bar: 500 μm .

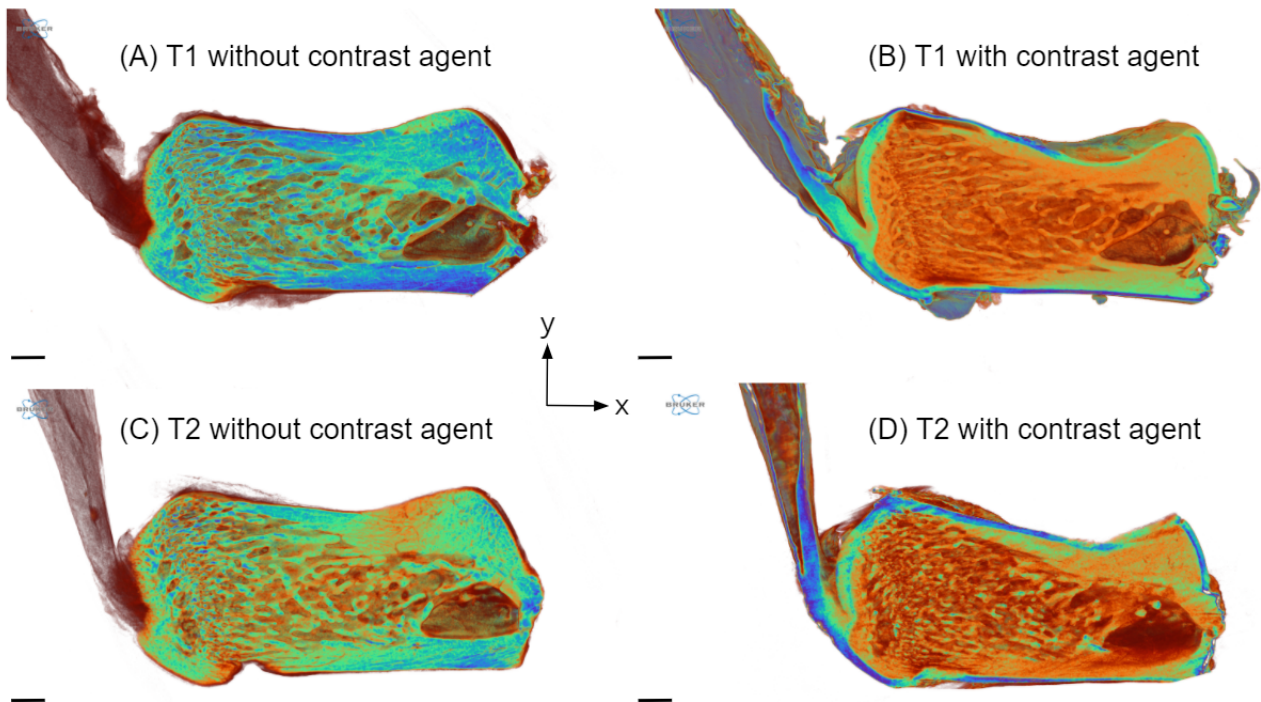


Figure 3.6: Global view with a cut for both samples (addition of a filter), with and without contrast agent cases for two samples (T1 and T2). Scale bar: 500 μm .

The next step is to introduce a filter to enhance visualization of the different components in the data volume. It highlights nicely the bone internal details in both cases and allows once again a nice tendon visualization in the contrast agent cases (Figure 3.6). Moreover, the color differences generated by the filter highlight nicely the insertion of the Achilles tendon even without contrast agent. Therefore, contrast agent can be seen as a second confirmation of what can be observed without. It confirms the tendon and the attachment zone identified without its staining. Nevertheless, some noise is created by its addition. Nevertheless, some noise, coming from undesired

strained tissues, is created by its addition. Consequently, the better visualization obtained using contrast agent does not balance the drawback of the noise. This is why we chose to work with the images without staining.

3 Insertion site morphology

The aim of this section is to present how the Achilles tendon as well as the plantar fascia attachment surfaces have been computed and quantified. Our goal is to develop a computational framework able to capture the three-dimensional irregularities of the surfaces. The method used is presented in a first section. It is based mainly on two softwares: CTAn and Matlab. CTAn is used to treat and extract specific regions of the μ CT images, while Matlab is used to reconstruct a 3D visual of the two attachment surfaces and quantify their areas. The results are then shown for several samples: the two coming from the experimental procedure described in Chapter 2 (T1 and T2), but also, in order to increase our statistical strength, five additional samples provided by Alexandra Tits (PhD student, University of Liege) with her authorization (A1, A2, A3, A4 and A5).

3.1 Method

The method followed to compute the area of attachment of both insertions (Achilles tendon and plantar fascia attachments) is described in this section. Notice that the sagittal section is used in this section

3.1.1 Image pre-processing

The aim of this pre-processing procedure is to treat and enhance the images for their further quantification in Matlab. Precise regions need to be extracted in order to effectively compute the attachment areas.

The first crucial step is to define a region of interest (ROI) for all the images of the stack. The choice is similar for both the attachment zones and consists of a circle centered at the middle point of the Achilles side or Fascia side of the tuberosity, of diameter equivalent to these side lengths. Figure 3.7 illustrates the construction principle of the ROIs. From this definition, a hypothesis is done: we assume that the region of both the tendon or the plantar fascia is spanning over the entire bone side (i.e. the full circle).

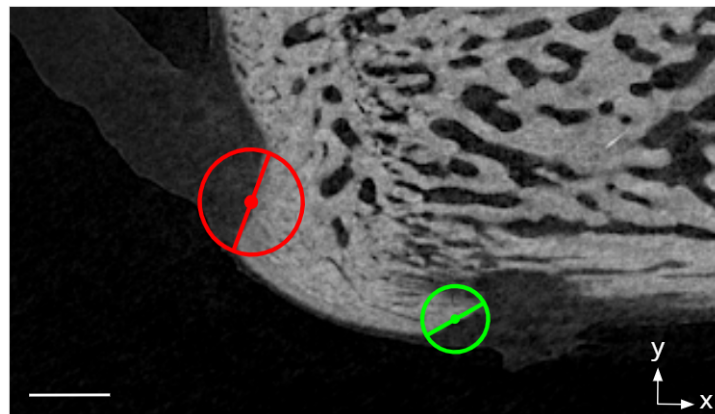


Figure 3.7: Illustration of the regions of interest. In red for the region of interest at Achilles side and in green for the region of interest at the plantar fascia side. Scale bar: 500 μ m.

A second essential parameter relates to the thickness of the soft tissues, or in other words over which depth the tissues are attaching. Following our first hypothesis, we suggest that the tuberosity is specifically localising the insertions, and that therefore the tissues attach over the full depth of the tuberosity. For the Achilles side, the tuberosity is considered to begin at the slice where it makes an angle higher 100° with the bone side. The ending slice is the one when the tuberosity has disappeared, in other words, when the bone side becomes flat. The two criteria are illustrated in Figure 3.8.

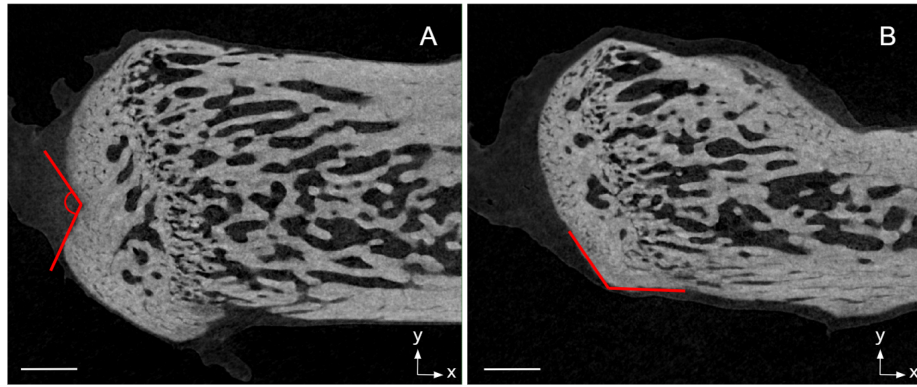


Figure 3.8: Illustration of the different criteria on two different slices for the Achilles tendon insertion. (A) starting criterion (B) ending criterion. Scale bar: 500 μm .

For the plantar fascia side, the beginning of the insertion is similarly defined when the angle between the horizontal axis and the right side of the tuberosity becomes greater than 30° . The ending slice is the one when the fascia side of the tuberosity becomes flat with the rest of the bone on the right side. The two cases are illustrated in Figure 3.9.

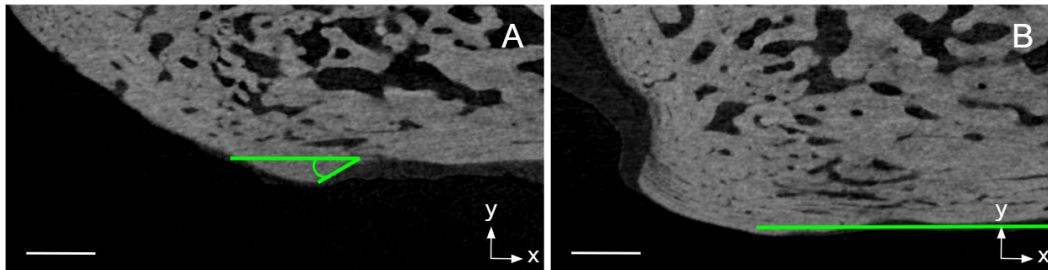


Figure 3.9: Illustration of the different criteria on two different slices for the fascia side. (A) starting criterion (B) ending criterion. Scale bar: 500 μm .

The next step is to apply a custom series of operations based on these regions of interest in order to extract two sets of images (in a BMP format): the bone region corresponding to the attachment area (for both Achilles and Fascia side) as well as the reverse images of the previous sets. Figure 3.10 shows these images respectively on the B and A part. In order to obtain such images, several treatment steps are required. It includes a filtering (Gaussian blur with a square kernel of 1.5 pixels), an automatic Otsu method thresholding, some despeckled filter (to remove small artefacts) and finally some morphological operations to remove bone pores without modifying its "surface".

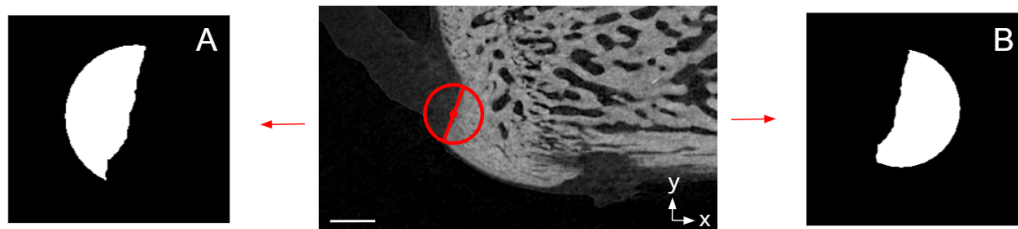


Figure 3.10: Illustration of the two groups of images extracted for the Achilles side (same procedure for the fascia side). (A) inverted attachment surface (B) attachment surface. Scale bar: 500 μm .

Another set of images is also saved, corresponding to the entire bone without taking into account the regions of interest and any morphological operations applied. An example slice is shown in Figure 3.11. Simply the same filtering, thresholding and despeckle are applied. It will serve for a visualization purpose later.



Figure 3.11: Whole bone image example. Scale bar: 500 μm .

3.1.1 Attachment area computation

The attachment area computation is done using Matlab. The code is divided into several parts. A first part is dedicated to the conversion and manipulations of the sets of images into matrices. The aim of this step is to obtain the attachment area in a matrix form. A second part is dedicated to the the meshing of the surface using this matrix. Because some errors are created during the meshing procedure, a cleaning procedure is realized. The final is step is the computation of the surface area.

▷ Image import and matrix conversion

As a reminder, the pre-processing procedure has led us to two sets of image for the attachment: the proper surface, but also its reverse. Let's call them respectively set A and B. The procedure being similar for both attachment regions, only the Achilles tendon one is fully described below.

Because of the BMP format, each image pixel is associated to a value corresponding to its gray level intensity value. At this point, each set is transformed into a three-dimensional matrix containing values equal to 0 or 255.

Then, in order to discriminate more easily between the two sets, white pixels (value 255) from the first one are assigned a value of 1, where as white pixels from the second set are replaced by 2.

Based on the processed sets of images, the attachment area is deduced as follow. To obtain that, a three-dimensional topology needs to be defined. First, the matrices of both sets are added together. The new matrix is fully checked to identify the position where an element value equals to 2 is found next to element value equals to 1. This is illustrated in Figure 3.12. A new matrix is created and has a 1 value each time the neighborhood criteria is met. This new three-dimensional matrix represents the attachment surface.

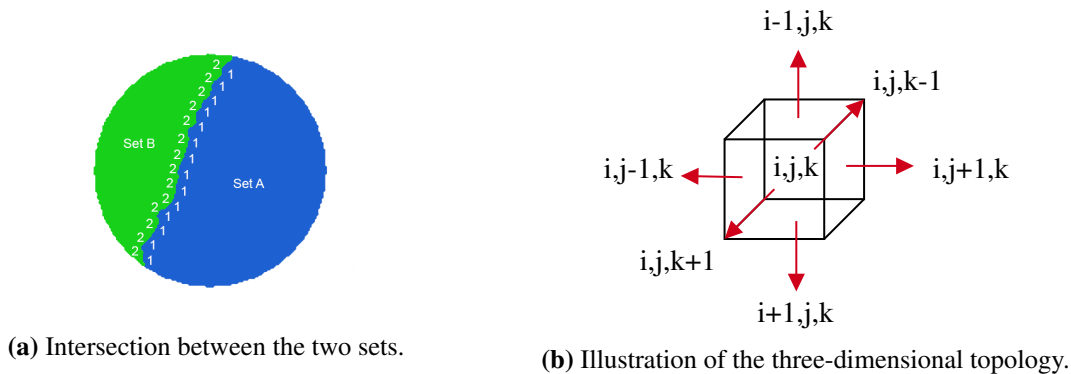
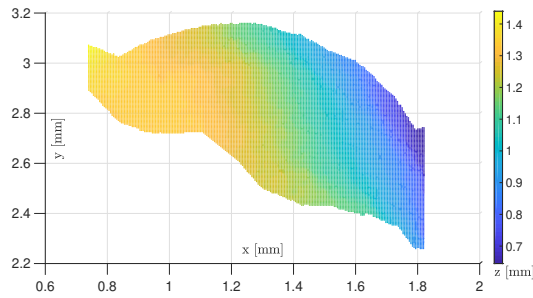


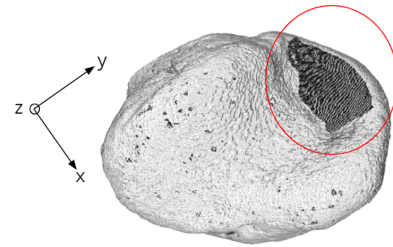
Figure 3.12: For an element at (i,j,k) position, each element in its neighborhood corresponding to each direction of the space is assessed to check whether a value of 1 is sitting next to a value of 2.

▷ Intersection visualization

From this matrix, we can already visualize the surface of attachment. First, using `scatter3`, a function that allows to display a three-dimensional cloud of points corresponding to the element values equal to 1 found in the attachment surface matrix. In Figure 3.13a, the result is shown for in x-y plane with a color bar specifying the z position in the perpendicular plane. In order to better visualize the result in three dimensions, `VolumeViewer` is used. A superimposition between the entire bone matrix and the attachment surface matrix is computed. Using this tool, it is possible to observe the attachment zone directly on the bone (Figure 3.13b).



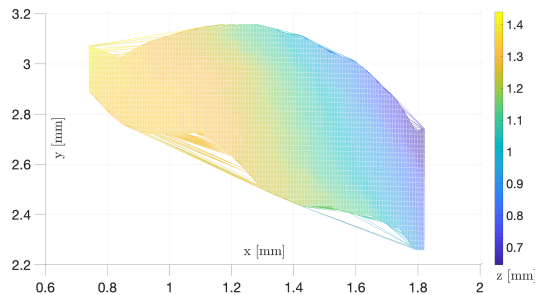
(a) Visualization using `scatter3` function.



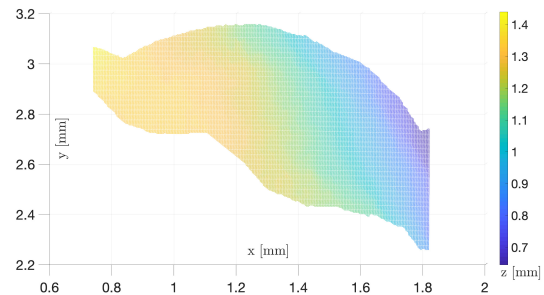
(b) 3D visualization using `VolumeViewer`.

Figure 3.13: Different way of visualization for the attachment surface at the Achilles side.

The next operation consists in deducing an area based on a cloud of points. To do so, a surface evaluation tool is used: the Delaunay triangulation (`delaunay` function). It is based on a fundamental property which is the Delaunay criterion, also called the empty circumcircle criterion in case of 2-D triangulation. Considering a set of points in 2D, a Delaunay triangulation of these points ensures that a circumcircle applied to each triangle created by connecting three points together does not contain another point in its interior [57] [55]. By using `trimesh`, a 3D visualization of the Delaunay triangulation result is possible. (Figure 3.14a) Again, the result is shown in the x-y plane with a color bar specifying the z position in the perpendicular plane.



(a) Undesired triangulations on the sides are observable.



(b) Corrected version of the meshed surface.

Figure 3.14: Visualization of the attachment surface on the Achilles tendon side. `trimesh` plot version.

▷ Cleaning procedure

By comparing Figure 3.13a and 3.14a, some undesired triangulations, that would result in an overevaluation of the area, are observable. The next part of the code consists to delete these undesired effects.

It is done in two parts. The first one consists in extracting the 3D contour from the 3D points cloud. It is a homemade script based on the basic manipulation on the attachment matrix using notably `min` and `max` functions. The general working principle is the following: the matrix is firstly scanned along the x direction: for each x coordinate the maximum and minimum y are retained with all their possible z coordinates. The matrix is then scanned along the y direction: for each y coordinate the minimum and maximum x are retained with all their possible z coordinates. The final result is presented in Figure 3.15. By knowing the 3D contour, it is possible to eliminate the undesired triangles.

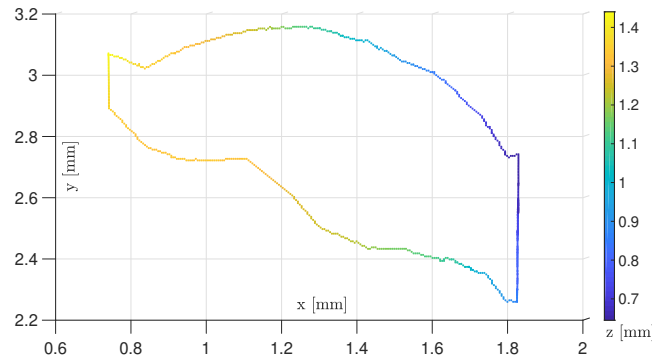


Figure 3.15: 3D contour plot using `scatter3` function.

From the `delaunay` function, one matrix is obtained called the TRI matrix. It has three columns corresponding to three points indexes that are the edges of a triangle. There are as many rows in the matrix as there are triangles created by the Delaunay triangulation. The contour vector simply contains the index of the contour points.

Each resulting point of the triangulation is compared with the contour points. Indeed, as seen in Figure 3.14a, contour points are the ones that seem to generate the errors. To verify whether a contour triangle is a mistake, we check if its lengths are aberrantly big, that is, the three side lengths are calculated and confronted to a threshold. It is equal to the highest side length possible among the acceptable mesh triangles. If one of them is greater, the corresponding triangle is discarded. The final result is shown in Figure 3.14b by using again the `trimesh` function.

▷ Intersection quantification

The final step of the code is to calculate the area of the surface. Since the surface is made of multiple triangles, its area is equal to the sum of all the triangle areas. A triangle area is calculated using the cross product of its two sides vector divided by 2. The final result is multiplied by $5 \mu\text{m}^2$ in order to take the original μCT scan resolution into account.

This method is applied in the same way for the Achilles tendon and the plantar fascia attachment.

3.2 Results

This section aims to present the different results from this chapter.

Firstly, images of both attachment surfaces for one sample are shown using VolumeViewer. In a second time, a table containing all surface area values of both attachment surfaces for each sample are shown. In total 4 different rats are investigated through these samples: T1 and T2 for rat 1, A1 for rat 2, A2 and A3 for rat 3 and finally A4 and A5 for rat 4.

Attachment surfaces visualization

The images coming from VolumeViewer app were privileged. Figure 3.16 shows the results for the plantar fascia (A) and the Achilles tendon (B) attachment surface on the bone for (T1) sample. From this image, it can be seen that the tuberosity region is perfectly shaped to receive the attachment of both the plantar fascia and the Achilles tendon. (The rest of the results can be found in the Appendix)

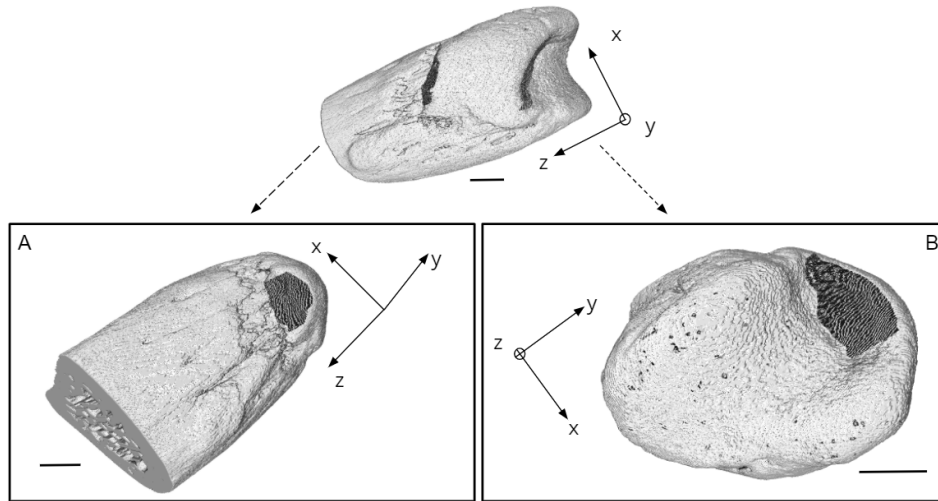


Figure 3.16: For T1 sample: Visualization of the plantar fascia (A) and Achilles tendon (B) attachment surfaces using VolumeViewer. Scale bar: 1 [mm] (*approximately*).

Attachment surfaces area values

Figure 3.17 shows the resulting attachment surface area values for both Achilles and Fascia sides.

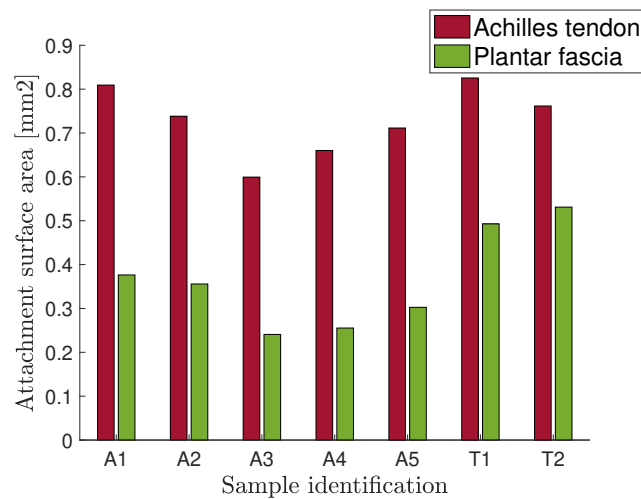


Figure 3.17: Bar plot of results of Achilles and plantar fascia attachment surface areas for seven samples available.

The detailed results are found in the Appendix. The results of the attachment surface areas are varying from one sample to another. Again, the variability is higher for the plantar fascia side with values from 0.2408 [mm²] to 0.5311 [mm²]. For the Achilles side, the values vary from 0.5995 [mm²] to 0.8255 [mm²].

In terms of statistics, for Achilles surface side, the mean is 0.7294 [mm²] and the standard deviation is 0.0803 [mm²], for the plantar fascia side, the mean is 0.3650 [mm²] and the standard deviation 0.1122 [mm²]. It means that the ratio between the two surfaces is, in mean, equal to 0.5004.

4 Discussion and conclusions

The aim of this section is to propose a critical discussion about the method and results developed in this chapter. A conclusion about the most relevant findings is also done.

The interest of using the contrast agent was the first question of this project. Without the contrast agent, the bone, its internal details (trabecular bone, growth plate ...) and the tuberosity were easily identified on the 3D rendered volume. By tuning the render contrast, the tendon as well as its attachment to the tuberosity were highlighted. Nevertheless, the tendon part remained blurry. By addition of the staining procedure, each of these parts were much more visible, especially the tendon part and its attachment, confirming what was observed without its use. It supports the hypothesis that the attachment region of both the tendon or the plantar fascia is spanning over the entire bone side despite the lack of literature about the question. Unfortunately, the contrast agent had not only penetrated the tendon and bone tissues but also the undesired tissues remaining from the extraction, like fat tissue for example. As a consequence, it created noise in the images. A solution would have been to be more cautious during the extraction process. But due to the small size of the samples manipulated as well as the risk of damaging of the attachment of the Achilles tendon to the bone, a deeper cleaning was more difficult. For these reasons, we choose to work only with the μ CT scan images obtained without contrast agent.

The method used to determine the attachment surface area remained experimental. The first step of the process, the image pre-processing was a critical one but it was completely operator dependent. The operator had to put correctly the ROI on every slice of the stack. It was sometimes an hard task due to the high shape variability of the tuberosity especially for the plantar fascia side. Some papers in the literature proposed similar methods. For instance [2] and [22], proposed a method to calculate the surface area of the supraspinatus tendon attachment to the humeral head for a rabbit. It was based on the definition of two regions of interest. A first one was representing the surface of the bone. It was obtained using a semi-automated implementation of a snake contouring algorithm. The second region of interest was the volume intersecting the outer edge of the tendon attachment and the first region of interest. The edge of the tendon attachment was visually determined by an operator. The two regions were then meshed using Matlab and the cgalsurf library. Finally the triangles total surface contained in the intersection of the two regions were considered as the attachment area (Figure 3.18). This process was based on three-dimensional regions of interest while our method was based on a two-dimensional approach. It can be noticed that this method was also a lot operator dependent for the determination of both regions of interest, even more for the second one.

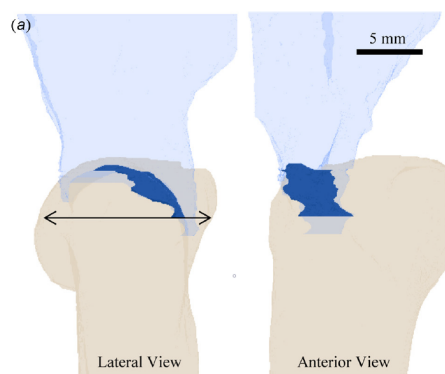


Figure 3.18: Superimposition of μ CT scan of the humeral head and the supraspinatus tendon of a rabbit. The attachment area is highlighted in blue for both lateral and anterior views [2].

As mentioned from [2] and [22], a meshing method based on triangular elements was used. In our project, a meshing procedure based on triangles element was also considered with the Delaunay algorithm. Unfortunately, undesired triangulations on the resulting meshed surfaces were also created in the process and therefore a method to correct this issue was required.

The results showed a certain variability, with a standard deviation remaining close to $0.1 \text{ [mm}^2\text{]}$ for both Achilles tendon and plantar fascia attachment surface. It remains acceptable knowing the shape variability between the samples. On average, the ratio between the two attachment surfaces was 0.5. The 3D visualizations of the attachment surfaces directly on the bone highlighted nicely the fact that the tuberosity was well shaped to allow the attachments on its two sides. This observation also reinforced our initial hypothesis about them.

Chapter 4

Global parameters analysis (continuum model)

1 Introduction

This chapter is the first one out of three about the investigation of the biomechanical behavior of the calcaneus under different boundary conditions. Only the bone side of the interface is investigated for this project thus a simplified two-dimensional continuum model of the bone will be considered. The Achilles tendon and plantar fascia are not included in the geometry instead they are considered through realistic boundary conditions.

This preliminary analysis has several goals. Mainly, the influence of several boundary conditions is investigated. Two sensitivity analyses are realized: firstly, about the orientation of the force at the Achilles tendon and secondly, about the force intensity at the plantar fascia. This ensures us to choose the most realistic cases for our further studied cases. However, simulating this simplified continuum model already allows us to characterize how stresses are distributed within bone. More specifically, because the continuum model includes exclusively the global bone shape, the influence of the tuberosity geometry (i.e. how it is extruding from the bone surface) can be emphasized.

A first section is focused on presenting our method, including the geometry, meshing, material properties definition and the boundary conditions notably. Then, the results for two different sensitivity analyses are presented and discussed.

2 Methods

The following biomechanical analyses are performed for one representative cross-section coming from sample T1 (n° 1313). The chosen cross-section illustrates a nice tuberosity shape for which Achilles and plantar fascia attachments are clearly visible.

The method exploited to compute stresses within bone is called the Finite Element Method (FEM). The Finite Element Method is a numerical technique which emerged at the early 20th century. It is based on the fundamental principle developed by Ritz and Garlekin. The general aim of the FEM is, for a given system, to compute its solution by solving a set of algebraic equations instead of a complex initial partial differential equations system. In other words, the FEM consists in translating a continuum problem into a discrete one. The system is not characterized anymore by an infinity of degrees of freedom but instead is restricted to a certain number of degrees of freedom and a set of discrete points called nodes. [43] The displacement of the whole system is then characterized by an approximation of a combination between the displacements of these nodes. A stiffness matrix is defined to link these displacements to the external forces applied on the system. In order to define this matrix in an efficient way, the system is divided on several sub-units corresponding to a simplified geometry. These sub-units are called elements. The displacements of each node of a particular element are linked to the external forces applied on these nodes. Therefore, a stiffness matrix can be defined for this particular element and thus for all the elements in a same way. The assembly of all these stiffness element matrices gives a large and sparse matrix which characterizes the stiffness of the system globally. A critical parameter can be fixed by the user: the element type. Indeed, it exists several kinds of element, from triangle to quadrilateral elements, characterized by a certain

order depending on how much nodes they include. Each of them provides a variable performance depending on the geometry involved. A mesh convergence analysis is often done in order to find the best element type suited to a certain problem. It consists in testing several combinations between type and size of elements and finding the best combination in term of errors generated and computation time.

For this chapter, Ansys Workbench is used.[3] It is a very intuitive platform that proposes a entire workflow process to perform finite element simulations and analyses.

2.1 Geometry

As mentioned before, the cross-section n° 1313 of sample T1 (low resolution) is used as basis for the simplified continuum model. The app SpaceClaim from Ansys is used to generate this model. Starting from the cross-section (part (A) of Figure 4.1), a .stl file is extracted directly from CTAn. This .stl file is used as input in spaceClaim. Its contour is extracted and simplified to get smooth borders. Finally, the contour is filled to finish the continuum model (part (B) of Figure 4.1).

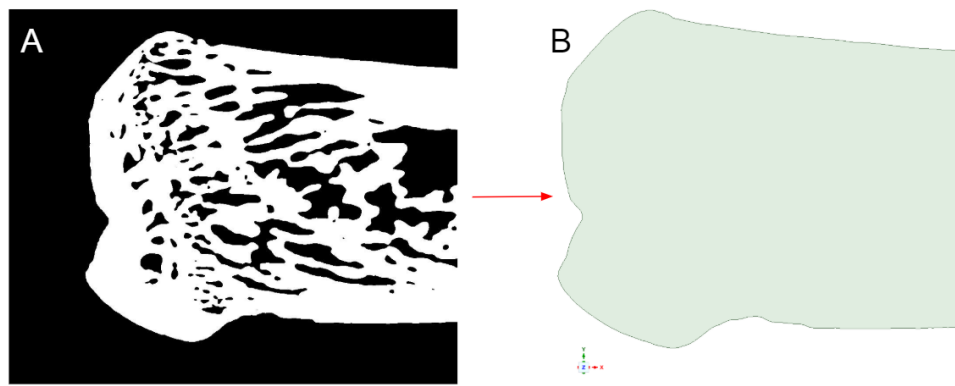


Figure 4.1: Transformation of the cross-section n°1313 of T1 sample (A) into the two dimensional continuum model (B).

2.2 Material properties definition

For this project, the bone is assumed to behave as an isotropic and linear elastic material. The linear elasticity assumption is acceptable because we are working with small deformations. The isotropy is more tricky to justify. Indeed, the bone is clearly an anisotropic material because of its no-uniformity in every direction due to its architecture (see Chapter 1). The trabecular bone shows different Young's Modulus depending on the loading direction and the trabecular architecture seems to be oriented with respect to it. For this continuum case, the architecture is simplified by neglecting porosity. Therefore, porosity should somehow be included through a lower than physiological Young's Modulus. Otherwise, tissue stiffness would be largely over-estimated [21]. Values reported in literature are included in the interval 5 to 25 [GPa] for Young's modulus at the bone tissue level [48] [32]. We choose to work with 1 [Gpa] as Young's modulus for our simplified continuum model. Poisson's ratio is, as commonly, set to $\nu = 0.33$ [71].

2.3 Boundary conditions

The boundary conditions are a set of parameters crucial to defined. For this chapter, two sensitivity analyses are realized, two sets of boundary conditions are therefore required and described in this section. Notice that, for both cases, the plane stress is set. In order to avoid any singularity in the model arising from rigid body motion, one needs to fix the bone at some location. It was chosen to encastre the lateral side of the bone for several reasons. Indeed, our region of interest is mainly focused around the insertion. Therefore, the lateral side of the bone is the farthest region from it and we can assume boundary effects will have minimal impact on our results.

Case I: Orientation of the applied force at the Achilles tendon

In order to mimic the evolution of stress distribution during a gait cycle or whenever the orientation of the force arising from the tendon changes, the influence of the force orientation at the Achilles tendon on the resulting stress distributions is investigated. An additional force at the plantar fascia side is also considered for physiological consistency. Its orientation is maintained horizontal through all the simulations.

In order to calculate the intensity of the two forces, the following reasoning is applied. First, the force to apply on the side of the Achilles tendon is set. As described in Chapter 1, cortical bone has in tension, a longitudinal ultimate stress equals to 130 [MPa] and a transverse ultimate stress equals to 50 [MPa] and in compression, a longitudinal ultimate stress equals to 190 [MPa] and a transverse ultimate stress equals to 130 [MPa]. [76] Moreover, the failure stress of Achilles tendon is around 50 [MPa]. [54]

Having a stress of 30 [MPa] being applied at the Achilles tendon seems thus to be a reasonable choice. This stress value is translated into a force boundary condition by multiplying it to the surface on which it has to act. In this case, we know that the force has to be applied on the entire left side of the tuberosity (depicted in green in Figure 4.2a). This segment length is equal to 0.6529 [mm] in the case of the considered cross-section. Taking the assumption that the cross-section is 1 μm thick, it gives a surface of $6.529\text{e-}4$ [mm^2] and therefore a force of 19.587 [mN]. Three orientations of this force are investigated: 180° and 90° , two extreme cases and 135° , a case closer to reality. (depicted respectively by blue, red and cyan arrows in Figure 4.2a)

Regarding the force intensity at the plantar fascia side, results of our structural analysis are exploited. Indeed, because very few literature is available regarding the plantar fascia, we assume that the force arising from a ligament or tendon is proportional to its area of attachment. More specifically, the force applied by the plantar fascia is supposed to be reduced proportionally to its reduction in attachment surface, when compared to the Achilles tendon. For T1 sample, the attachment surfaces for plantar fascia and Achilles tendons are equal respectively to 0.4995 and 0.8328 [mm^2]. The ratio between these two values is equal roughly to 0.6. This ratio is then multiplied by the computed value of the force for the Achilles tendon, which gives a force of 11.747 [mN]. This value is the force at the plantar fascia side.

This force is applied at the right side of the tuberosity (depicted in purple in Figure 4.2a). By proceeding this way, we take into consideration not only a shape parameter of the actual used cross-section but also information coming from a 3D point of view.

Case II: intensity of the applied force at the plantar fascia

Our second analysis focuses on the plantar fascia and its influence on the global stress behavior. This is done by imposing a growing importance to the force arising from it. Specifically, in addition to the previously mentioned proportional force, we simulate two additional cases: no plantar fascia at all, and a plantar fascia with a force as high as the Achilles tendon one. (Depicted respectively by orange, no arrow and dark red arrows in Figure 4.2b)

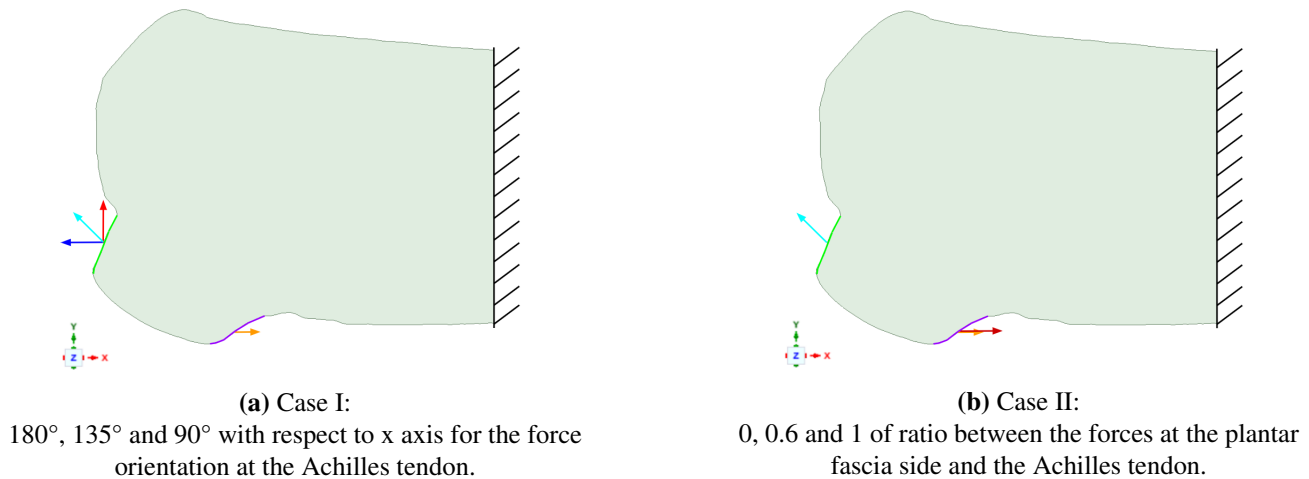


Figure 4.2: Illustration of the boundary conditions for the two investigated cases.

2.4 Mesh convergence analysis

Once geometries were built and boundary conditions set, the model needs to be meshed. A common step in FE analysis is to proceed with a mesh convergence analysis. The aim of this analysis is to choose the type and size of element that is the best suited to the model under investigation. In addition to this analysis, quality factors can be assessed to reinforce the choice. Several kinds exist but for this analysis only one was retained: the aspect ratio. The aspect ratio quantifies how much the sides length of an element differ from each other. In other words, it is defined as $R = l/s$ where l is the longest edge and s is the shorter edge of an element. Consequently, a value close to 1 means a good quality element because of its regular shape.

For this analysis, boundary conditions need to be defined and maintained constant. A force with 135° orientation with respect to the x axis is applied at the Achilles tendon with an intensity equal to 19.587 [mN] (defined in the previous section) and a force of 11.747 [mN] is applied horizontally at the plantar fascia (0.6 of ratio). The nodes on the right side of the bone are also fixed in the two directions of space like usual.

The triangular elements are directly eliminated from the analysis. Indeed, as shown in Figure 4.3, T6 elements (Triangular elements, quadratic order) show a very heterogeneous distribution in the elements quality in terms of aspect ratio. Therefore, an automatic meshing based on a quadrilateral dominant meshing is tested. Two options are proposed for this mode: a mix between triangular and quadrilateral elements and quadrilateral elements only. The first and second order of these elements are tested.

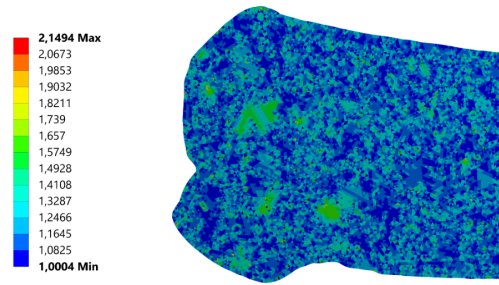


Figure 4.3: Visualization of the aspect ratio for T6 elements only (a value close to 1 means good quality element).

The mesh convergence analysis consists in progressively reducing the size of the elements while recording the displacement at the nodes where the forces are applied. When the curve converges near a stable displacement as the element size decreases, it means that the element size does not affect anymore the mechanical response of the model and the element size can be fixed in that range. This analysis is depicted in Figure 4.4a for the Achilles tendon and in Figure 4.4b for the plantar fascia side. Two analyses are conducted in parallel due to the two force boundary conditions.

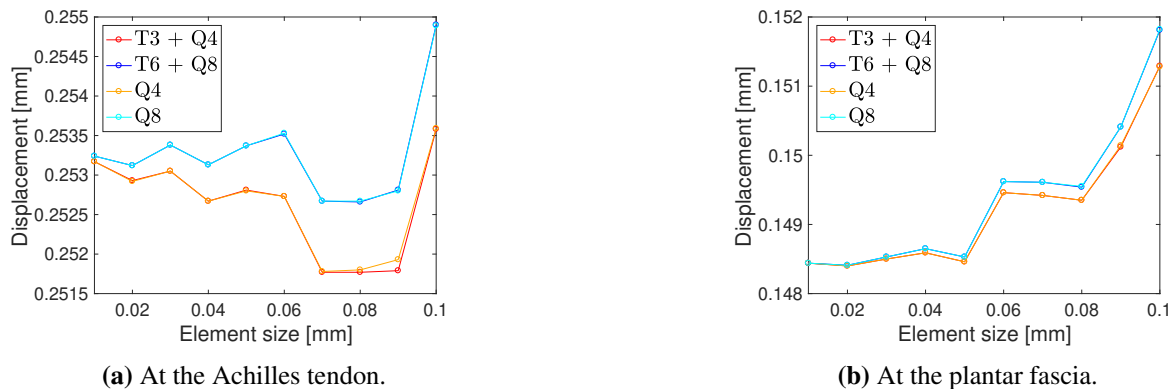


Figure 4.4: Comparison of the results for the mesh convergence analysis obtained for both sides of the tuberosity.

From Figure 4.4, a first observation is that almost no difference can be seen between the two cases for first order elements (namely a mix between triangular elements (T3) and quadrilateral elements (Q4) or only quadrilateral elements (Q4) elements cases) as well as for the second order elements (namely a mix between triangular elements

(T6) and quadrilateral elements (Q8) or only quadrilateral elements (Q8) elements cases). This is explained by the very few quantity of triangular elements created in the case of the mixed element type. Displacements do not vary extensively from 0.06 [mm] element size for the Achilles tendon and starts to converge to 0.05 [mm] for the plantar fascia. Therefore, to avoid high computational cost, a size of 0.04 mm is chosen.

After that, the element order has to be fixed. At the Achilles tendon, the convergence is a bit more stable for the quadratic order than for the linear order. Thus, the quadratic order is chosen. The final choice relates to the element type. Figure 4.5 illustrates the aspect ratios for the two quadratic element types. Figure 4.5b, Q8 elements only, shows better results than Figure 4.5a, which contains a mix between T6 and Q8 elements, in terms of aspect ratio, with a better homogeneity in perfectly shaped quadrilateral elements (aspect ratio close to 1). Therefore, the Q8 elements with a size of 0.04 [mm] are chosen.



(a) Aspect ratio for a mix between Q8 and T6 elements.

(b) Aspect ratio for a mix between Q8 elements.

Figure 4.5: Comparison of the results for the aspect ratio for two kinds of elements configuration.

2.5 Regions of interest

From the mesh created, two regions of interest are delineated. The first is the tuberosity region, where the insertions are located, and the second is the whole bone region region (represented in Figure 4.6). Notice that a part of the model is excluded from the whole bone region to avoid boundary effects where a fixed support is applied. This excluded region is defined to start at the middle distance between the right side of the tuberosity and the end of the bone (see illustration in Figure 4.6).

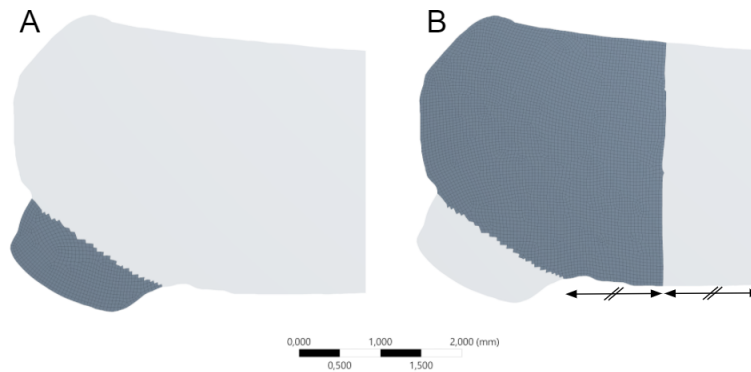


Figure 4.6: Definition of the two regions of interest on the mesh. (A) tuberosity region (B) whole bone region

2.6 Solver features

This created FE model contains 8088 elements and 24605 nodes. It was solved using Mechanical of Ansys on a computer equipped with a Intel®core™i7-4790K CPU 4.00 [GHz] with 32 [GB] of RAM. Total CPU time required to achieve the simulations does not exceed 2 [s] in average.

2.7 Outputs exportation

When the simulations are completed, qualitative observations can be done by using visualization tools, like contour plots, directly in Mechanical. The goal is to observe the stress distributions. Three outputs are examined: the equivalent stresses (Von-Mises), the maximum stresses, and the minimum stresses. While the first output is more associated with shear, maximum and minimum stresses give information about tension and compression regions. The stress results at the nodes are then exported in a `.txt` file and used as an input for a Matlab script. This script generates the histograms of the different outputs for the two regions of interest. Thanks to them, the frequency distribution of stresses are investigated. These histograms are normalized in order to have the area under the curve equal to 1 to ensure a fair comparison between the cases.

3 Results

The aim of this section is to present the outputs results for the two sensitivity analyses. For each stress output (equivalent stresses (Von-Mises), maximum and minimum principal stresses), contour plots as well as stress distribution plots are shown.

3.1 Case I: Orientation of the applied force at the Achilles tendon

In this section, the results concerning the sensitivity analysis conducted at the Achilles tendon are shown. The outputs results are presented for three different orientations of the force at the Achilles tendon : 180° , 135° and 90° with respect to the x axis.

Equivalent stresses (Von-Mises)

Figure 4.8 shows the contour plots for the equivalent stresses (Von-Mises) for the three orientations of the force at the Achilles tendon : 180° , 135° and 90° with respect to the x axis.

Considering the 180° orientation case (Figure 4.8a), it can be seen that the stresses remain concentrated within the tuberosity. This is explained by the fact that the tuberosity is uni-axially loaded along the x axis with two forces in opposite directions. Considering that the intensity force at the plantar fascia is 60 % of the force intensity at the Achilles tendon, a higher stress concentration is observed on the left side of the tuberosity than on its right side.

When the force at the Achilles tendon starts to be more vertically oriented, the stresses begin to spread in the whole bone. Logically, this propagation is even more marked for the 90° (Figure 4.8c)) than for the 135° orientation case (Figure 4.8b)). This is due to the lever arm effect. This effect is based on torque creation which induces a rotational motion of an object. A torque is defined by the applied force multiplied by a lever arm. This lever arm is the perpendicular distance from the line of action of the force to the rotation axis. This is illustrated in Figure 4.7. For the 90° orientation case, a larger lever arm and thus a greater induced torque is observed than in the 135° orientation case. Therefore, an increased rotation movement of the bone inducing a greater stress distribution is visible for the 90° orientation case than in the 135° orientation case.

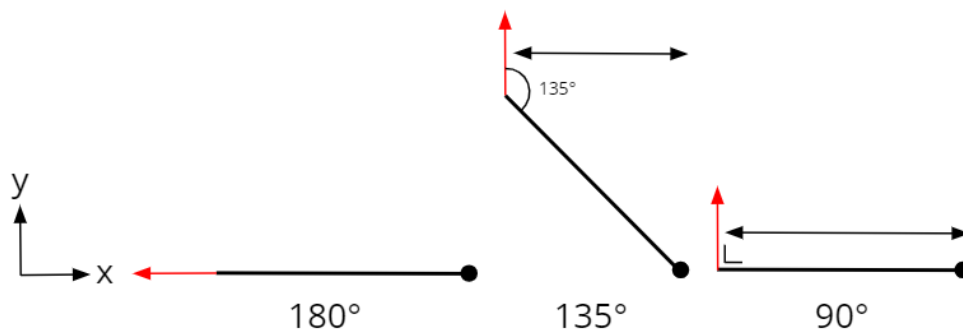


Figure 4.7: Illustration of the lever arm effect for the three force orientation cases.

Some boundary effects, with high stress concentrations regions, can be seen on the inferior and superior edges of the right side of the bone.

A more accurate representation of the results is provided with distribution plots 4.9. In the tuberosity region, depicted in Figure 4.9a, the smallest mean equivalent stress is associated to the 180° orientation case while the 135° and 90° orientation cases exhibit both similar values. They are increased by 35 % in comparison to the first case. This is explained by the apparition of the lever arm effect in these last two cases. For the standard deviations, the highest value is found for the 90° orientation case because there is a lot of heterogeneity inside the stress distribution at the Achilles tendon where the force is applied. Indeed, on one side this force induces a lever arm effect and on the other side there is a smaller force at the plantar fascia side which counteracts the first one. Considering the 135° orientation case, these two effects are more balanced between each other, decreasing the stress concentration at the Achilles tendon. Therefore, the standard deviation is lower for this case.

In the whole bone region (Figure 4.9b), a progressive shifting of the curves to the right is observed with increasing applied force angle. Consequently, the mean stress and standard deviation values increase too. It is explained by the progressive importance of the lever arm effect when the angle of the force applied at the Achilles tendon increases.

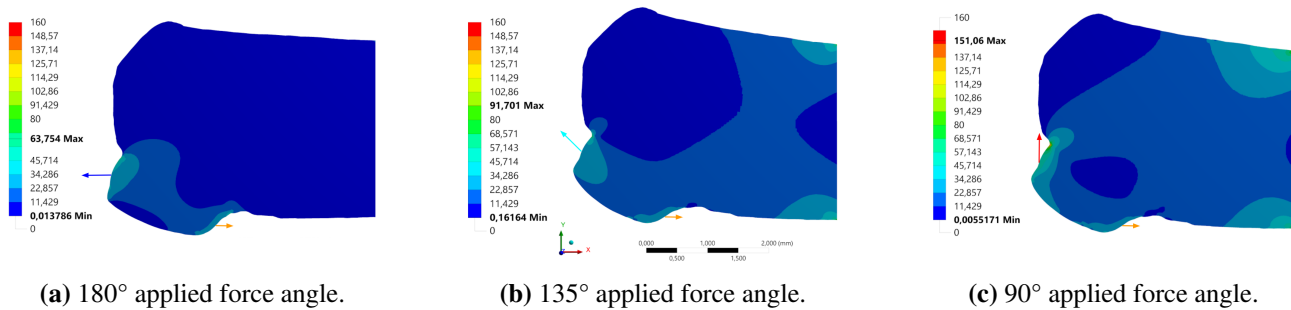


Figure 4.8: Contour plots of the equivalent (Von Mises) [MPa] stress for a varying angle of the force applied at the Achilles tendon (constant force with a ratio of 0.6 at the plantar fascia).

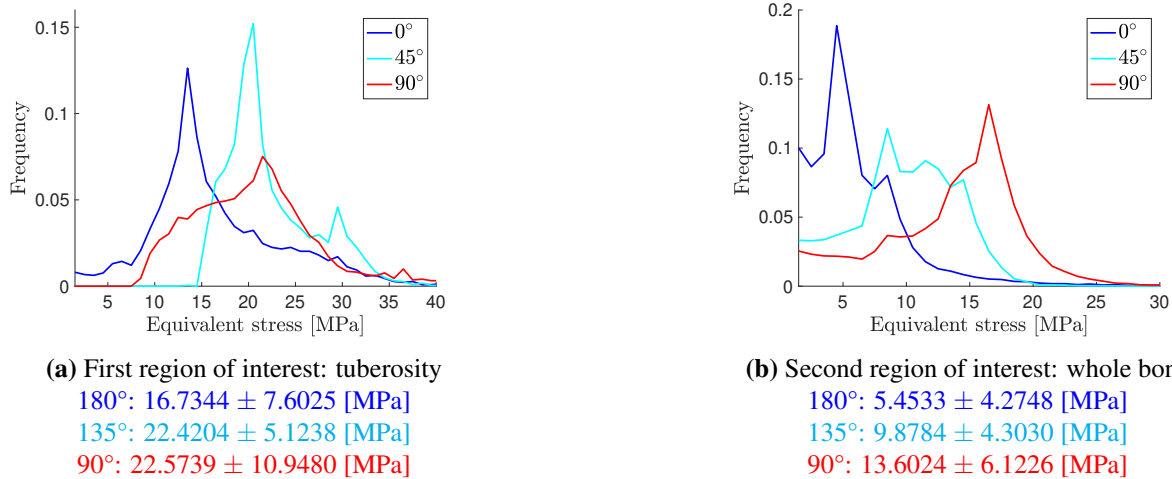


Figure 4.9: Comparison of the results for the equivalent stresses (Von-Mises) distribution obtained for both regions of interest. The means and standard deviations are also mentioned.

Maximum and minimum principal stresses

As already mentioned, maximum principal stresses provide information about regions in tension while minimum principal stresses are linked to compression dominated regions. Thanks to Von-Mises stresses visualization, a lever arm effect with increasing angle was identified. As illustrated in Figure 4.10, this should also lead to clear tension and compression regions.

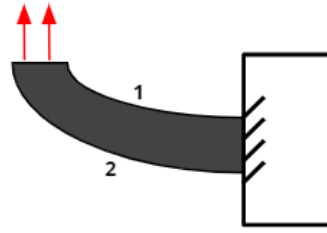


Figure 4.10: Illustration of the lever arm effect for a 2D piece pulled up vertically. Two kinds of stresses found: (1) side in compression (2) side in tension.

Those regions can indeed be visualised. Figure 4.11 presents the contour plots of the maximum principal stress for an increasing force angle. As can be observed in those figures, a region in tension is appearing at the bottom of the bone for cases implying a lever arm effect. Those regions can indeed be visualised in the 135° and 90° orientation cases, in Figures 4.11b and 4.11c. For the 90° orientation case, the force at the plantar fascia side being perpendicular to the one at the Achilles tendon, it counteracts the lever arm effect in way that seems to concentrate the tension within the tuberosity. The 135° orientation case allows a more homogeneous stress distribution.

Concerning the 180° orientation case, the tension region is consistently concentrated within the tuberosity because this part is loaded by two opposite forces on its two opposite sides (shown in Figure 4.11a). The force on the Achilles tendon being greater than the one at the plantar fascia side, the stress concentration is greater on the first than on the second side.

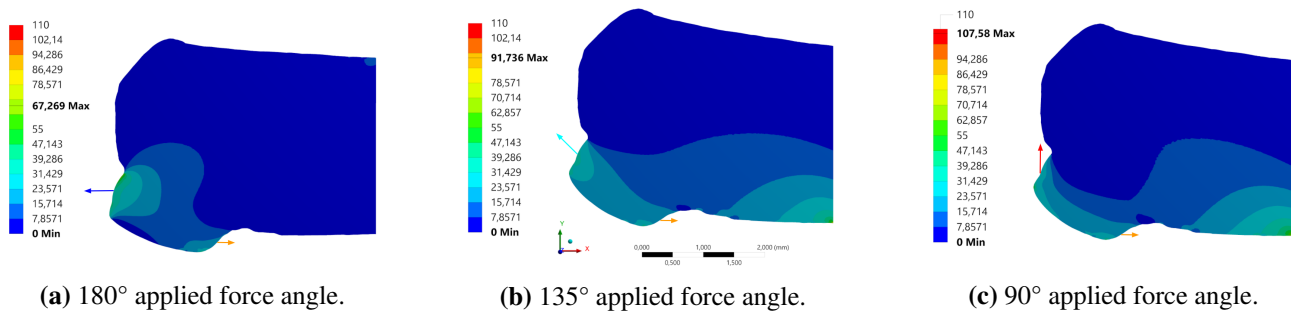


Figure 4.11: Contour plots of the maximum principal stress for a varying angle of the force applied at the Achilles tendon (constant force with a ratio of 0.6 at the plantar fascia).

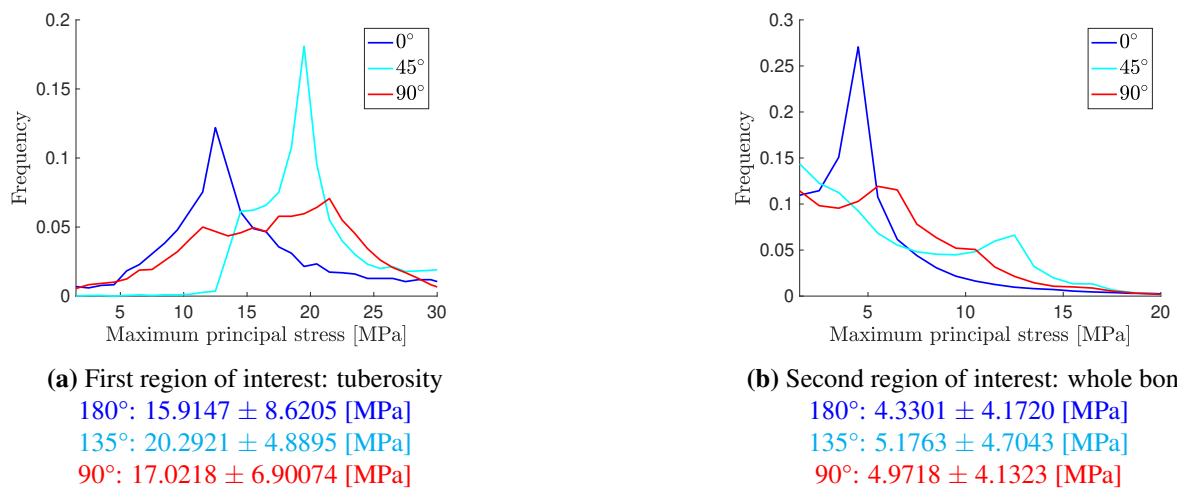


Figure 4.12: Comparison between the results for the maximum principal stresses obtained for both regions of interest.

Figure 4.12 shows the frequency plots of the maximum principal stresses distributions for both regions of interest. For the tuberosity region, the curves show the same trend than the ones for the equivalent stresses distribution

(Figure 4.12a). For the whole bone region (Figure 4.12b), the curves reflect the observations explained for the contour plots above (Figure 4.11). For the 180° orientation case, tension stresses overflow a bit from the tuberosity region where the major stress concentration is observed. The 90° orientation case shows smaller values in terms of mean for the maximum stress and its standard deviation than the 135° orientation case. It is induced by the fact that the stresses are more concentrated in the tuberosity in the first case than in the second.

Figure 4.13 shows the contour plots of the minimum principal stresses for the three orientation cases. Overall, no significant compression stresses can be observed. In the cases of 180° and 135° orientation small areas of compression stresses are spotted, due to the geometry of the edges connecting the tuberosity to the whole bone. This particular geometry allows the apparition of secondary minor lever arm effects. At the top right corner (the fixed region), a larger region of compression stresses can be observed for the 135° and 90° cases. These regions are due to a mix between the boundary conditions effect (more specifically to the fixed support) and the lever arm effect. In case of 90° orientation, the two kind of compression regions, just described, are joined together to form a larger region of compression stresses.

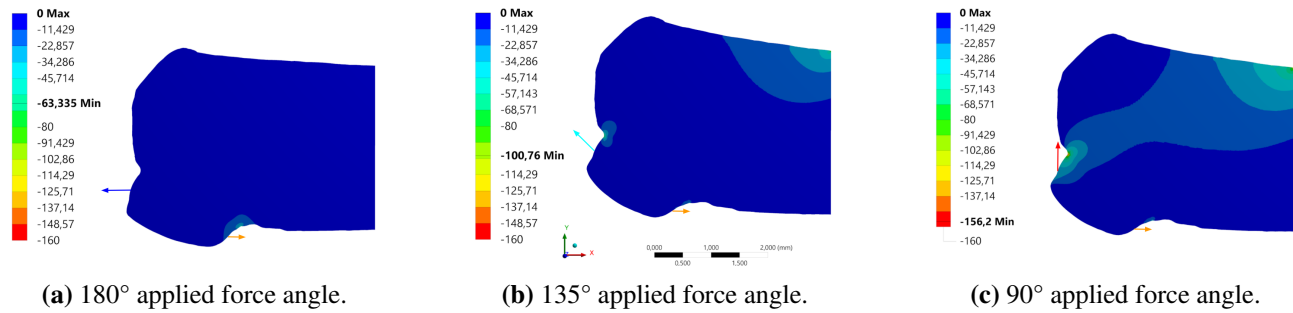


Figure 4.13: Contour plots of the minimum principal stress for a varying angle of the force applied at the Achilles tendon (constant force with a ratio of 0.6 at the plantar fascia).

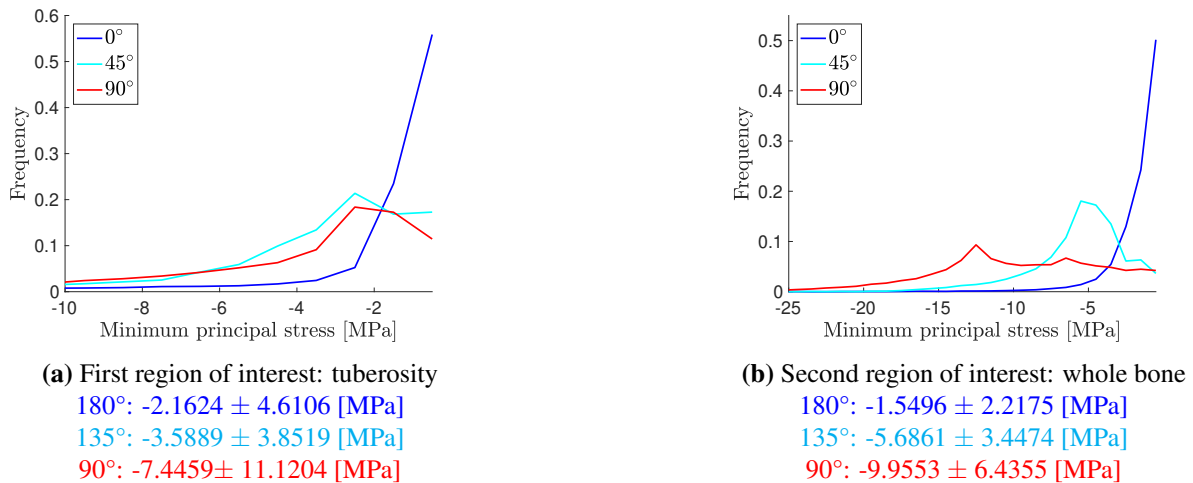


Figure 4.14: Comparison between the results for the minimum principal stresses obtained for both regions of interest.

The minimum principal stresses distributions are depicted in Figure 4.14. As expected, small compression stresses are present in the tuberosity (Figure 4.14a) for the 180° and 135° orientation cases. For the 90° orientation case, the mean stress values as well as the standard deviation values are higher due to the greater stress concentration close to transition between the left side of the tuberosity and the whole bone. For the whole bone region, the distribution of the minimum principal stresses are shown in Figure 4.14b. As observed in the contour plot, the highest mean stress and standard deviation values are observed for the 90° orientation case. The 135° case shows a relatively high mean value of minimum principal stress. It is due to the compression region close to the Achilles tendon.

3.2 Case II: intensity of the applied force at the plantar fascia

In this section, the impact of a force arising from the plantar fascia is assessed. The outputs results are shown for three different ratios between the forces at the two sides: 0 (no force at the plantar fascia side), 0.6 (value based on the ratio of their attachment area) and 1 (same force intensity on both sides).

Equivalent stress (Von-Mises)

Figure 4.15 shows the contour plots of the equivalent stresses (Von-Mises) for the three cases studied. Interestingly, a progressive stress isolation inside the tuberosity region is observed when the force intensity at the plantar fascia side is increased. Without any force from the plantar fascia (Figure 4.15a), the stresses are flowing through the entire bone. They are caused by the lever arm effect still present because of the 135° oriented force at the Achilles tendon. When a force is applied at the plantar fascia side (Figure 4.15b for the 0.6 ratio case), not only the lever arm effect is counterbalanced, therefore reducing the global stress flow, but it also seems that the remaining stress area is staying within the tuberosity (considering the other stressed regions as boundary). This effect is even more observable when the force applied on both sides are equal (Figure 4.15c). Again, stress concentrations at the top and bottom right side of the bone are present due to the boundary effects.

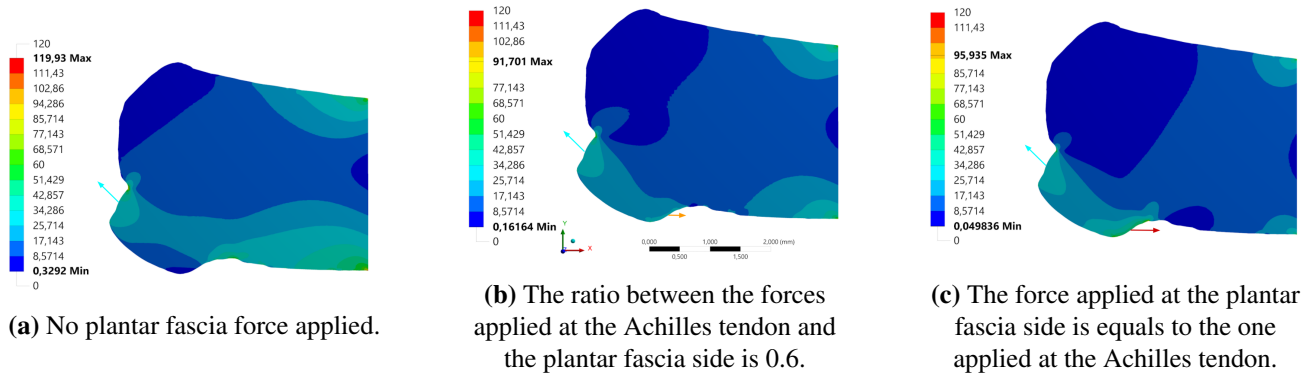


Figure 4.15: Equivalent stresses (Von Mises) for a varying intensity of the horizontal force applied at the plantar fascia side, based on its ratio with the force applied at the Achilles tendon which is kept constant in orientation (135° with respect to the x axis) and in intensity.

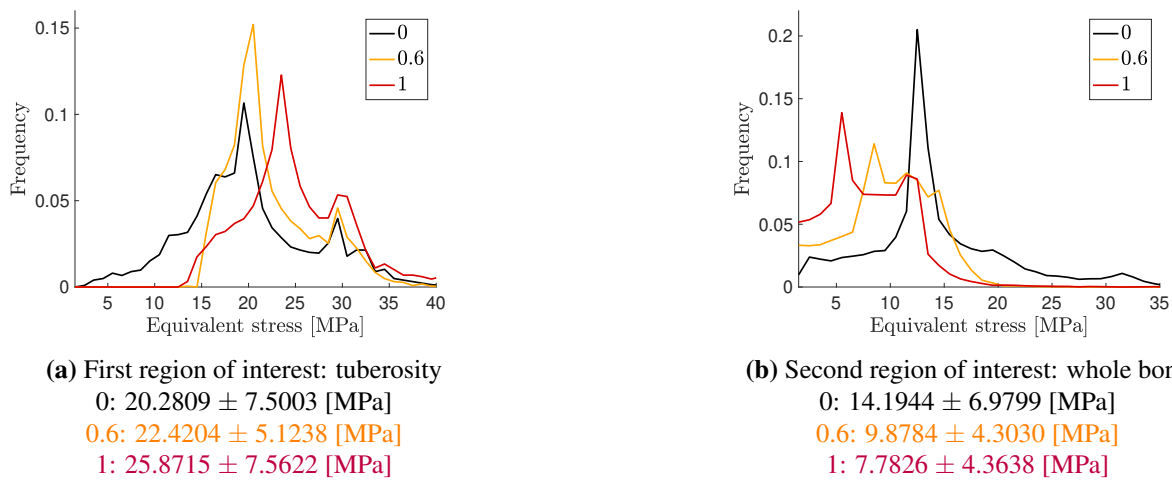


Figure 4.16: Comparison of the results for the equivalent stresses (Von Mises) obtained for both regions of interest.

This progressive stress concentration within the tuberosity is also illustrated by the equivalent stresses distribution plots in Figure 4.16. Indeed, for the tuberosity region (Figure 4.16a), the curves move towards higher stresses with an increasing force applied at the plantar fascia. This is translated by the increasing mean stress values. The opposite trend is depicted for the whole bone region (Figure 4.16b), the curves move towards lower stresses with

an increasing force at the plantar fascia side. Logically, the mean stress values are decreasing with this increasing force. Notice that the stress heterogeneity remains fairly similar when a force at the plantar fascia side is applied. A slight homogenization can also be spotted in the whole bone (decreased std), which further highlights the potential role of the tuberosity (as will be discussed later).

Maximum and minimum principal stresses

Figure 4.17 shows the contour plots of the maximal principal stresses, in other words of the regions dominated by tension, for the three cases. Similar observations than for the Von-Mises case can be drawn: the higher the force at the plantar fascia, the more concentrated within tuberosity the tensile stresses are.

This is again reflected in the distribution plots presented in Figure 4.18. Moreover, a clear homogenization is now reflected by the reduction in standard deviation for the whole bone region (-47.02 and -67.44 % for a ratio of 0.6 and 1, respectively). Interestingly, mean stress value within tuberosity is increasing of 27.97 %, whereas the whole bone mean value decreases of 62.36 %.

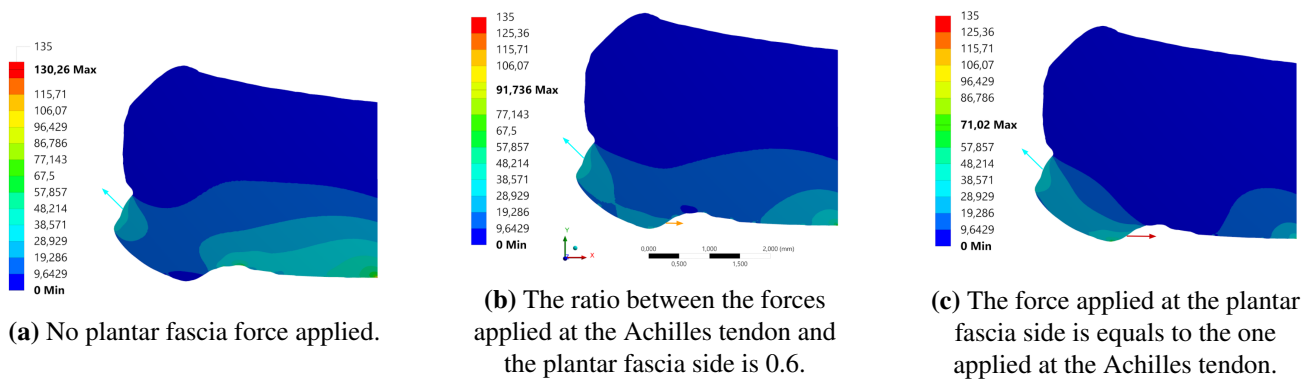


Figure 4.17: Maximum principal stress contour plot for a varying intensity of the horizontal force applied at the plantar fascia side, based on its ratio with the force applied at the Achilles tendon which is kept constant in orientation (135° with respect to the x axis) and in intensity.

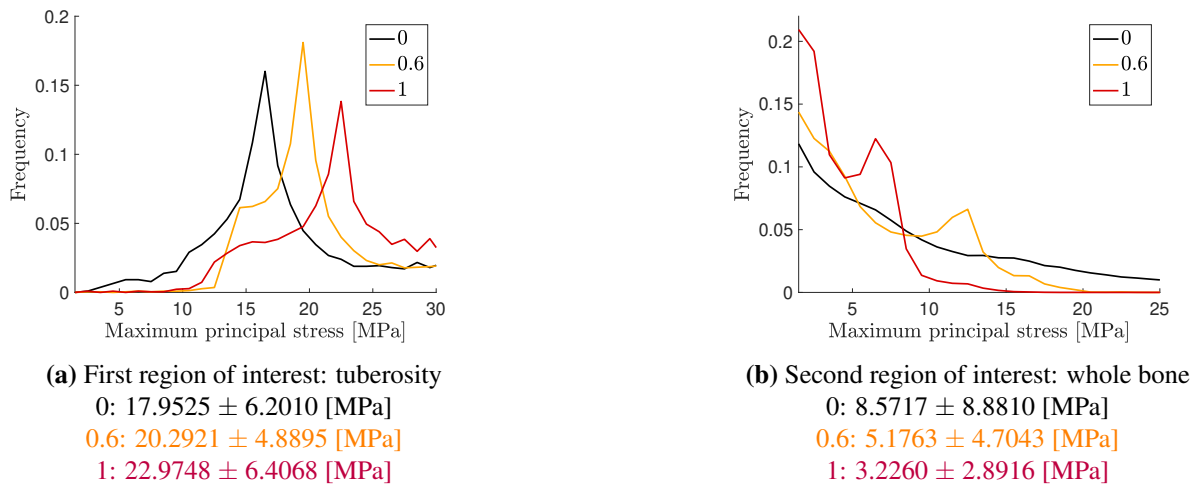


Figure 4.18: Comparison between the results for the maximum principal stresses obtained for both regions of interest.

Figure 4.19 shows the contour plots of the minimum principal stresses. In this case, the regions in compression are depicted. The usual boundary effect in the upper right corner is again visible. Small compression regions are also visible at the corners of the tuberosity where it connects to the whole bone. Interestingly, a high intensity of the PF force leads to a larger compressive concentration area than at the Achilles tendon, and that is spreading much more than for an intermediary ratio.

Figure 4.20 shows the minimum principal stresses distributions for both regions of interest. For the tuberosity region, the results are depicted in Figure 4.20a. Quantitative representation confirms those observations. Indeed,

while mean stress within the tuberosity is reduced with an intermediary plantar fascia force, an excessive one leads to higher stress (19.1% increase compared to the initial 0 force). For the whole bone (Figure 4.20b), a slight decrease is observed in the mean values, albeit the percentage gained with an intermediary force (-14.85%) is higher than when increasing further the force (-18.83%).

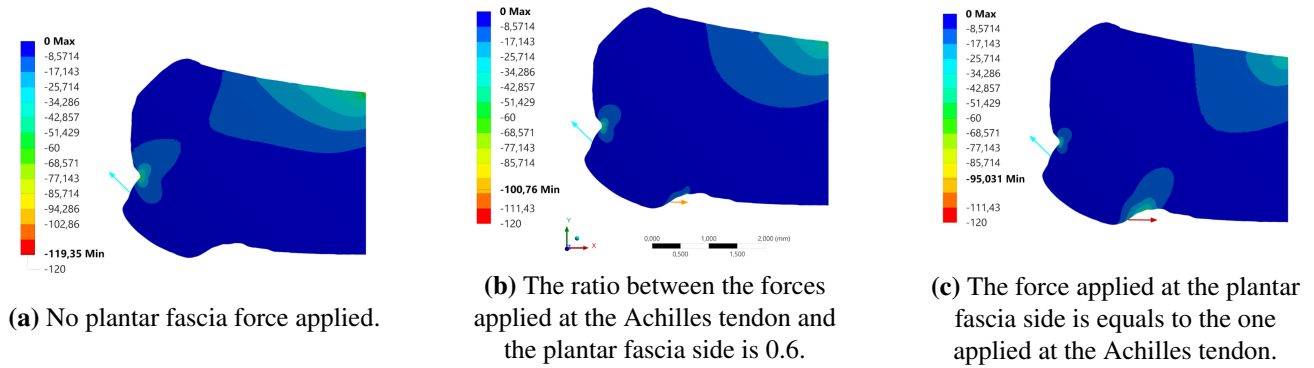


Figure 4.19: Minimum principal stresses for a varying intensity of the horizontal force applied at the plantar fascia side, based on its ratio with the force applied at the Achilles tendon which is kept constant in orientation (135° with respect to the x axis) and in intensity.

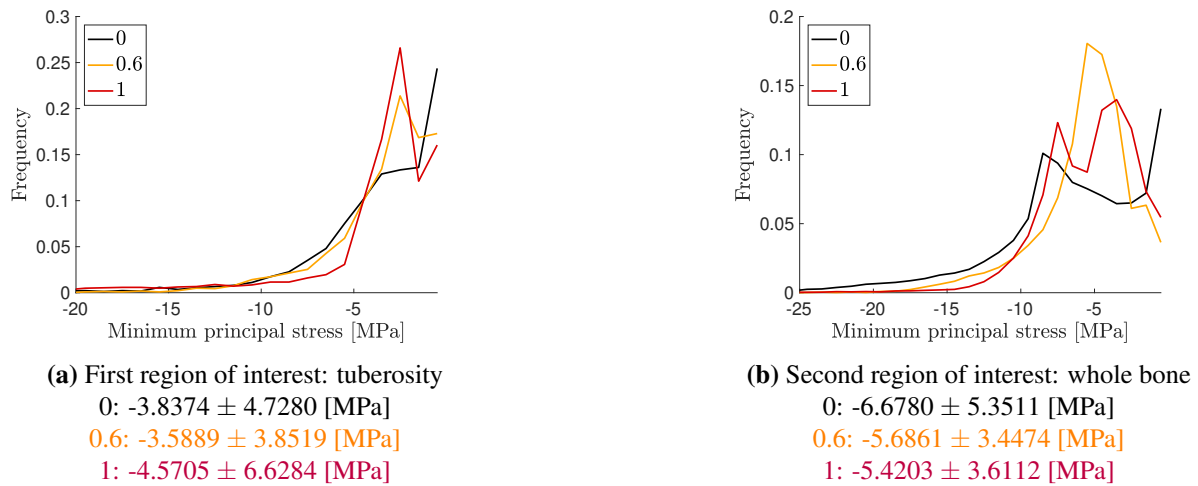


Figure 4.20: comparison between the results for the minimum principal stresses obtained for both regions of interest.

4 Discussion and conclusions

The aim of this section is to propose a critical discussion about the methods and results presented during this chapter.

Thanks to this chapter, a first glimpse about the Finite Element approach linked to our problematic was possible. The method was only based on one representative cross-section and the geometry was voluntarily simplified and transformed into a continuum model. While being clear limitations of this study, the idea was to simplify the process and the comprehension of these first simulations. The choice of working in two dimensions was considered for this and the following chapters because of the simplicity of handling the models as well as the reduced need in terms of time and computation power required. Two complementary sensitivity analyses were conducted.

For the Achilles tendon, the orientation of the force was studied. This was an interesting parameter to study, to understand the impact of the angle insertion of the actual Achilles tendon. Two extreme cases in addition to a more physiologically acceptable case were chosen. The 180° orientation was indeed something which is not compatible anatomically but the 90° orientation could happen in case of a very high level of traction on the Achilles tendon. In Chapter 1, in the clinical relevance section, the two last examples were the bone spurs apparition and the fracture avulsion case. These pathologies are linked to huge mechanical constraints. From the simulation results, it could be seen that indeed the stresses distribution was less heterogeneous in the case of 90° orientation and more specifically the tension stresses were more concentrated in the tuberosity. This could explain the avulsion fractures as well as the apparition of the bone spurs which could be induced to dissipate in some way this excess of energy. This stress concentration in the tuberosity could also be a protective mechanism which saves the whole bone from high stress. This is in line with the idea that bone shape is well adapted to receive the loading coming from the tendon.

In terms of values, the highest stress values were found in the tuberosity. They were mostly tensile stresses but they did not exceed 30 [MPa]. This remains acceptable compared to the ultimate stresses in tension for both longitudinal and transversal direction found for cortical bone as well as compared to the value of stresses applied as boundary conditions (up to 30 [MPa] on both Achilles tendons and plantar fascia).

For the plantar fascia side, the intensity of the force applied was studied. The original hypothesis about its intensity was based on a calculated ratio with the force at the Achilles tendon. The goal was to exploit the data from Chapter 3 which are specimen-specific. The "ideal" ratio calculated was 0.6.

The idea of considering this ratio seemed consistent regarding the result of our second case study. Considering no force at all at the plantar fascia gave the opportunity to the lever arm effect to fully spread inside the bone. This also created a high compressive stress region at the Achilles tendon insertion. Introducing a force at the plantar fascia induced a more balanced distribution of the stresses, in tension as well as in compression. Applying the same force intensities on both sides generated a high compressive stress area at the bottom inside corner of the tuberosity, while not reducing as much the stresses in the whole bone.

From these two sensitivity analyses, it seems that the most physiological parameters of the force boundary conditions are a 135° oriented force at the Achilles tendon and a 0.6 ratio of force applied at the plantar fascia side. Those values will be considered in our further simulations.

Chapter 5

Micro-architecture influence (micro-structural model)

1 Introduction

This chapter is the second one related to the investigation of the biomechanical behavior of the calcaneus. Complexity is progressively included in the previously presented model by considering bone porosity. The aim is to study the impact of structural changes on the stress and strain energy distributions. To do so, two image-based micro-structural finite element models are built, based either on low or high resolution images.

A first analysis is conducted based on the low resolution scans (5 μm voxel size), including trabecular porosity. The influence of several parameters (including bone length and force orientation) is studied.

The second one focuses on the influence of a gradual inclusion of porosity. In order to assess the impact of the fine microporosity present within the tuberosity, this analysis is conducted on high resolution scans (1.25 μm voxel size) available from Alexandra Tits (PhD student). Three models are being compared: one without any porosity (similar to the continuum model), one containing only the trabecular porosity (microporosity removed), and the last one comprising the full porosity.

As previously, the methods are presented and mainly include the geometry, meshing process, material properties definition. After that the results are presented and discussed.

2 Methods

This section describes step-by-step the procedure followed to build our new version of the model. In order to develop this image-based micro-structural model, another tool of Ansys is required and is called Ansys APDL. Indeed, we need a voxel based meshing that cannot be computed with the basic version of the software. Instead of an interface with limited possible modifications, Ansys APDL proposes a coding language (APDL) that ensures a total control over all the parameters of the finite element model. All the following steps described are indeed translated into this language including the geometry and the meshing process.

2.1 Geometry

The multiple geometries involved in the different studied cases are described in this section.

Case I: Low resolution micro-structural model

The geometries for this case are based on the same representative cross-section n°1313 coming from the low resolution (5 μm) μCT scan of sample T1. In contrast with the continuum model from the previous chapter, no simplification is included. In order to evaluate the influence of the bone length on the stress behavior, a cut geometry is considered as well. The idea is also to assess whether the considered length is long enough considering

the boundary effects of the fixation for the high resolution scan, which is cut at the exact same position. The geometries are presented on Figure 5.1.

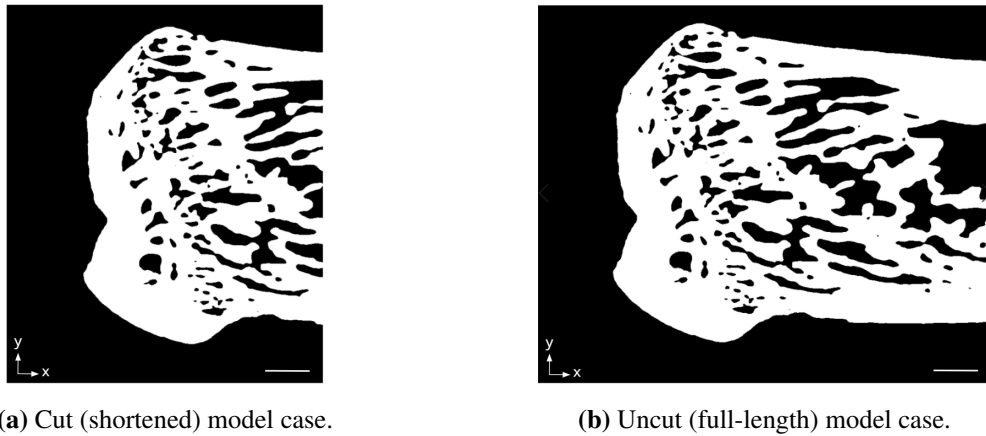


Figure 5.1: Geometries for the low resolution micro-structural model. Scale bar: 500 μm .

Case II: High resolution micro-structural model

For this second case, the influence of the porosity is investigated. The geometries are based on a high resolution (1.25 μm voxel size) cross-section of sample A1 (data coming from A.T.). Thanks to this resolution, more details about the micro-porosity are visible on the images.

For the analysis, three versions of the cross-section will be considered. The modifications of the cross-section are done using CTAn. These modified versions include: a continuum version (a) realized by removing all the porosity present, a version of cross-section including the trabecular network (b) but with its micro-porosity removed and a version without any modification (c). The geometries are presented in Figure 5.2.

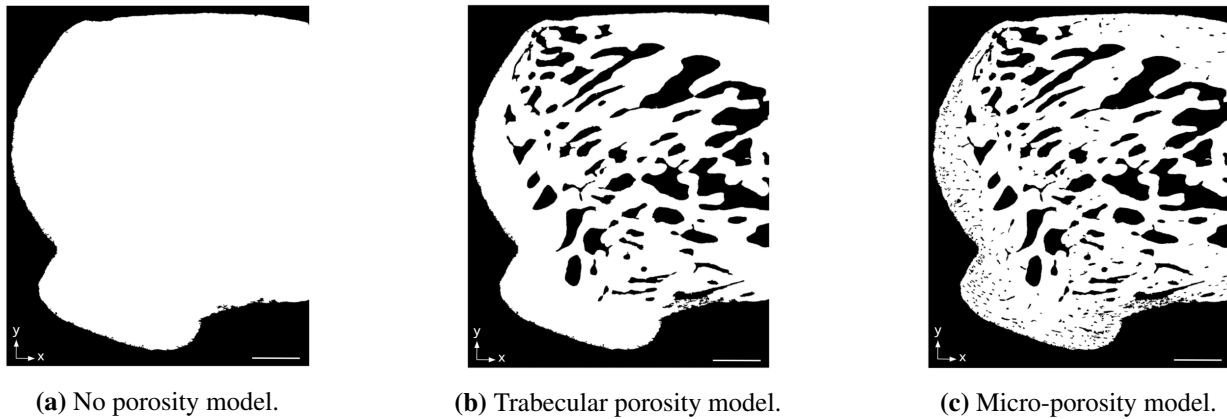


Figure 5.2: Geometries for the high resolution micro-structural model. Scale bar: 500 μm .

2.2 Regions of interest

In a same way than the previous chapter, two regions of interest are defined for each cases. The first one is the tuberosity region and the second one is the whole bone region. Again, an excluded region is also considered to avoid the boundary effects. Data from this region is not taken into consideration for the quantitative analysis (distribution plots). Similarly to Chapter 4, this excluded region is defined to start at the middle distance between the right side of the tuberosity and the end of the bone.

2.3 Meshing

The meshing step is the reason why Ansys ADPL is used for this chapter. Indeed, the porosity of the bone must now to be included and the meshing becomes therefore more delicate. To solve ensure a perfect replication of the finest porosity, a voxel-based meshing is coded.

The procedure is described in the following paragraph. The smallest unit of an image is the pixel. The idea is to transform each bone pixel to one element formed by four nodes. In order words, a Q4 element, quadrilateral element of the linear order. This is done by first converting the cross-section binarized image into a two dimensional matrix using the function `imread`. The pixels corresponding to bone are associated with a value of 1 and the void pixel are associated to a value of 0 in the created matrix. The element is build following the illustration in Figure 5.3.

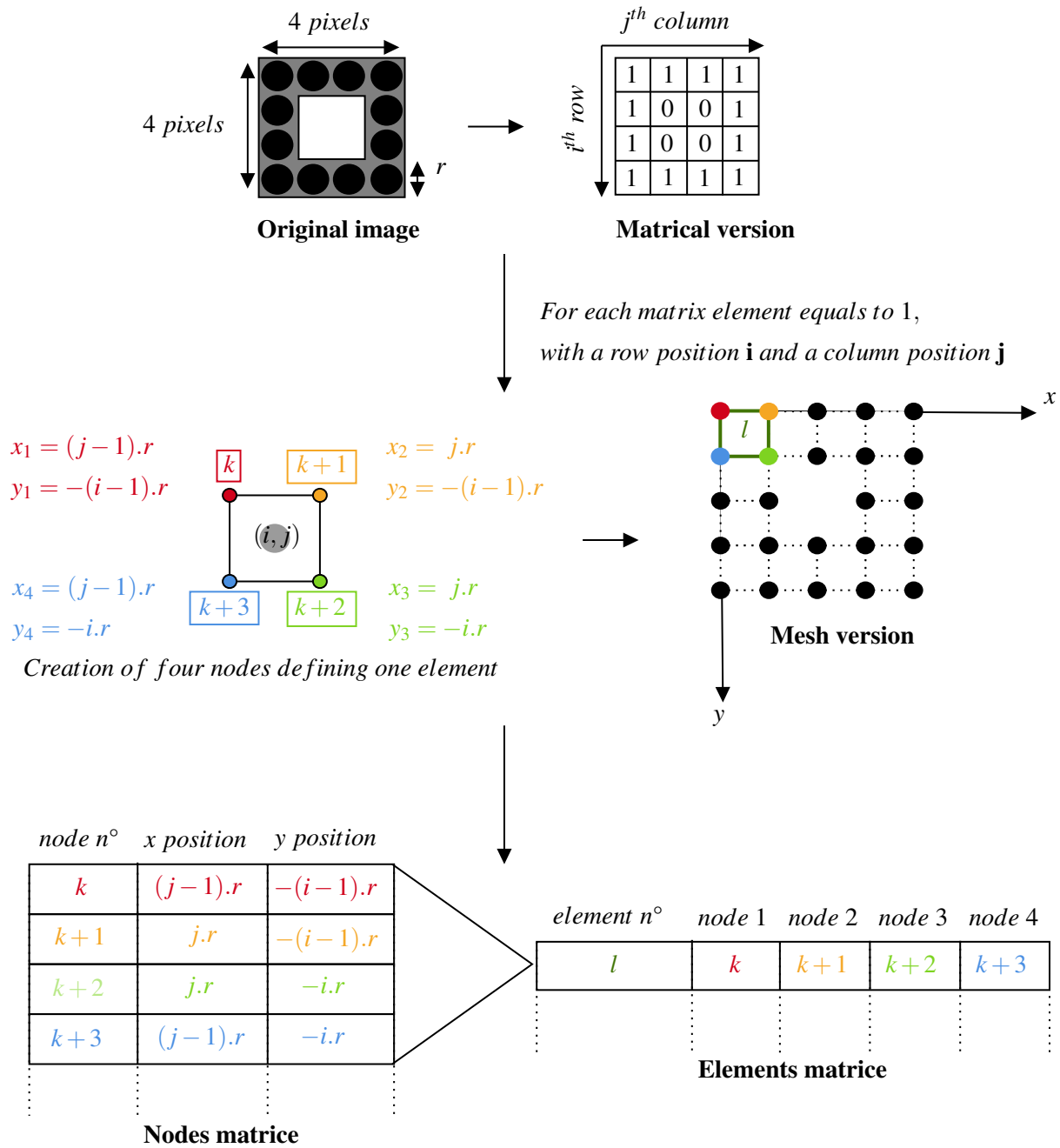


Figure 5.3: Mesh creation principle applied on a basic example. r is the resolution of the image or pixel size ($5 \mu\text{m}$ for low resolution model and $1.25 \mu\text{m}$ for high resolution model) (The filled circles on the original image represent the pixels).

Each entry of the matrix is characterized by its row i and its column j . For each entry, the coordinates of four nodes are created using the indices of it like described in Figure 5.3. The coordinates and the number of the nodes are stored in a second matrix. When four nodes corresponding to the an element edges are finally created, an element

number is created and stored in another matrix with the four nodes number involved. Of course, this process is applied only for pixels corresponding to bone.

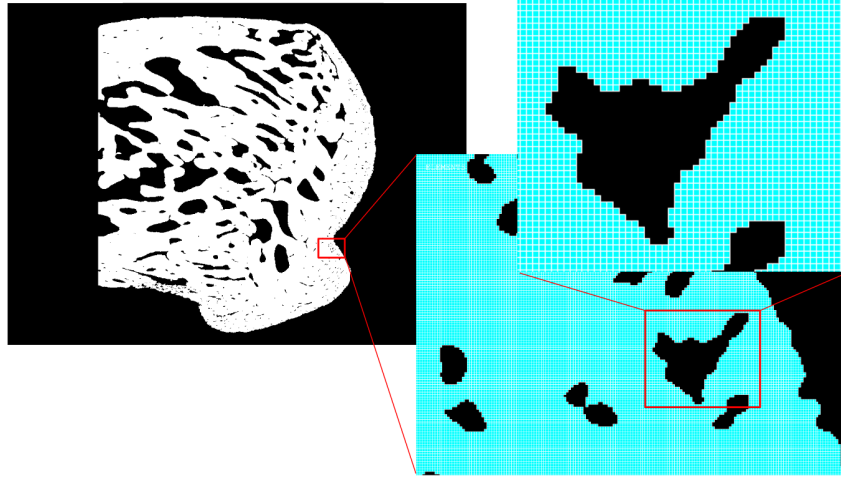


Figure 5.4: Final result seen in APDL ansys software for A1_hr. Progressive zoom of one particular zone of the tuberosity where micro-porosity is present. For the maximum zoom, elements are visible.

The two matrices are then written in a .txt file in the APDL syntax in order to make the creation of the model possible. The final result for a geometry based on A1_hr high resolution model is depicted in Figure 5.4. It highlights the perfect reproduction of the micro-porosity even at very low length scale.

Of course, the mesh is perfectly regular. The elements are the same: there are all perfect squares with a side length of $5 \mu\text{m}$ for a low resolution model or $1.25 \mu\text{m}$ for a high resolution model. In terms of quality assessment, it means that each element has an aspect ratio equal to 1 which is the best value possible for this factor.

2.4 Material properties definition

The bone is again assumed to behave as an isotropic and linear elastic material. The Poisson's ratio is also set to $\nu = 0.33$ [71]. For the definition of the Young's Modulus, a power law is used. This one is defined as follow:

$$\frac{E_{\text{continuum}}}{E_{\text{micro-structural}}} = \left(\frac{BV}{TV} \right)^2 \iff E_{\text{micro-structural}} = \frac{E_{\text{continuum}}}{\left(\frac{BV}{TV} \right)^2} \quad (5.1)$$

where $E_{\text{continuum}}$ is the Young's modulus for the continuum models, $E_{\text{microstructural}}$ is the Young's modulus for the micro-structural model and $\frac{BV}{TV}$ is the ratio of the bone volume over the tissue volume which characterize the density of the model.

$\frac{BV}{TV}$ being cross-section-dependent, the Young's modulus for the two models are not the same. For the low resolution model, the $\frac{BV}{TV}$ of the cut version of the cross-section is considered. It is equal to 40.28% therefore by the power law, $E_{\text{microstructural}}$ is equal to more or less 6 GPa. This Young's modulus is also considered for the full-length version of the model in order to only have one parameter varying at the time and thus ensure a relevant comparison. For the high resolution model, the density of the original high resolution cross-section without any modification is considered. Its $\frac{BV}{TV}$ value is equal to 0.5854 which gives, thanks to the power law, a $E_{\text{microstructural}}$ equals to more or less 3 GPa. Again this value of Young's modulus is also considered for the two other versions to avoid multiple factors of comparison.

2.5 Boundary conditions

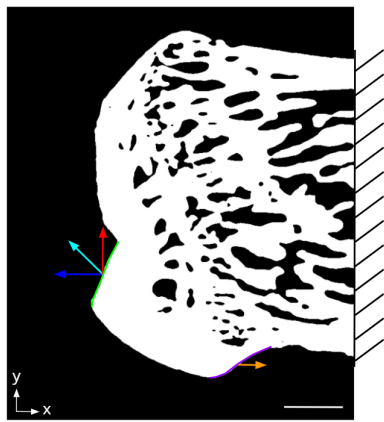
The definition of the boundary conditions is assessed in this section. For this chapter, two analyses are realized. Therefore, two sets of boundary conditions are required. Notice that, for both cases, the plane stress is again set. In order to avoid any singularity in the model arising from rigid body motion, fixation of the bone at some location is mandatory. As previously, it was chosen to imbed the lateral side of the bone for the same reasons.

Case I: Low resolution micro-structural model

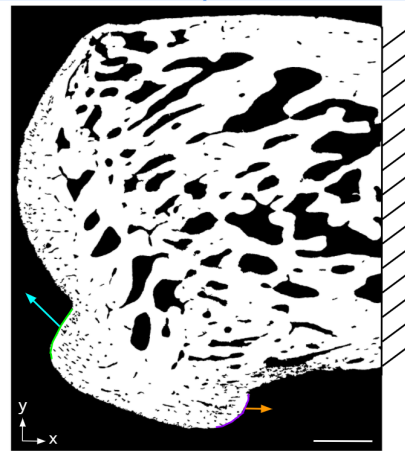
In addition to the investigation of the bone length effect on stress distribution, the impact of the force angle orientation at the Achilles tendon is also assessed. The idea is to ensure that our comparisons in terms of length is robust with the change of orientation. As a reminder, two forces are applied: a constant one, equivalent to a stress of 30 [MPa], at the Achilles tendon which is 180°, 135° and 90° oriented with respect to the x axis, opposed to a second constant one at the plantar fascia horizontally oriented, with a force corresponding to 60% of the intensity applied at the Achilles tendon side. Those three cases are illustrated in Figure 5.5a.

Case II: High resolution micro-structural model

For the high resolution case, only one configuration of these forces is considered and used for the three different versions of the model: a 135° oriented force at the Achilles tendon and a force at the plantar fascia, horizontally oriented with 60% less intensity. These boundary conditions are illustrated in Figure 5.5b.



(a) Case I: illustrated for the cut model case. The 180°, 135° and 90° cases of the force orientation at the Achilles tendon are illustrated as well as the horizontal force at the plantar fascia.



(b) Case II : illustrated for the original high resolution model. The 135° orientation force at the Achilles tendon as well as the horizontally oriented force at the plantar fascia are shown.

Figure 5.5: Boundary conditions shown for both models simulated in this chapter. Scale bar: 500 μm .

2.6 Solver features

As mentioned before, Ansys APDL software is used. The computer is the same than previous chapter. It is equipped Intel®core™i7-4790K CPU 4.00 [GHz] with 32 [GB] of RAM.

The number of nodes and elements created in each case are presented in Table 5.1.

		Number of nodes	Number of elements
Low resolution	Shortened model	253 896	246 241
	Full-length model	385 320	374 826
High resolution	Continuum version	5 860 180	5 851 434
	No micro-porosity version	4 635 012	4 598 138
	No modification version	4 559 048	4 506 795

Table 5.1: Number of nodes and elements created in each case.

Therefore, the CPU times for both cases are different, it is roughly 30 [s] on average for low resolutions models (over 6 simulations in total) and more or less 8 [min] on average for high resolution model (over 3 simulations in total). These CPU times do not take into account the time required for the software to read and compute the

mesh elements and to extract the results. This additional time required is much larger than the actual CPU times (around 30 [min]).

2.7 Outputs exportation

In this chapter, two outputs are considered: the equivalent stress (Von-Mises) and the strain energy.

3 Results

The aim of this section is to present the outputs results for both analyses conducted on the low and high resolution micro-structural models. Contour and distribution plots are commented for each simulation case.

3.1 Case I: Low resolution micro-structural model

Figures 5.6 shows the contour plots of the equivalent stress of the shortened and full-length models for respectively the 180° , 135° and 90° force orientation cases at the Achilles tendon. By looking at the stress distributions for the whole bone region, it seems that the stresses are simply flowing further away in the additional part of the full-length model. In the tuberosity region, global stress seems independent on the bone length. Only small differences for the extreme angles (180° and 90°) cases are observable.

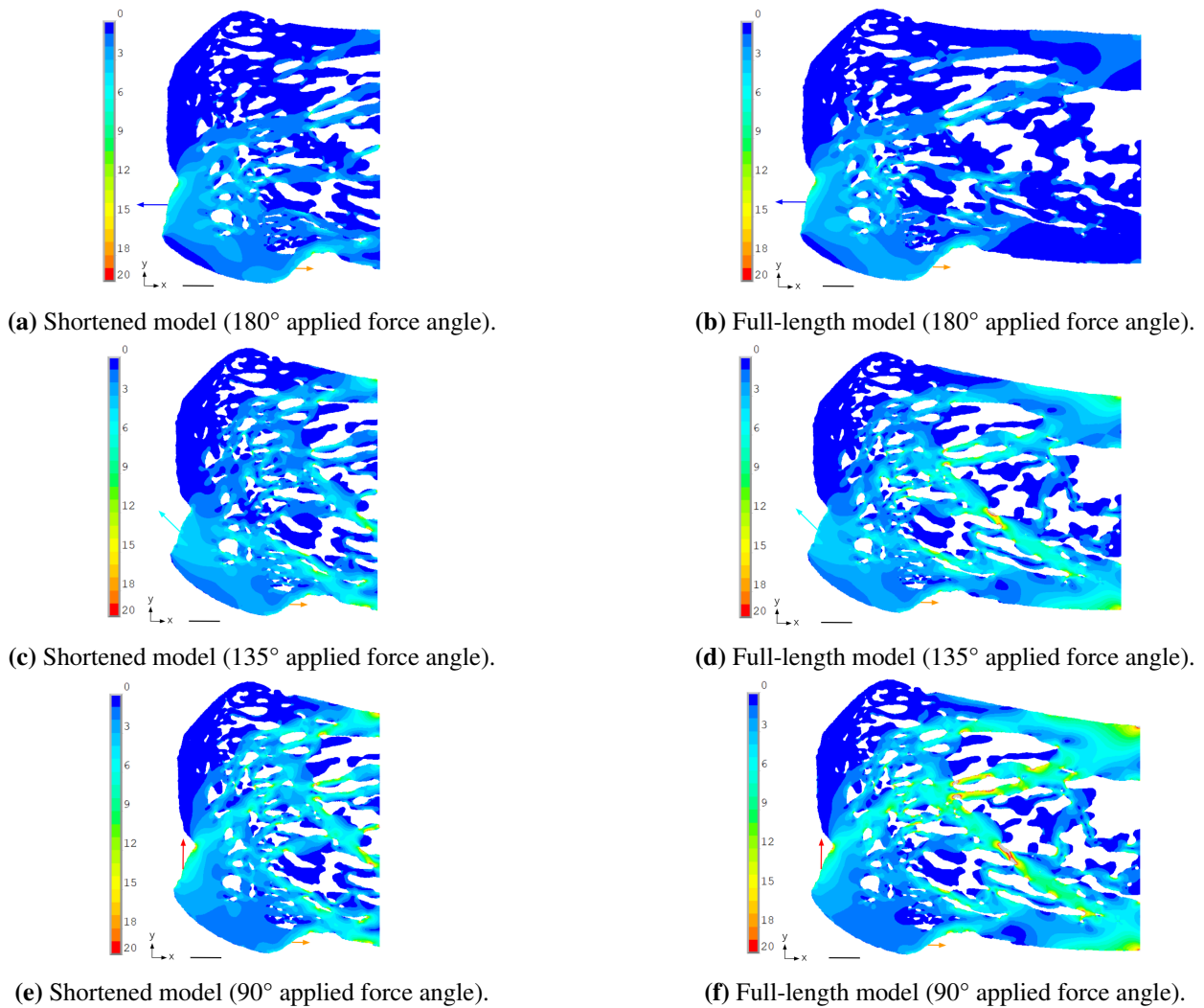


Figure 5.6: Comparison of the contour plots of the equivalent stress (Von Mises) [MPa] for the shortened and the full-length models for several orientations of the force applied at the Achilles tendon. (constant force with a ratio of 0.6 at the plantar fascia). Scale bar: 500 μm .

These observations are confirmed by the equivalent stresses distribution plots, in Figure 5.7. The comparison between the models is presented for the three orientations for the tuberosity region. For the sake of conciseness, whole bone region plots are discarded here. Our main interest is to access whether the tuberosity gets more or less stressed with the change of fixation position. Moreover, qualitative plots already show very few effect regarding the whole bone region.

At 180° (Figure 5.7a), curves of both cases are very similar in shape but the shortened model is slightly less stressed (7% decrease in mean value). At 135° (Figure 5.7b), bone length has almost no effect on the stress shape length: only 1.5 % decrease in value for the full-length case. Finally, for the vertical force (Figure 5.7c), an opposite trend compared to the horizontal one is observed: the tuberosity is slightly more stressed with a mean value 7% lower in the full-length case.

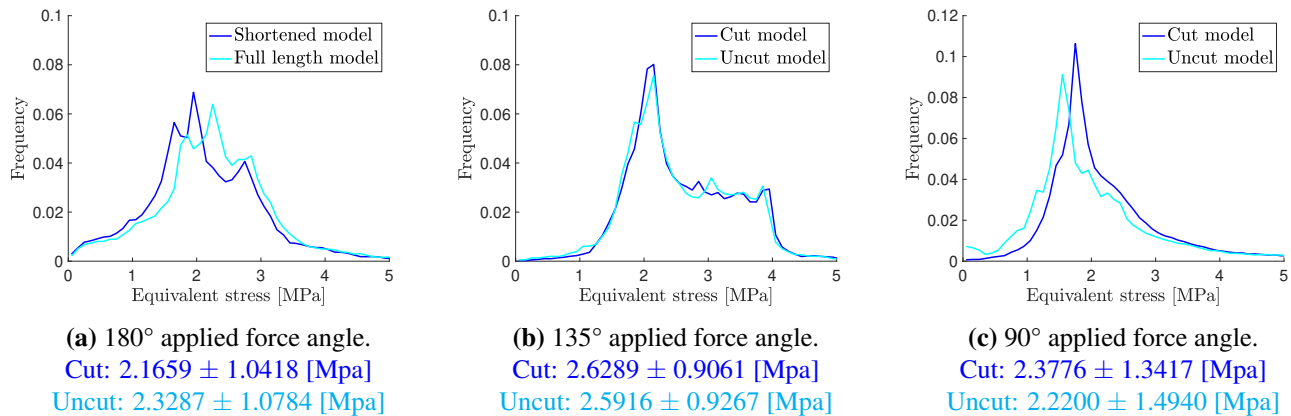


Figure 5.7: Comparison of the results for the equivalent stresses (Von-Mises) distribution obtained for three orientation cases in the tuberosity region. The means and standard deviations are also mentioned.

Figures 5.8 shows the contour plots of the strain energies of the shortened and full-length model for respectively the 180°, 135° and 90° force orientation cases at the Achilles tendon. By looking at the strain energy distributions for the whole bone region, the same distribution as for the equivalent stresses distributions is observed. They are prolonged through the trabeculae of the additional part of the full-length model case by comparison of the ones found in the shortened model version. The strain energy distributions in the tuberosity region are also not changing that much with the bone length. Again, only small differences for 180° and 90° cases are visible.

It makes sense, considering the fact that the strain energy of one element is its deformation energy stored under a loading condition. The strain energy is linked to the equivalent stresses and they evolve both in a same way.

These observations are again confirmed by looking at the strain energy distribution plots depicted in Figure 5.9. The comparison between the shortened and full-length model is presented for the three orientations in the tuberosity region. The curves show similar shapes and behaviors comparing case to case with the equivalent stresses distribution plots.

3.2 Case II: High resolution micro-structural model

Figure 5.10 reveals the resulting contour plots of the equivalent stress for a progressive inclusion of the bone porosity.

The geometry without any porosity (Figure 5.10a) corresponds to the continuum model simulated in Chapter 4. Results therefore show a similar behavior in terms of stress distribution, mainly influenced by the lever arm effect.

The continuum version (Figure 5.10a) shows a similar behavior in terms of stress distribution compared to the results from Chapter 4. The causes is again the lever arm effect.

When the porosity of the trabecular network is included in the whole bone region (Figure 5.10b), the stress distribution in this region is obviously hugely influenced. Some local stress concentrations are generated due to the shape and the interconnections of the trabecular network. However, the less stressed region on the top left area is preserved despite the inclusion of the porosity.

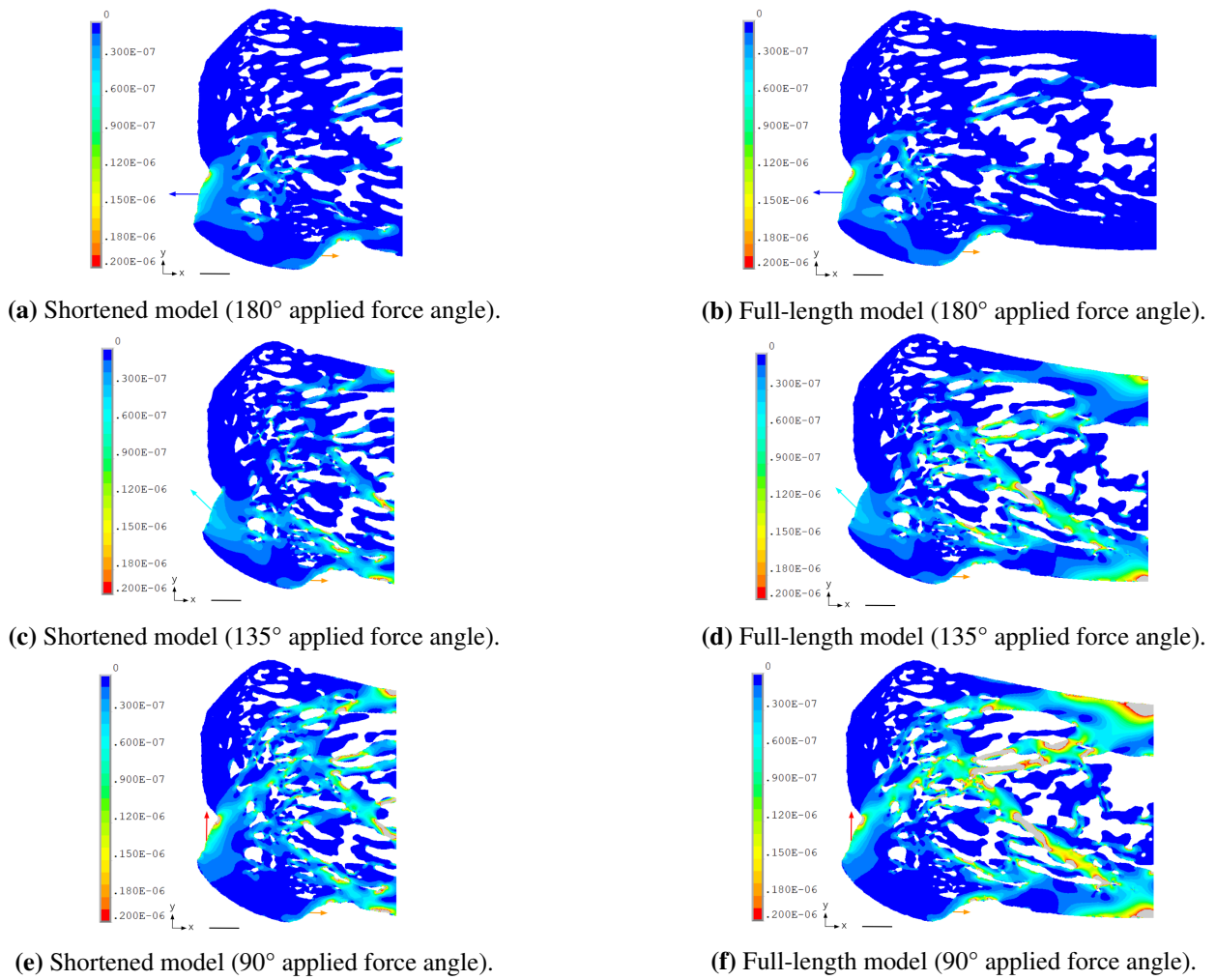


Figure 5.8: Comparison of the contour plots of the strain energy [mJ] for the shortened and the full-length models for several orientations of the force applied at the Achilles tendon. (constant force with a ratio of 0.6 at the plantar fascia). Scale bar: 500 μm .

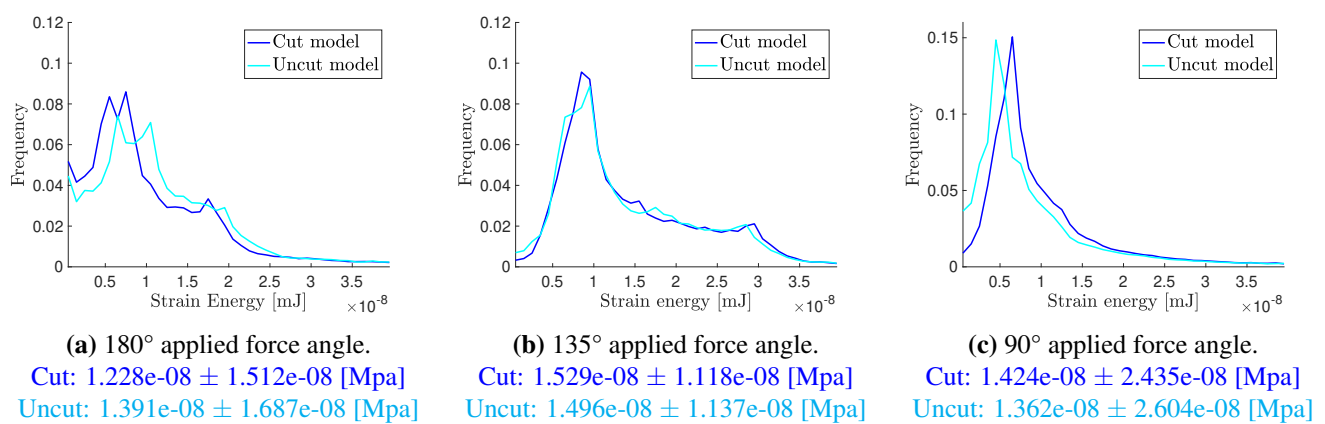


Figure 5.9: Comparison of the results for the strain energies distribution obtained for three orientation cases in the tuberosity region. The means and standard deviations are also mentioned.

Regarding the tuberosity region, the architectural modification influences the stress pattern. Indeed, although the insertion (side) regions remain almost unchanged, the pattern of the stresses from 6 to 15 [MPa], mainly located in the middle portion of the tuberosity, is modified. This could be due to the fact that this is the region where the trabecular pores are coming the closest to the tuberosity region. For the original version of the high resolution cross-section (Figure 5.10c), the micro-porosity is also considered. The latter being mostly present within the tuberosity, close to the force application area, this micro-structural change has more impact on that

region. Multiple stress concentrations are now visible around these micro-pores, especially around the Achilles tendon, which is one of the most stressed area. The stresses at the tuberosity region seem to continuously flow from one insertion towards the other.

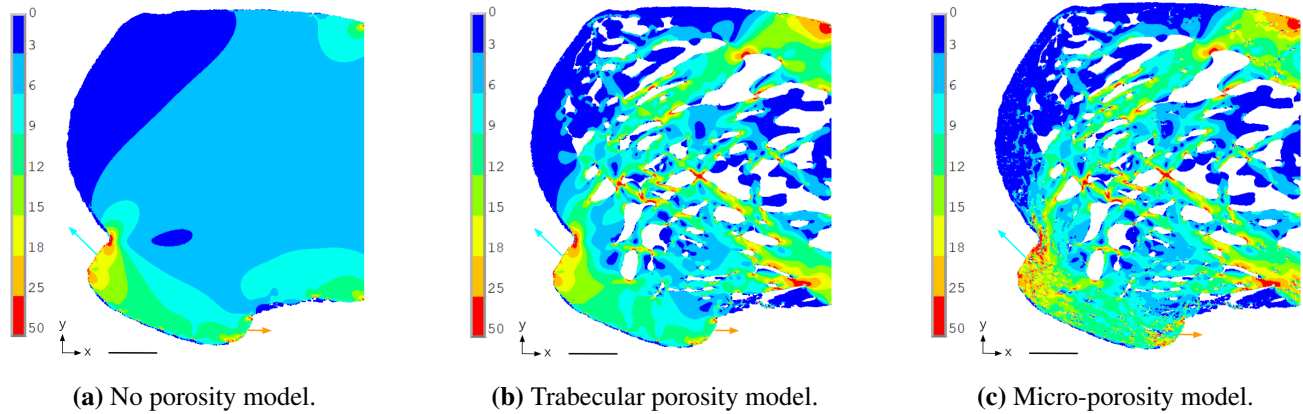


Figure 5.10: Comparison of the contour plots of the equivalent stress (Von Mises) [MPa] stress in three models for a 135° oriented force applied at the Achilles tendon (constant force with a ratio of 0.6 at the plantar fascia) Scale bar: $500 \mu\text{m}$.

Notice that including (either trabecular or micro-) porosity is similarly accentuating the effect of the fixation boundary condition on the upper right corner.

Figure 5.11 shows the equivalent stress distribution plots of the three porosity cases for both regions of interest. For the tuberosity region (Figure 5.11a), an increase of the mean stress value as well as of the standard deviation are induced by the introduction of the complete micro-architecture (respectively, compared to zero porosity: 11.5 % and 46.88 %). For the whole bone region (Figure 5.11b), the curve shapes are completely changing when the trabeculae network is introduced. The region is more stressed in terms of mean (61.02 % increase), and stress distribution is much more heterogeneous (213.19 % increase in standard deviation). Due to the reduced amount of micro-porosity presents in this region, its additional inclusion does not bring significant changes in terms of mean stress (less than 1 %) nor in the standard deviation (less than 5 % increase) .

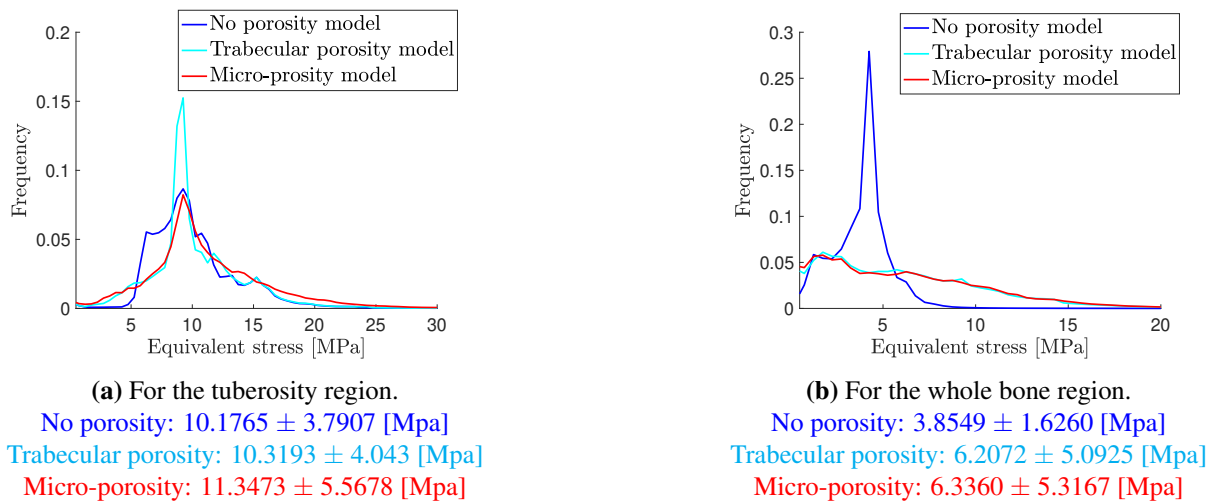


Figure 5.11: Comparison of the results for the equivalent stresses (Von-Mises) distribution obtained for both regions of interest. The means and standard deviations are also mentioned.

Figure 5.12 shows the contour plots of the strain energies for the three versions of the cross-section studied. The distributions of the strain energies values are again linked to what was observed for the contour plots of the equivalent stresses.

For the no-porous model case (Figure 5.12a), it can be seen that the main strain energies developed are located around the Achilles tendon. In comparison, the plantar fascia develops less strain energies, probably because of the reduced force intensity. For the Achilles tendon side, it seems that the strain energy smoothly decreases

in intensity towards the whole bone region in consecutive layers that tend to be parallel to the bone surface (i.e. connecting both insertion sites). Two additional zones of high strain energies are developed in the top and bottom right side of the bone due to the now usual boundary condition effect. The strain energies are evolving as a consequence of the inclusion of the trabecular network (Figure 5.12b). In the whole bone region, certain trabeculae, probably the ones participating the most to the lever arm effect, exhibit higher strain energies. For the tuberosity region, the strain energy flows similarly to stresses previously, are less organized and not smoothly connecting both insertion as in the non porous model. The trabecular network also accentuates the effect of the boundary conditions, with higher strain energies generated. Interestingly, it seems that the addition of the final micro-porosity is restoring the nice and smooth flow connecting both insertion sites (Figure 5.12c).

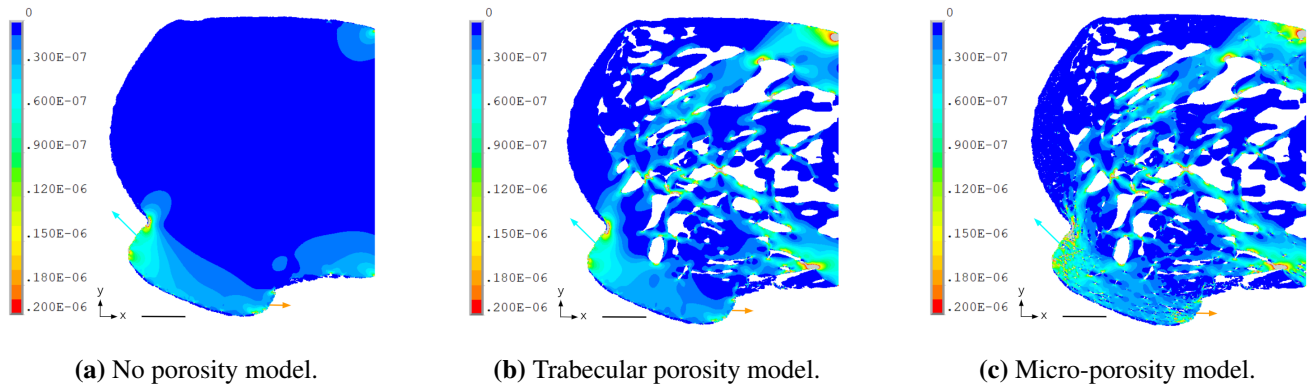
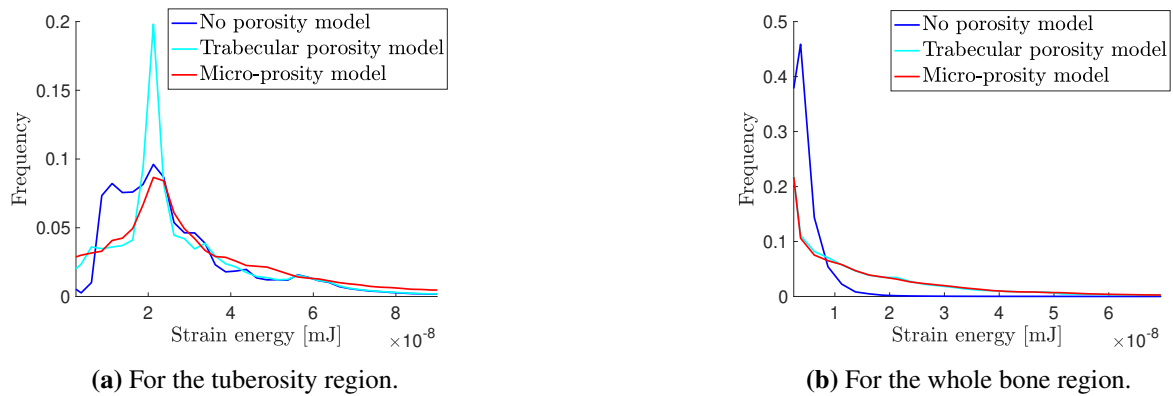


Figure 5.12: Comparison of the contour plots of the strain energy [mJ] stress in three models for a 135° oriented force applied at the Achilles tendon (constant force with a ratio of 0.6 at the plantar fascia) Scale bar: $500 \mu\text{m}$.

Figure 5.13 shows the strain energy distribution plots comparing the three case studies for the two regions of interest: tuberosity and rest of the bone. For the tuberosity region, the mean strain energy value as well as the standard deviation value increase with the complexity of the architecture (respectively, compared the zero porosity model, 4.33 % and 8.76 % for the trabecula network introduction or 35.64 % and 90.68 % for the micro-porosity addition). For the whole bone region, the trabecular network addition leads to a large increase of the strain energy mean value and a much more heterogeneous distribution.



(a) For the tuberosity region.
 No porosity: $2.9317\text{e-}08 \pm 3.1776\text{e-}08$ [Mpa]
 Trabecular porosity: $3.0588\text{e-}08 \pm 3.4561\text{e-}08$ [Mpa]
 Micro-prosity: $3.9766\text{e-}08 \pm 6.0591\text{e-}08$ [Mpa]

(b) For the whole bone region.
 No porosity: $4.2817\text{e-}09 \pm 5.5231\text{e-}09$ [Mpa]
 Trabecular porosity: $1.6262\text{e-}08 \pm 1.2809\text{e-}07$ [Mpa]
 Micro-prosity: $1.7272\text{e-}08 \pm 1.3780\text{e-}07$ [Mpa]

Figure 5.13: Comparison of the results for the strain energies distribution obtained for both regions of interest. The means and standard deviations are also mentioned.

4 Discussion and conclusions

The goal of this chapter was to investigate the impact of macro-structural and micro-structural features in a respectively low and high resolution model on several outputs including stress and strain behavior.

A first limitation may be raised regarding the material properties. Indeed, the same Young's modulus was considered for each model within a specific analysis to avoid introducing another variable parameter in the comparison. For the first analysis, it was an acceptable choice because the difference in volume fraction between the shortened and full-length model was not significant. For the second analysis, this choice was more questionable. Using the power law on the original cross-section, it gave a Young's modulus of 3 [GPa]. This value was also acceptable for the case where the micro-porosity was removed because the volume fraction did not change that much between the two cases. In contrary, using this Young's modulus value for the zero porosity version of the cross-section was a bit over-estimating its value. Indeed, the correct value (see Chapter 4, material properties definition) should be around 1 [GPa].

Our results interestingly suggest that the length considered of the bone along the cranio-caudal direction and therefore the proximity of the boundary effect is not influencing significantly the stress level within the tuberosity. This ensures us that the shortened bone required to achieve high resolution scan is not exaggeratedly over or under estimating the stress in our main region of interest.

For the second analysis, three versions of a high resolution model were compared. For both regions of interest, the model without any porosity showed the lowest values in terms of mean and standard deviation for the equivalent stress and the strain energy while the model containing all the porosity demonstrated their highest values. The differences are explained by the presence of micro-structural features and their role as stress concentrators. Moreover, the tuberosity got the greatest strain energy mean value and the strain energy was more homogeneously distributed than in the whole bone region. This is again a proof that, despite the addition of micro-architecture, the tuberosity acts as a protective structure for to the whole bone region.

The reproducibility of the results was not assessed because only one cross-section from one rat was considered for each case. Nevertheless, all the cross-sections with a tuberosity looked quite the same. Moreover, in [83], it has been proven that using more cross-sections does not change the main conclusions of an analysis.

Chapter 6

Material properties investigation (micro-structural model)

1 Introduction

This last chapter treats the investigation of how material properties changes may influence the biomechanical behavior of the calcaneus bone. This chapter is based on the results of the mineral content analysis conducted by Alexandra Tits (in collaboration with Dr. Markus Hartmann at the Ludwig Boltzmann Institute of Osteology of Vienna, Austria). The principle of this analysis is explained in a first section. As it has already been highlighted in the literature [31], calcium content at the insertion site is varying locally, inducing some gradients that in turn generate local variations in material stiffness. Our aim is to include those local changes in our micro-structural model by introducing stiffness gradients along the tendon Achilles side. Two kinds of spatial evolutions are computed: linear and hyperbolic.

For this chapter, two approaches are considered. A first one is based on a simplified, rectangular, bimaterial model and aims at getting a first glimpse of stress repartition when applying a linear material gradient while playing on the virtual tendon length. The second approach aims to implement these gradients in the high resolution micro-structural model. The results for these two approaches are presented and discussed.

2 Mineral content assessment

In the context of the PhD of Alexandra Tits, the evolution of mineral content across the interface was assessed using qBEI analysis. qBEI stands for quantitative Backscattered Electron Imaging, a scanning technique developed to investigate the mineral content inside bone samples notably.

The working principle is based on an electron beam that is sent to the sample. Some of the electrons are backscattered and reached the detector, hence forming an image [77].

This scanning technique allows to highlight especially the local variations of calcium concentration. Calcium content characterization is very useful since we know that the amount of mineral and its distribution play a major role to the mechanical properties of bone. The resulting qBEI images show different grey levels. They are linked to the local calcium concentrations found in the sample. High calcium concentration are linked to bright-gray level while low calcium concentrations are linked to dark-gray level [65].

Bone mineralization density distribution images were obtained following a well established procedure with a pixel resolution of $0.882\ \mu\text{m}$ [67]. Figure 6.1 represents the resulting qBEI image of the rat calcaneus exploited in this chapter with a focus on the enthesal fibrocartilage. Fibrocartilage is a connective tissue combining a white fibrous tissue (collagen type I) and a cartilaginous tissue (collagen type II). It gives respectively the toughness and the resilience properties to the tissue. The cells populating this tissue are fibrochondrocytes within the mineralized fibrocartilage [45] [85].

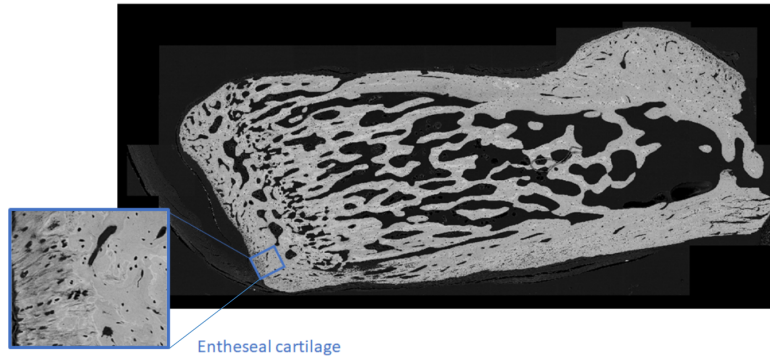


Figure 6.1: qBEI resulting image for the rat calcaneus (new sample) with a focus on the enthesal cartilage.

Grey level (GL) images are then converted to calcium concentrations using the following rule: $Ca_{wt.\%} = -4.332 + 0.1733GL$ based on calibration with phantoms of known mineral content. To get an idea of the mineralization profile, a rectangular mask was defined at the insertion site. Normal distance to the interface layer is computed and then all the pixels within the rectangular mask are grouped according to their distance. This allows to visualize the spatial evolution of mineralization. The obtained curve was then approximated by a hyperbolic fit (Figure 6.2 part A). Finally, this calcium content was converted into a Young's modulus using an exponential law: $E = \alpha \exp(\beta Ca)$ with $\alpha = 5$ [GPa] and $\beta = 0.05$ [1/Ca wt%] (Figure 6.2).

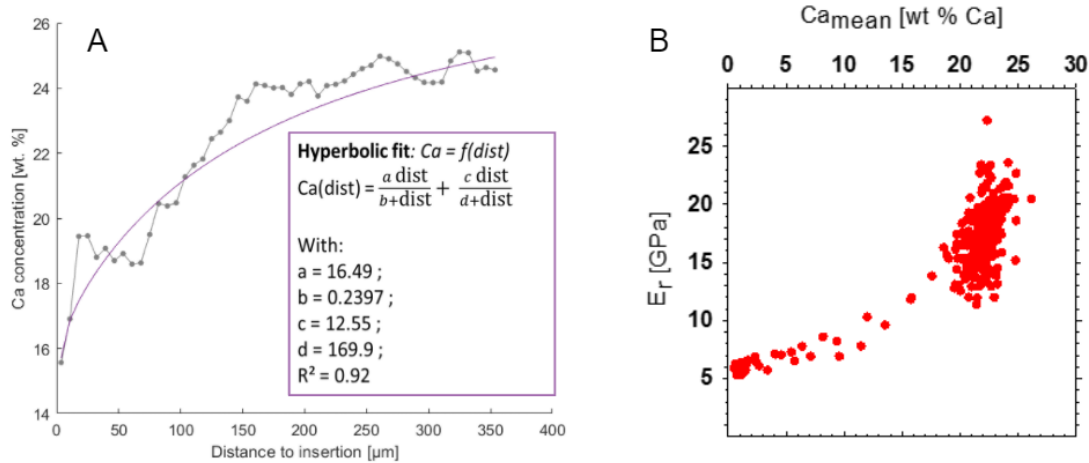


Figure 6.2: (A) Hyperbolic fitting of the calcium content as a function of the distance to the attachment side (B) Experimentally assessed variation of Young's modulus (E_r) with mean calcium content (Ca) showing a nice exponential relationship.

3 Methods

This section goes through the details of the methods related to our two approaches for material effect investigation. A highly simplified geometry is firstly investigated in order to have a full control over the parameters and to be able to draw clear conclusions from the simulations. Notably, a tendon region is now actually modeled, and the impact of its length is assessed. The idea is to evaluate which minimal length should be considered in our model in order to trigger bi-material effects. Then, the analysis is pursued within the complex and detailed geometry of the high resolution cross-section in order to evaluate the potential changes with respect to the simple model.

3.1 Geometry

The geometries involved in the two approaches are described in this section.

For the simplified model, four rectangles of varying sizes are considered. They are constant in height (1 [mm] width) but varying in length (specifically, 1.375, 1.37625, 1.3875 and 1.5 [mm]). This was computed in Matlab by fulfilling a two-dimensional matrix. The FE method developed in Chapter 5 can now be used on this geometry as well. The reason why several lengths are considered is explained in section 3.3.

For the second approach, the same high resolution cross-section than the one used in Chapter 5 is exploited ($A1_{hr}$) to create the geometry (Figure 6.3).



Figure 6.3: High resolution cross-section ($A1_{hr}$). Scale bar: 500 μm .

3.2 Meshing

The same meshing method developed in Chapter 5 was used for this chapter for both approaches. As a reminder, the goal of the method is to create a mesh composed of first order quadrilateral elements (Q4) (1.25 μm element size for both approaches) from the bone pixels of the cross-section image of interest. As usual, the BMP cross-section image is transformed into a two-dimensional matrix. The intermediate step is the creation of sets of four nodes, with their positions calculated based on the indices of the matrix element representing bone. Then these sets of four nodes are associated to the element. The interconnection of all these elements forms the mesh.

3.3 Material properties definition

The bone is, as for the other chapters, assumed to behave as an isotropic and linear elastic material. The Poisson's ratio is again set to $\nu = 0.33$ [71].

For the Young's modulus definition, two different gradients are defined. The first is the hyperbolic one. In order to compute over which distance the gradient will be applied, one parameter has to be fixed. It is chosen to impose the maximum Young's modulus to 15 [GPa], which is also used for the rest of the bone. Using the exponential law, it corresponds to a maximum calcium content equals to 21.9722 [wt%]. Using now the hyperbolic fitting equation defined in Section 2:

$$Ca(dist) = \frac{a \cdot dist}{b + dist} + \frac{c \cdot dist}{d + dist}$$

with $a = 16.49$, $b = 0.2397$, $c = 12.55$, $d = 169.9$, the corresponding distance equals 133.0574 μm . This value is therefore the maximum distance over which the gradient is applied.

The inverse reasoning is applied for the minimum Young's modulus. The minimum distance from Achilles tendon (where the force is applied) is assumed to be equal to 1.25 μm (i.e. one pixel).

The gradient is finally applied to all the elements that belong to this range of distance. This one is computed as its shortest distance to an element belonging to the "tendon zone". Indeed, the tendon and its reduced Young's modulus has to be introduced to potentially observe the benefits of the gradient. A layer of elements with a Young's modulus of 0.5 [GPa] is therefore defined to model the presence of the tendon.

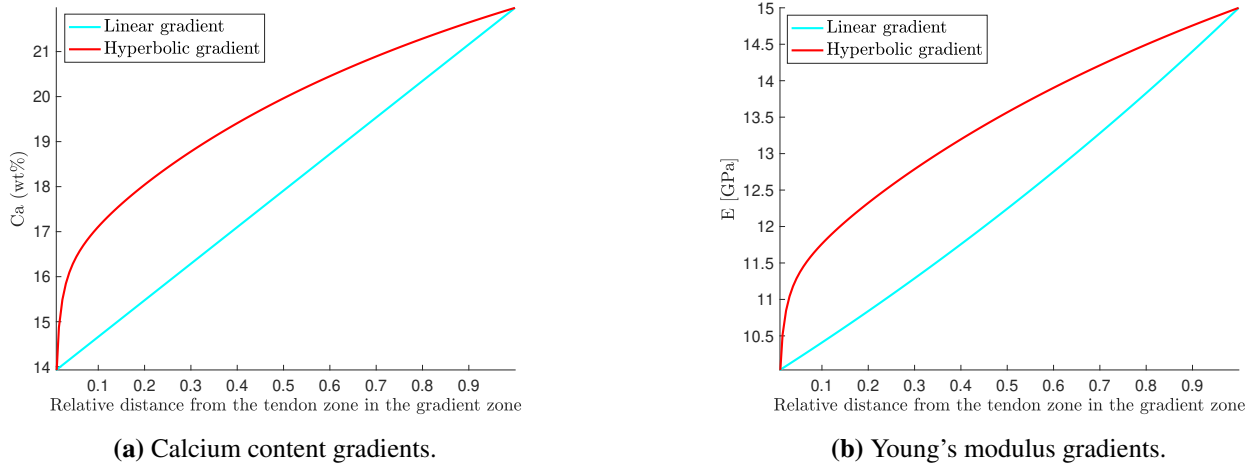


Figure 6.4: Calcium content and Young's modulus evolution in the two cases.

The linear gradient is directly obtained by computing the linear relation linking the two extremes of calcium content calculated for the hyperbolic gradient. The following linear equation is obtained:

$$Ca(dist) = a \cdot dist + b$$

with $a = 0.061$ and $b = 13.85$. Figure 6.4a shows the graph comparison of the two calcium content gradients. After using the exponential law, the Young's modulus as a function of the relative distance from the "tendon zone" (in the gradient zone) is plotted in the two cases in Figure 6.4b.

First, in the simplified approach, only the linear gradient is considered. The particularity of this analysis is the progressive inclusion of a so called "tendon zone" with four cases: 0, 1, 10 and 100 pixels in width at the right side of the rectangle model where the force is applied (section 3.4). As mentioned before, this zone is constituted of elements with an Young's modulus equals to 0.5 [GPa]. The bone side is kept constant in dimensions while the tendon part of a variable size comes to attach to it. Figure 6.5 shows an example for this additional zone constituted of 100 pixels in width.

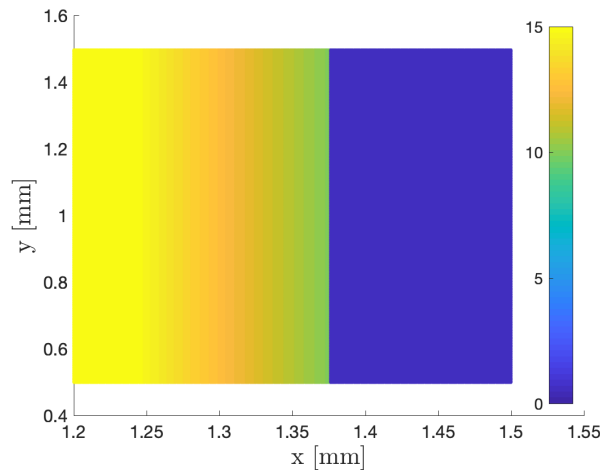


Figure 6.5: Linear stiffness gradient (zoom) for the simplified model. Example for the 100 pixels width zone of 0.5 [GPa] (125 μm). (Color bar : E [GPa])

For the second approach, on the actual bone cross-section, both gradients are tested. Instead of adding a variable size of tendon zone as for the first approach, only the elements that contain the nodes on which the force at the Achilles tendon is applied are considered to be a part of the tendon zone (i.e. one pixel layer at the bone surface). Figure 6.6 illustrates the resulting gradient at the insertion site. The contour where the tendon zone is located is shown in dark blue.

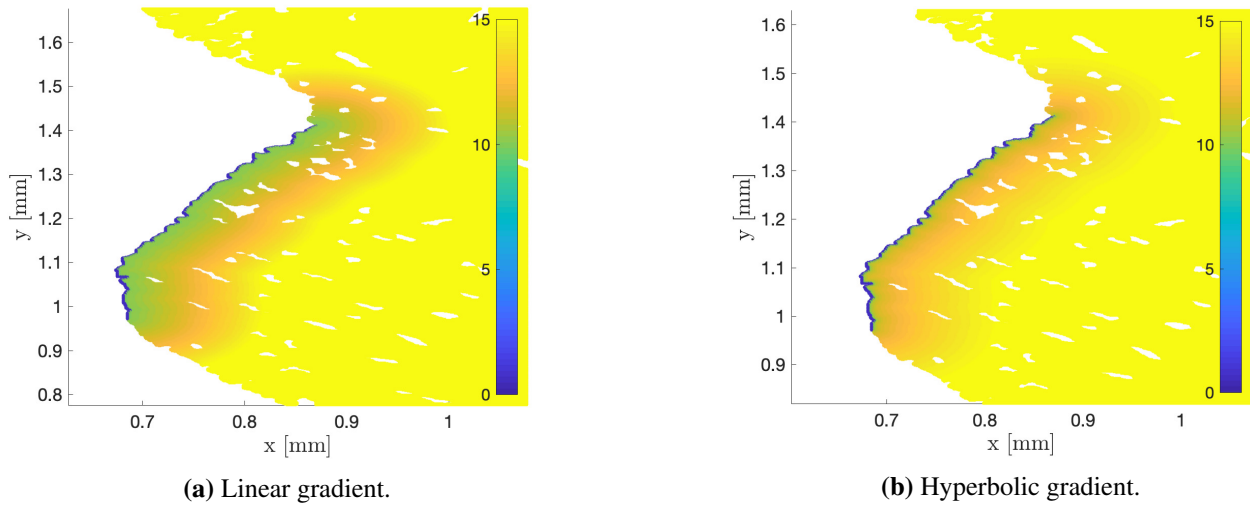


Figure 6.6: Illustration of the two kinds of stiffness gradient (Color bar : E [GPa]).

3.4 Boundary conditions

For this chapter, two approaches are considered. Therefore, two sets of boundary conditions are described. For both cases, the plane stress is again set. To avoid any singularity arising from rigid body motion, fixation of the bone at some location is mandatory in the model. It was chosen to embed the lateral side (left) for the simplified rectangular model, and (right) of the bone for the same reasons than previously explained. For the simplified model, only one node at the bottom left side was blocked in the two directions, the rest of left side nodes were only blocked in x direction.

For the simplified model, a force of 0.03 N is applied on every nodes of the right side of the rectangle, at the end of the tendon region. This is, as for the bone models, calculated to result in a stress of 30 [MPa]. For the second approach, a force with 135° orientation is applied at the Achilles tendon while a force with 0.6 ratio is applied at the plantar fascia. These boundary conditions are illustrated in Figure 6.7.

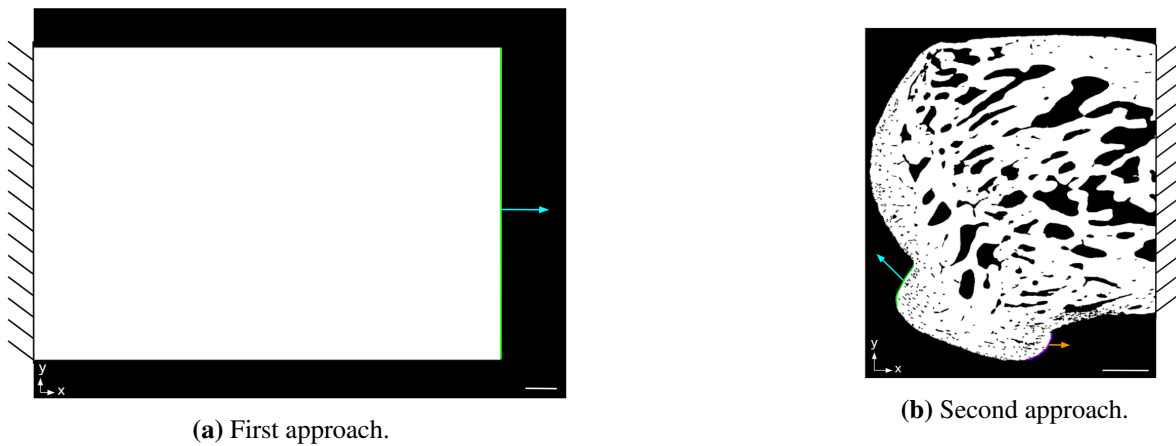


Figure 6.7: Illustration of the boundary conditions for the two approaches. Scale bar: (a) 100 μm (b) 500 μm .

3.5 Solver features

As mentioned before, Ansys APDL software is used. The computer used is the same than the previous chapters. Table 6.1 summarize the number of nodes and elements created for each case during the FE simulations. In terms of CPU times, for the simplified model, it equals in mean to 90 [s] and for the high resolution bone model, it is equal roughly to 9.5 [min].

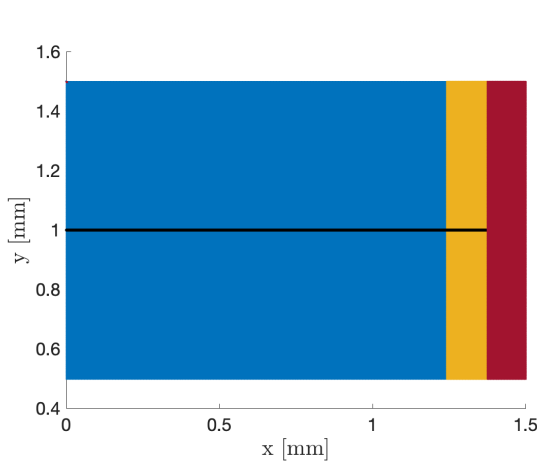
	Case	Number of nodes	Number of elements
Simplified model	0 px	881 100	879 200
	1 px	881 901	880 000
	10 px	889 110	887 200
	100 px	961 200	959 200
High resolution bone model	1 px	4 559 048	4 506 795

Table 6.1: Number of nodes and elements created for the different cases.

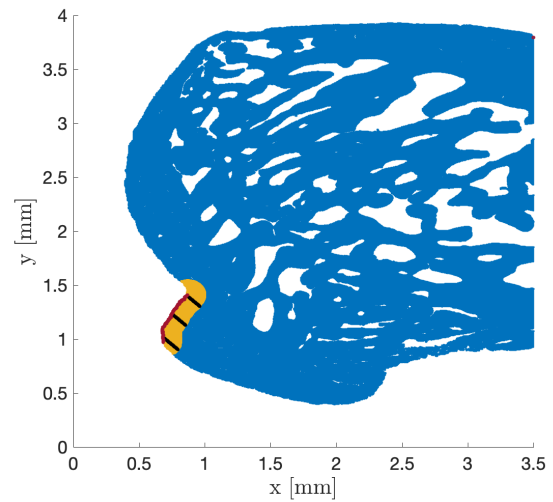
3.6 Outputs exportation

As previously, the contour plots are exported. Only one output is considered for this chapter : the equivalent stress (Von-Mises). Instead of considering two regions of interest and compute the stress distributions plots inside those regions, the choice was made to consider "lines" along which the stresses are exported because this way is more optimal to visualize the influence of the gradient inclusion.

Then the data are exported in `Matlab` to plot the stress data at all the positions along the lines. For the simplified model, only one line was considered. It is located along the x axis at the middle part with respect to y axis of the model in order to capture the stress values from the embedded side to the border with the tendon region. This line position was chosen due to the symmetry of the problem (Figure 6.8a). For the second approach, three lines were considered. These lines are now oriented 135° with respect to the x axis to get align with the force applied at the Achilles tendon. They start at the beginning of the gradient zone and they stop just before the tendon region in the tuberosity region. They are considered only inside the gradient zone in order to spot precisely the stress modifications in this region (Figure 6.8b).



(a) Stress line for the simplified model.



(b) Stress lines for the high resolution bone model.

Figure 6.8: Illustration of lines picked for both approaches. For both cases, bone, the gradient zone and tendon zone are respectively depicted in blue, orange and red.

4 Results

The aim of this section is to present the outputs results from both approaches. The contour plots as well as the stress values along the defined lines are shown in each case for the equivalent stress (Von-Mises).

4.1 Approach I: simplified model

Figure 6.9, 6.10, 6.11 and 6.12 show the contour plots for the equivalent stress (Von-Mises) for the four sizes of tendon region, respectively, 0, 1, 10 and 100 pixels in width. For each size, the comparison between no gradient and gradient is shown. Notice that the color bars used to illustrate the stress distributions are restrained from 23.5 [MPa] to 24.5 [MPa] because it is within this range that the major variations in distributions are observed.

For both cases, high stress concentrations are visible on the top and bottom edges of the right side of the model where the force is applied. These zones of high stresses are growing with an increased size of the tendon zone. They are probably created by an edge effect.

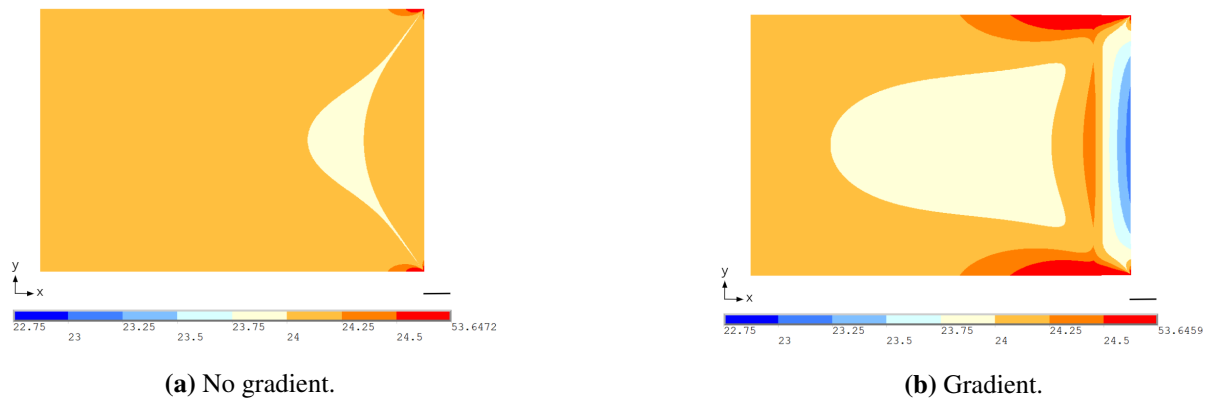


Figure 6.9: Comparison of the contour plots of the equivalent (Von-Mises) [MPa] stress in two models for no additional zone of $E=0.5$ [GPa]. Scale bar: $100 \mu\text{m}$.

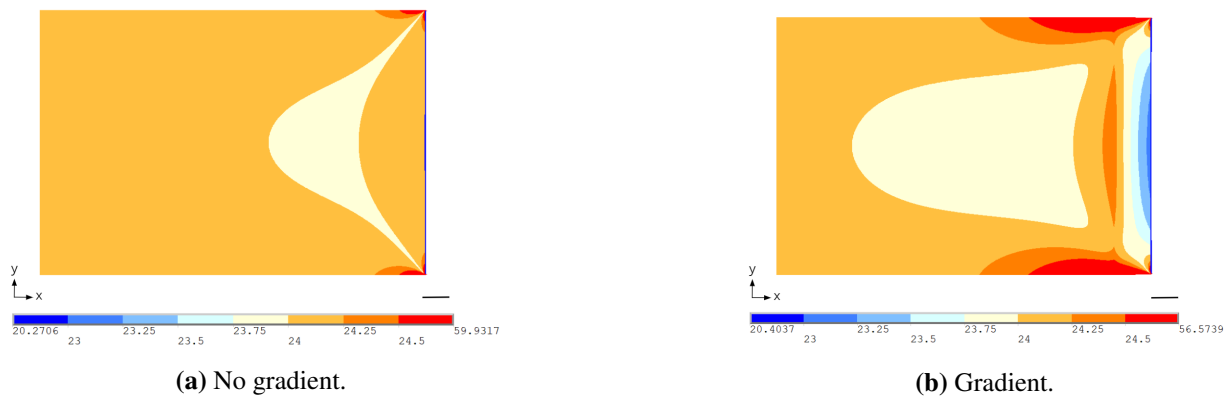


Figure 6.10: Comparison of the contour plots of the equivalent (Von-Mises) [MPa] stress in two models for an one pixel width additional zone of $E=0.5$ [GPa] ($1.25 \mu\text{m}$). Scale bar: $100 \mu\text{m}$.

Without gradient, nor tendon, the model behaves as an homogeneous material ($E=15$ GPa) on which a "small" force is applied. This force is not great enough to deform significantly the material. Therefore, stress concentrations are observed at the "free" corners where the force is applied because at these positions the material wants to deform by shrinking but because of its rigidity, it deforms only a little. Notice that a low stressed region is created under the influence of these two high stressed edges. By increasing the tendon side length, this effect is reinforced. Indeed, the tendon region having a Young's Modulus 30 times lower than the bone region, it deforms more easily but an increase of its size leads to an increase of stresses transmitted at the interface between the two materials. Its notably visible in Figure 6.11a and even more in Figure 6.12a. The stress concentration inside the

tendon region remains low at its central part but the edge effect is propagating inside it as well. (Figure 6.11a and 6.12a). For the longest case of tendon, the stress are not only high at the corners but all along the interface between the two materials.

With the inclusion of the gradient, the edge effect is even more accentuated for small tendon regions added compared to the cases without gradient. In the gradient zone, the stress concentrations are progressively increasing with respect to the distance from the tendon zone. It can be noticed that the more tendon is added, the less low stress distributions (depicted in blue) are present at the interface between the gradient and the tendon zone. At the end of the gradient, at the interface with the homogeneous $E = 15$ [GPa] region, a local concentration of stresses is visible. This local gradient is pushing further the edge effect along the sides. Interestingly, for the 100 pixels width tendon zone, the progressive stress concentration inside the gradient zone usually seen is transformed into a extended zone of a restrained lower stresses distribution.

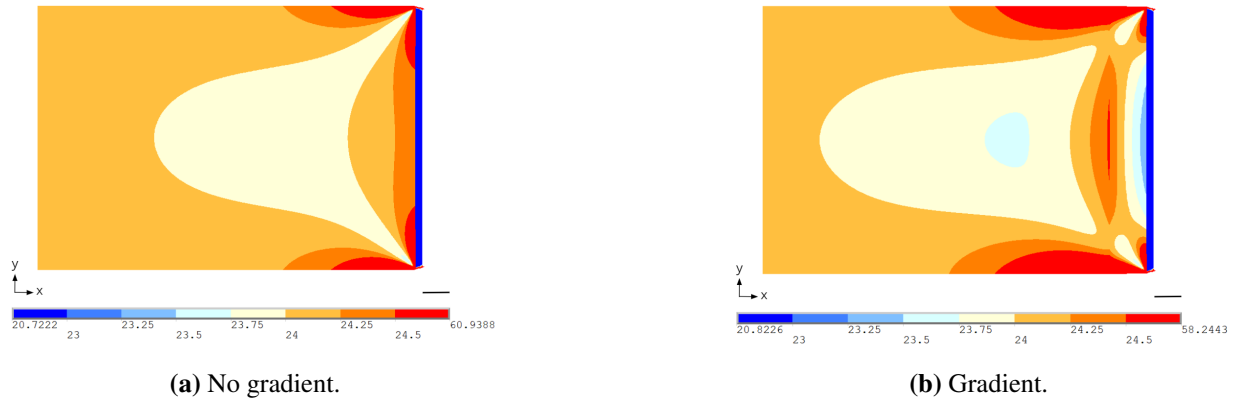


Figure 6.11: Comparison of the contour plots of the equivalent (Von-Mises) [MPa] stress in two models for a ten pixels width additional zone of $E=0.5$ [GPa] ($12.5 \mu\text{m}$). Scale bar: $100 \mu\text{m}$.

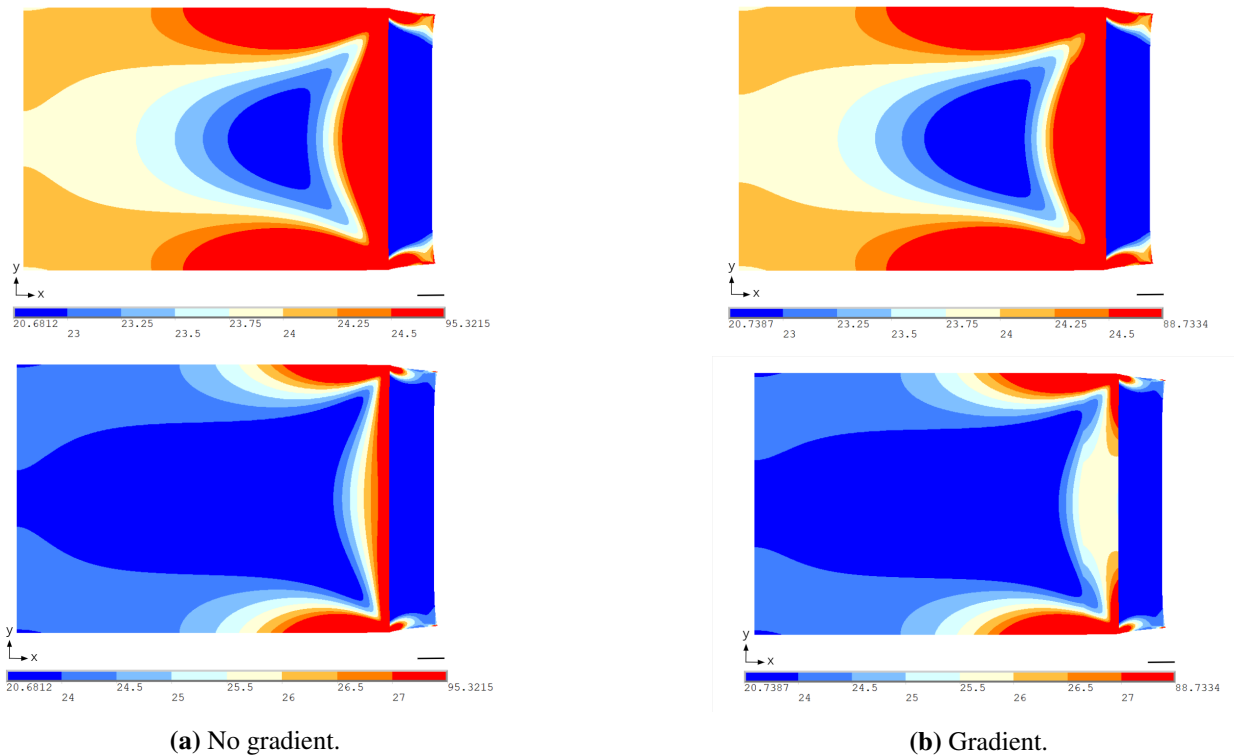


Figure 6.12: Comparison of the contour plots of the equivalent (Von-Mises) [MPa] stress in two models for a hundred pixels width additional zone of $E=0.5$ [GPa] ($125 \mu\text{m}$). (Two versions: one with the same color bar used for the previous comparisons (top) and a larger one to better see the high stress distributions (bottom)) Scale bar: $100 \mu\text{m}$.

Figure 6.13, shows the plots of the equivalent stress along the defined middle line. A comparison of the gradient and no gradient cases for the four sizes of tendon regions is depicted. Notice that stress values are divided by the

applied stress (30 [MPa]) in order to normalize them and plotted as a function of their relative distance along the line starting from the embedded side.

Without any gradient, Figure 6.13a, the 0, 1 and 10 pixels cases show uniform stress distribution along the line. In contrast, the 100 pixels width case shows a non-uniform distribution. The stresses are slightly decreasing in a first region (passage into the low stressed area) to finally increase to its maximum value.

The effect of the gradient (Figure 6.13b) is to allow a stress concentration reduction in the zone where it is included. For the 100 pixels case, a decrease of 7.69 % in comparison with the highest stress without gradient is observed. For the three other cases, a similar decrease of around 4% is observed.

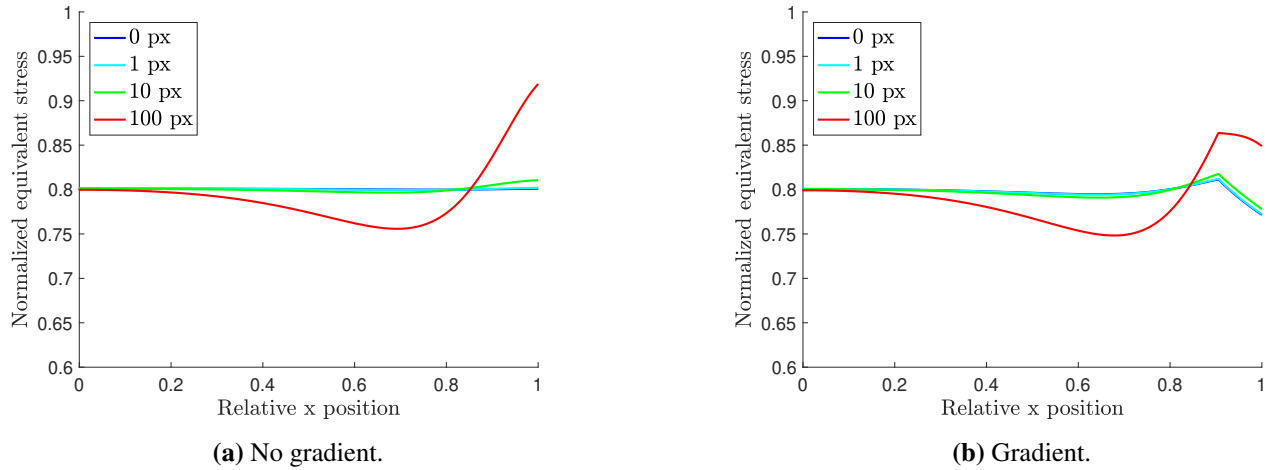


Figure 6.13: Comparison of the equivalent stress distributions (Von-Mises) along x at a constant y for the four sizes of additional zone of $E=0.5$ [GPa]. Scale bar: $100 \mu\text{m}$.

4.2 Approach II: high resolution micro-structural model

In Figure 6.14, the comparison of the contour plots for equivalent stress (Von-Mises) in the linear, hyperbolic and no gradient cases. At this stage, it is difficult to spot significant differences between the three situations. Interestingly, these differences are mainly observable within the stress concentration region at the corner of the Achilles tendon insertion.

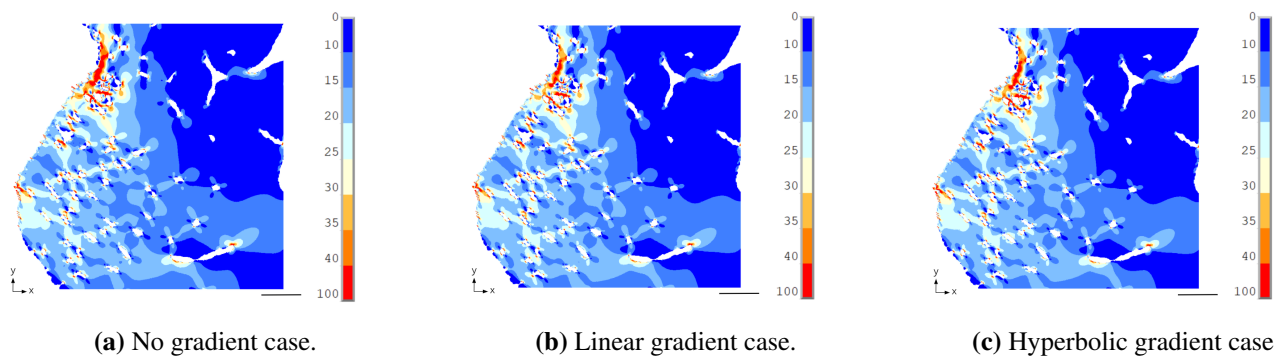


Figure 6.14: Comparison of the contour plots of the equivalent (Von-Mises) [MPa] stress for three different gradients. Scale bar: $100 \mu\text{m}$.

Figure 6.15 depicts the plots for the three profile lines of interest for the three gradient cases. As a reminder, Figure 6.16 illustrates the position of these lines in a global view zoomed at the tuberosity. Moreover, for each profile line case, a reduced view is shown at the bottom of Figure 6.15. The first line, Figure 6.15a passes in the neighborhood of a multitude of pores. As a consequence, a great variability of stress distribution is observed. Indeed, in Figure 6.14, local stress concentration around the micro-pores could be observed. Small differences are visible between the gradients. These differences are particularly visible in the left part of the curves, close to the beginning of the gradient zone, with an decrease of 17% in stress because of the addition of the two gradients. This effect is

also observed in the simplified approach. For the second line, Figure 6.15b, a huge peak is observable due to the same reason than explained for the first line (vicinity of a pore). In terms of difference between the gradient cases, only a small decrease at the Achilles tendon side with the gradients inclusion is seen. Finally, for the third line, Figure 6.15c, because it does not get close to any micro-porosity, the curve is smoother. A decrease in stress of roughly 30% along it is observed. This is in contradiction with what is observed in the first approach. Indeed, in the simplified model, the stress increased with the distance inside the gradient zone. It could be explained by the corner effect. Indeed, the profile line starts at the corner of the tuberosity, where a higher stress concentration is depicted. (Figure 6.14)

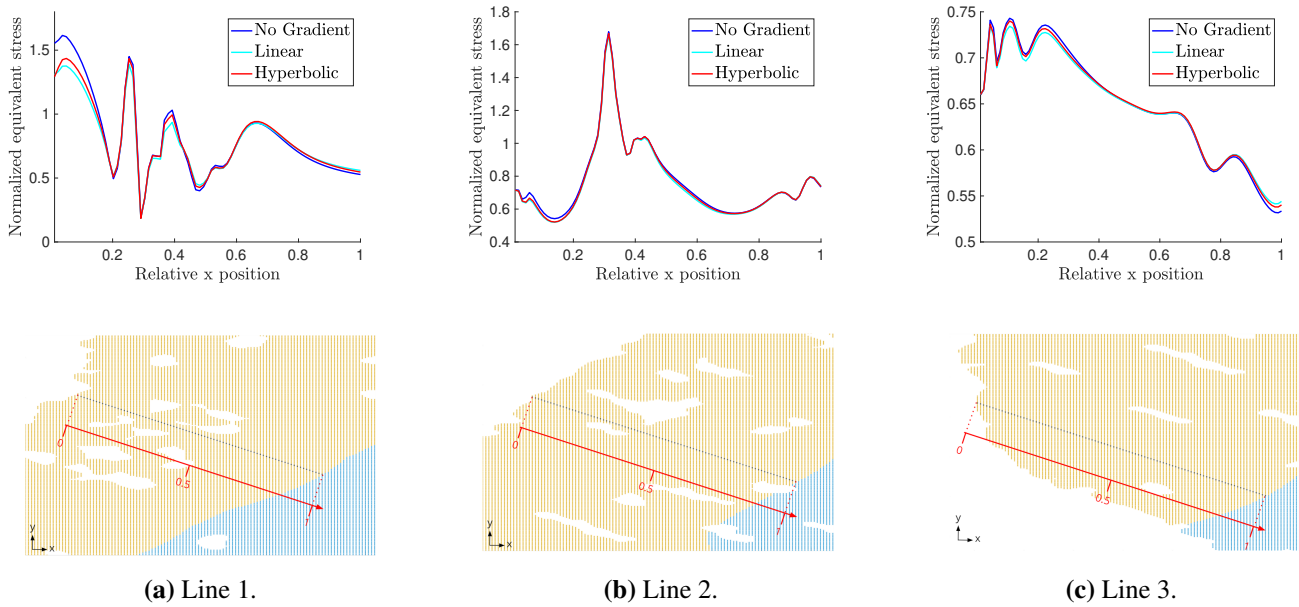


Figure 6.15: Top: comparison of the results for the equivalent stresses distribution (Von-Mises) along three different lines for the three cases. Bottom: visualization of each line.

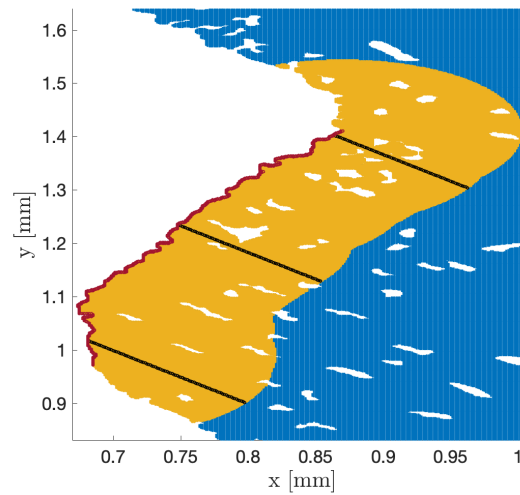


Figure 6.16: Global view of the three lines. The bone, the gradient zone and the tendon zone are respectively depicted in blue, orange and red.

5 Discussion and conclusions

The goal of this chapter was to investigate the influence of material properties on the equivalent stress results (Von-Mises) in a simplified geometry as well as within the real cross-section.

The first approach was voluntary based on an extremely simplified geometry in order to provide a first insight of the impact of a linear gradient introduction. The presence of the edge effect was observed in each case. A smoother stress distribution was induced at the gradient zone with a progressive equivalent stress increase from the side where the force was applied towards the end of it instead of the homogeneous distribution (except at the right corners) without it. A local increase of stress concentration was also observed at the interface between the end of the gradient zone and the rest of the model.

For the second approach, the high resolution model of the bone was considered. The introduction of the gradients inside this model has not revealed significant effects. This could be explained by the proportion of the gradient zone in comparison of the whole model (Figure 6.8b). The whole bone region being very rigid ($E = 15$ [GPa]), and the gradient being distributed on 5 [GPa] over a small area, its impact is limited compared to the simplified model. Moreover, the presence of pores are increasing stresses around them whereas they seem aligned (Figure 6.14). This could be useful for another purpose.

Conclusion and perspectives

The main goal of this master thesis was to better understand the bone side of the tendon-to-bone attachment, especially the Achilles tendon and plantar fascia attachments. A complete methodology starting from the rat sample extraction and scanning, through the quantification of the attachment surfaces of the Achilles tendon and plantar fascia, to finally finish on the investigation of the bio-mechanical behavior of the calcaneus bone using the finite element method. Our objective was to study the stress distribution in calcaneus bone and more specifically to highlight the crucial role of its geometry in the stress distribution.

Firstly, the assessment of the staining process on the samples before scanning was investigated. It allowed to confirm what could already be observed without it. Considering the noise that it created by staining all the present tissues, and even those unwanted, the μ CT images without staining were privileged.

Secondly, a process was developed to compute the attachment surfaces of both the Achilles tendon and the plantar fascia using the μ CT images. The resulting area values showed a small standard deviation, proving the efficiency of the method despite the high shape variability between the samples. Additionally, the visualization of these attachment surfaces directly on the bone was computed, highlighting the fact that the tuberosity facilitates the attachment of the two soft tissues of interest.

Third, the finite element method was used for several purposes, using two-dimensional models of the calcaneus bone:

- A first finite element analysis was done, considering a simplified continuum model. The combined results of this analysis led to the conclusion that the best force boundary conditions were a force oriented with 135° with respect to the horizontal axis applied at the Achilles tendon and a force with a ratio of 0.6 in intensity applied at the plantar fascia. This "realistic" applied forces configuration allows the stresses to concentrate in the tuberosity and therefore to relieve the whole bone region.
- A second one was based on micro-structural models. From the study of the macro-structural changes influence (performed at low resolution), we concluded that the length considered for the bone along the cranio-caudal direction had not significant impact on the results found in the tuberosity region. For the second analysis, at high resolution, the micro-structural changes influence was assessed. The conclusion was that despite the increased stresses induced by the micro-architecture presence, the tuberosity remains the region where the stresses are predominantly concentrated, acting as a protective structure for the whole bone. The bone being a multi-functional material, the increased stress could be useful for another purpose.
- Finally, a third finite element analysis, based on a simplified and on a high resolution micro-structural models, was conducted to evaluate the influence of material properties changes on the stress results. Both models included "a tendon zone". From the simplified model, considering a linear gradient, it appeared that the length of the tendon zone considered had a huge influence on the stress distribution and also that the gradient allowed to progressively reduce the stress concentration where it was located. In the high resolution micro-structural model, a linear and a hyperbolic gradients were tested. Their influences were quite limited: certain similitude with the simplified model were spotted, but the impact of the gradient inclusion remained limited on the stress distributions.

Our project was restrained to two-dimensional based models because it was more feasible in terms of time and hardware required. Nevertheless, a lot of perspectives are opened for three-dimensional finite element analysis. Some tests were already performed during this project on a three-dimensional low resolution model reconstructed

using the images of a low resolution μ CT scan. The preliminary results are presented in Figure 6.17. The comparison of the results obtained in two-dimensional and three-dimensional are shown for similar cross-sections in three cases of boundary conditions: 0° , 45° and 90° orientation for the force applied at the Achilles tendon (and with the 0.6 ratio force applied at the plantar fascia). As can be observed, the two sets of results match closely qualitatively, the stress concentrations at the tuberosity are retrieved and are even more visible for the three-dimensional cases. In the three-dimensional model cross-sections, the previously called "whole bone" regions seem to be even less prone to stress concentration compared to those of the two-dimensional model. Nevertheless, the two cases do not match quantitatively. Indeed, the value of stresses found in the three-dimensional model, especially at the tuberosity region, are almost twice higher than in the two-dimensional one. Using three-dimensional model is a good choice to get step closer to the reality and get more realistic quantitative data on local stresses and strains when the loading parameters and material properties have been defined using the two dimensional model. Thus, all the analyses conducted in this project could be repeated considering the two forces defined in our boundary conditions. Three-dimensional low resolution models are easy to compute and do not ask a tremendous amount of computation power and time but the micro-porosity architecture and its effect on the bio-mechanical behavior of the model are not included. On the contrary, working with a high resolution model including the detailed micro-architecture will require super computer and dedicated solver.

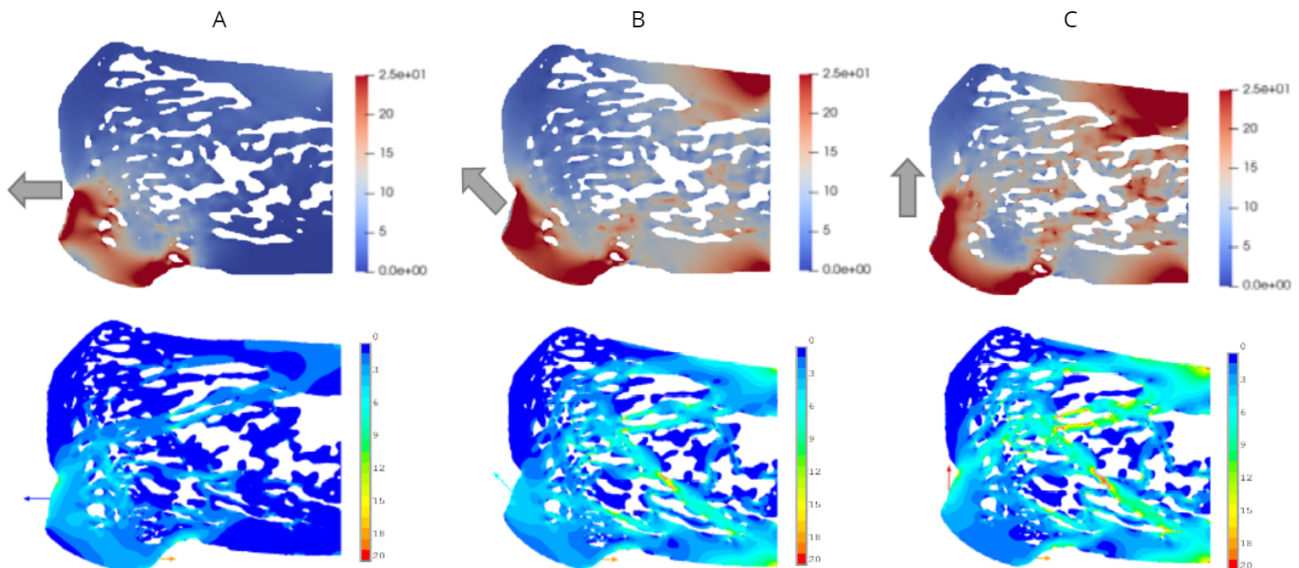


Figure 6.17: Comparison of the contour plots for the equivalent stress in three-dimensional (top) and two-dimensional (bottom) cases: (A) 180° oriented force (B) 135° oriented force (C) 90° oriented force.

Appendix

Additional results from Chapter 3

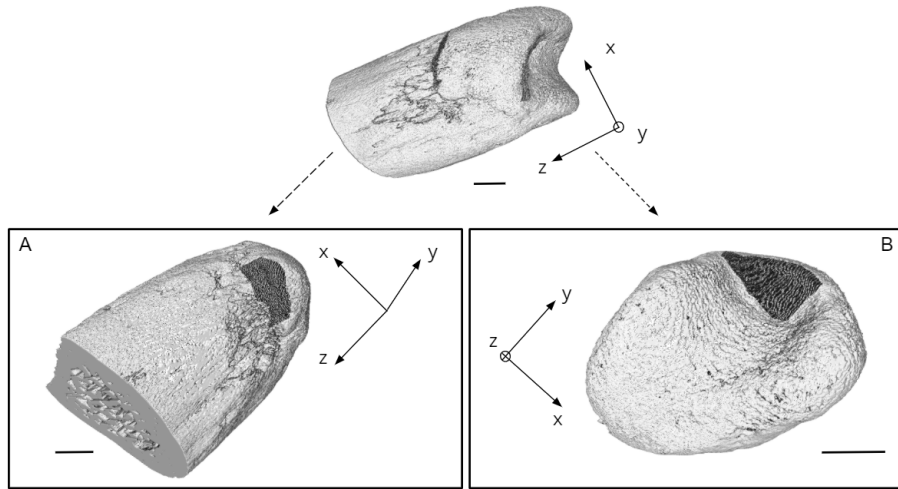


Figure 6.18: For T2 sample: Visualization of the plantar fascia (A) and Achilles tendon (B) attachment surfaces using VolumeViewer. Scale bar: 1 [mm] (*approximately*).

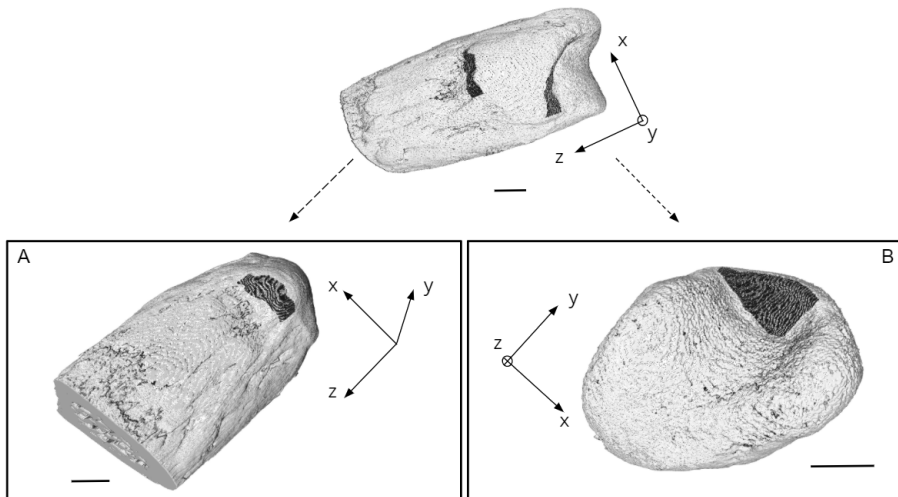


Figure 6.19: For A1 sample: Visualization of the plantar fascia (A) and Achilles tendon (B) attachment surfaces using VolumeViewer. Scale bar: 1 [mm] (*approximately*).

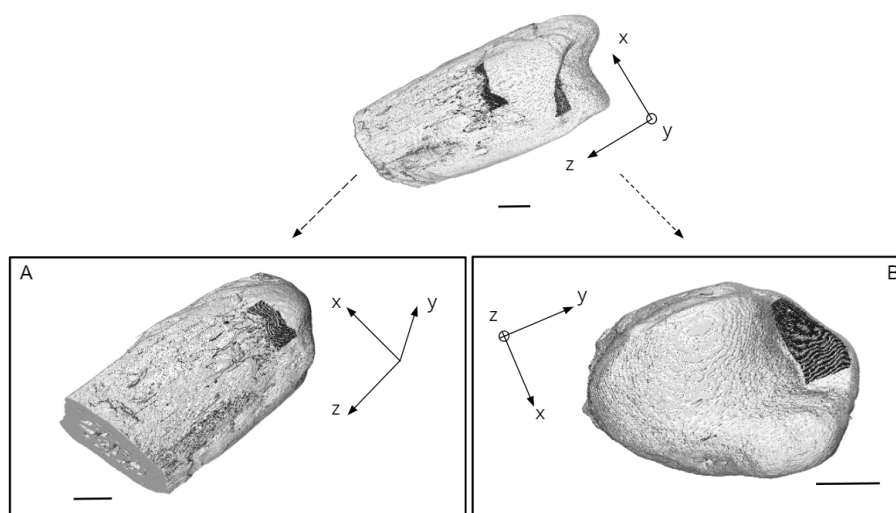


Figure 6.20: For A2 sample: Visualization of the plantar fascia (A) and Achilles tendon (B) attachment surfaces using VolumeViewer. Scale bar: 1 [mm] (*approximately*).

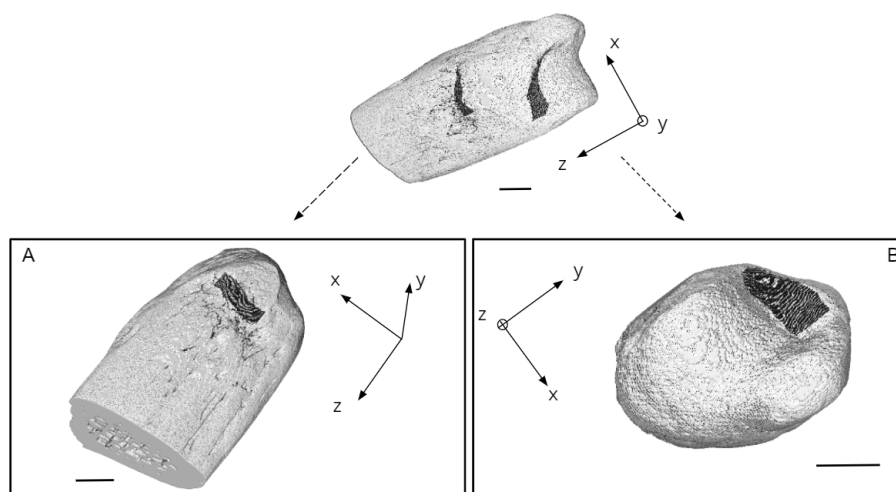


Figure 6.21: For A3 sample: Visualization of the plantar fascia (A) and Achilles tendon (B) attachment surfaces using VolumeViewer. Scale bar: 1 [mm] (*approximately*).

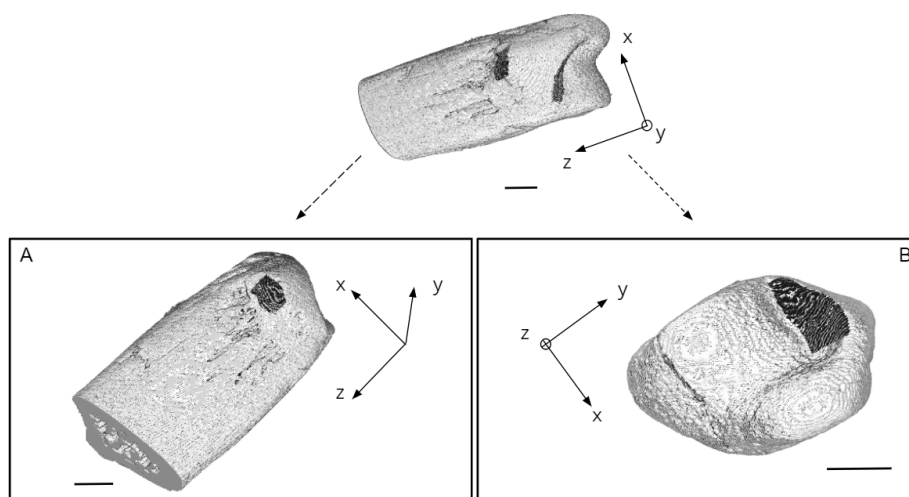


Figure 6.22: For A4 sample: Visualization of the plantar fascia (A) and Achilles tendon (B) attachment surfaces using VolumeViewer. Scale bar: 1 [mm] (*approximately*).

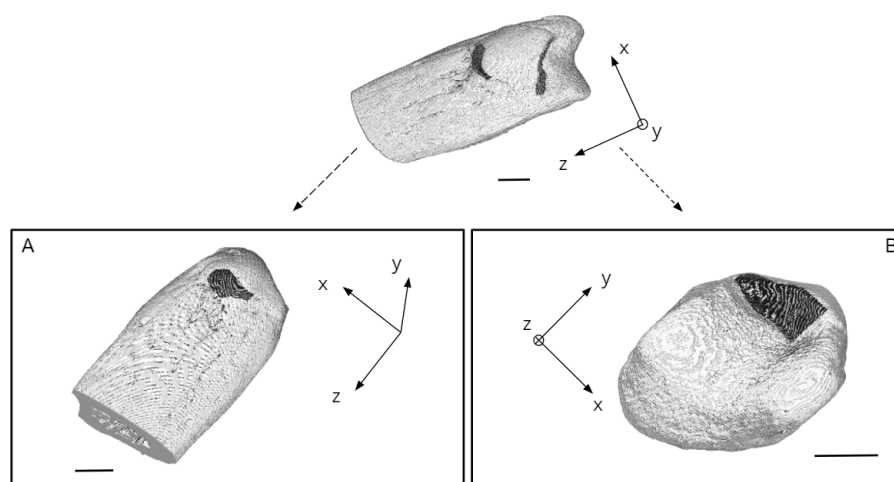


Figure 6.23: For A5 sample: Visualization of the plantar fascia (A) and Achilles tendon (B) attachment surfaces using VolumeViewer. Scale bar: 1 [mm] (*approximately*).

Sample identification	Achilles attachment surface area [mm ²]	plantar fascia attachment surface area [mm ²]
T1	0.8255	0.4928
T2	0.7616	0.5311
A1	0.8093	0.3764
A2	0.7383	0.3558
A3	0.5995	0.2408
A4	0.6602	0.2554
A5	0.7114	0.3026

Table 6.2: Results for the Achilles tendon and plantar fascia attachment surface areas ([mm²]) for seven samples available.

Bibliography

- [1] M. C. Devernejoul F. Tirode M. Nys G. Mocaer C. Morieux H. Murakami A. Barbier, C. Martel and F. Lacheretz. The visualization and evaluation of bone architecture in the rat using three-dimensional x-ray microcomputed tomography. *Journal of Bone and Mineral Metabolism*, 17, 1999.
- [2] G. M. Genin S. Thomopoulos A. C. Deymier-Black, J. D. Pasteris. Allometry of the tendon enthesis: Mechanisms of load transfer between tendon and bone. *Journal of Biomechanical Engineering*, 137, 2015.
- [3] Ansys. Ansys presentation, (accessed August 3, 2020). URL: <https://www.ansys.com/>.
- [4] H. Guo T. Su X.-Q. Fu T. Li H.-H. Cao A. K.-W. Tse Z.-Z. Wu H.-Y. Kwan A.-L. Yu B. C. Y. Cheng, H. Yu. A herbal formula comprising rosae multiflorae fructus and lonicerae japonicae flos, attenuates collagen-induced arthritis and inhibits tlr4 signalling in rats. *Scientific reports*, 6:pp. 200–242, 2016.
- [5] M. Benjamin and D. McGonagle. The anatomical basis for disease localisation in seronegative spondyloarthropathy at entheses and related sites. *Journal of Anatomy*, 199:503–526, 2001.
- [6] V. Birman, G. M. Genin, and S. Thomopoulos. Multiscale enthesis mechanics. 2015.
- [7] BMJ. Figure 9, (accessed July 20, 2020). URL: <https://ard.bmj.com/content/66/12/1553/F9>.
- [8] Team Bone. Basic biology of bone, (accessed July 20, 2020). URL: <https://teambone.com/education-basic/basic-biology-of-bone/>.
- [9] BoneJ. Moments of inertia, (accessed July 27, 2020). URL: <https://bonej.org/moments>.
- [10] A. L. Boskey. Bone composition: relationship to bone fragility and antiosteoporotic drug effects. *Bonekey Rep.*, 4:710, 2013.
- [11] A. L. Boskey. The role of osteocytes in bone remodeling. *Clin Calcium.*, 27:1697–1703, 2017.
- [12] Encyclopedia Britannica. Osteocyte, (accessed July 20, 2020). URL: <https://www.britannica.com/science/osteocyte>.
- [13] J. L. Brown, S. G. Kumbar, and C. T. Laurencin. Bone tissue engineering. *Biomaterials Science (Third Edition) An Introduction to Materials in Medicine*, pages 1194–1214, 2013.
- [14] Bruker. Skyscan-1272, (accessed July 23, 2020). URL: <https://www.bruker.com/products/microtomography/micro-ct-for-sample-scanning/skyscan-1272/learn-more.html>.
- [15] Bruker. 3d.suite software, (accessed July 31, 2020). URL: <https://www.bruker.com/products/microtomography/micro-ct-software/3dsuite.html>.
- [16] Ortho Bullets. Calcaneus fractures, (accessed July 22, 2020). URL: <https://www.orthobullets.com/trauma/1051/calcaneus-fractures>.
- [17] J. Caetano-Lopes, H. Canhao, and J. E. Fonseca. Osteoblasts and bone formation. *Acta Reumatol Port.*, 32:103–110, 2007.
- [18] B. Clarker. Normal bone anatomy and physiology. *Clinical Journal of the American Society of Nephrology*, 3:131–139, 2008.

- [19] E. Legrand M. F. Baslé D. Chappard, N. Retailleau-Gaborit and M. Audran. Comparison insight bonemeasurements by histomorphometry and ct. *Journal of Bone and Mineral Research*, 20, 2005.
- [20] E. J. Newton D. Davis, T. J. Seaman. Calcaneus fractures. *StatPearls Publishing*, 2020.
- [21] A. T. M. Phillips D. T. Zaharie. A comparative study of continuum and structural modelling approaches to simulate bone adaptation in the pelvic construct. *Applied Sciences*, 9, 2019.
- [22] A. Deymier-Black, A. Sschwartz, Z. Cai, T. Daulton, J. Pasteris, G. Genin, and S. Thomopoulos. The multiscale structural and mechanical effects of mouse supraspinatus muscle unloading on the mature enthesis. *Acta Biomaterialia*, 83, 2018.
- [23] I. Eshed, M. Bollow, D. G. McGonagle, A. I. L. Tan, C. E. Althoff, P. Asbach, and K.-G. A. Hermann. Mri of enthesitis of the appendicular skeleton in spondyloarthritis. *Annals of the Rheumatic Diseases*, 66:pp. 1553–1559, 2007.
- [24] C. Hudry F. Mathoret-Philibert M. Poussiere-T. De Chalus C. Dreuillet-F. Russo-Marie J. M. Joubert A. Sarraux F. Berenbaum, P. Chauvin. Fears and beliefs in rheumatoid arthritis and spondyloarthritis: a qualitative study. *PLoS One.*, 10, 2014.
- [25] S. D’Angelo L. Amara-K. Nicolosi E. Russo S. Naty C. Bruno-G. De Sarro I. Oliveri R. D. Grembiale F. Ursini, F. Arturi. High prevalence of achilles tendon enthesopathic changes in patients with type 2 diabetes without peripheral neuropathy. *J Am Podiatr Med Assoc* 1, 2017.
- [26] M. I. Fanuscu and T.-L. Chang. Three-dimensional morphometric analysis of human cadaver bone: microstructural data from maxilla and mandible. *Clinical Oral Implants Research*, 15, 2004.
- [27] Ankle Foot and Lower Leg Orthopedic Assessment. Ankle and lower leg anatomy, (accessed July 20, 2020). URL: <https://leassessment.weebly.com/ankle--lower-leg-anatomy.html>.
- [28] International Osteoporosis Foundation. Introduction to bone biology: all about our bones, (accessed July 21, 2020). URL: <https://www.iofbonehealth.org/introduction-bone-biology-all-about-our-bones>.
- [29] P. Fratzl and R. Weinkamer. Nature’s hierarchical materials. *Progress in Materials Science*, 52:1263–1334, 2007.
- [30] X. Yu-D.-W. Chen Y.-F. Yang B. Li-J.-Q. Zhou G.-R. Yu, Q.-J. Pang. Surgical management for avulsion fracture of the calcaneal tuberosity. *Chinese Orthopaedic Association and Wiley Publishing Asia Pty Ltd*, 5, 2013.
- [31] G. M. Genin, A. Kent, V. Birman, B. Wopenka, J. D. Pasteris, P. J. Marquez, and S. Thomopoulos. Functional grading of mineral and collagen in the attachment of tendon to bone. *Biophysical Journal*, 97:976–985, 2009.
- [32] X. E. Guo and S. A. Goldstein. Vertebral trabecular bone microscopic tissue elastic modulus and hardness do not change in ovariectomized rats. *Journal of Orthopaedic Research*, 18:333–336, 2000.
- [33] D. J. Hadjidakis and I. I. Androulakis. Bone remodeling. *Annals of the New York Academy of Sciences*, 1092:385–396, 2006.
- [34] Northern Arizona Healthcare. Foot and ankle issues, (accessed July 20, 2020). URL: <https://www.nahealth.com/orthopedic-services/foot-and-ankle-issues>.
- [35] Healthline. Calcaneus, (accessed July 20, 2020). URL: <https://www.healthline.com/human-body-maps/calcaneus-bone#1>.
- [36] Healthline. Plantar aponeurosis, (accessed July 20, 2020). URL: <https://www.healthline.com/human-body-maps/plantar-aponeurosis#1>.
- [37] Ideadigezt. Foot x-ray exam: What to expect, (accessed July 20, 2020). URL: <https://www.ideadigezt.com/foot-x-ray-exam-what-to-expect/>.

- [38] ImageJ. Imagej, (accessed July 27, 2020). URL: <https://imagej.net/Welcome>.
- [39] C. R. Dwyer-R. P. Russell J. H. Weinreb F. Alaei-K. Beitzel M. B. McCarthy M. P. Cote A. D. Mazzocca J. Apostolakos, T. J. Durant. The enthesis: a review of the tendon-to-bone insertion. *Muscles, ligaments and tendons journal*, 4:pp. 333–342, 2014.
- [40] J. S. Day J. H. Waarsing and H. Weinans. An improved segmentation method for in vivo ct imaging. *Journal of Bone and Mineral Research*, 19, 2004.
- [41] L. A. Feldkamp R. W. Goulet J. L. Kuhn, S. A. Goldstein and G. Jesion. Evaluation of a microcomputed tomography system to study trabecular bone structure. *Journal of Orthopaedic Research*, 8, 1990.
- [42] S. Fish R. Müller T. Uchiyama G. Gronowicz M. Nahounou Q. Zhao D. W. White M. Chorev D. Gazit J. M. Alexander, I. Bab and M. Rosenblatt. Human parathyroid hormone 1-34 reverses bone loss in ovariectomized mice. *Journal of Bone and Mineral Research*, 16, 2001.
- [43] J.P.Ponthot. An introduction to finite element method. chapter 1: introduction, 2016.
- [44] L. L. Lempainen T. Laitala-Leinonen S. Orava K. J. Johansson, J. J. Sarimo. Calcific spurs at the insertion of the achilles tendon: a clinical and histological study. *Muscles Ligaments Tendons J.*, 2:273–277, 2013.
- [45] KENHUB. Fibrocartilage, (accessed August 15, 2020). URL: <https://www.kenhub.com/en/library/anatomy/fibrocartilage>.
- [46] Berkeley Lab. The toughness of bone, (accessed July 20, 2020). URL: <https://newscenter.lbl.gov/2008/08/06/the-toughness-of-bone/>.
- [47] D. Latt, D. Jaffe, Y. Tang, and M. Taljanovic. Evaluation and treatment of chronic plantar fasciitis. *Foot Ankle Orthopaedics*, 5, 2020.
- [48] M. A. Liebschner. Biomechanical considerations of animal models used in tissue engineering of bone. *Biomaterials*, 25:1697–1714, 2004.
- [49] Lumen. Bone and calcium, (accessed July 21, 2020). URL: <https://courses.lumenlearning.com/boundless-ap/chapter/bone-and-calcium/>.
- [50] K. Davies M. Akhter, J. Lappe and R. Recker. Transmenopausal changes in the trabecular bone structure. *Bone*, 41, 2007.
- [51] J. R. Ralphs G. Bydder T. M. Best S. Milz M. Benjamin, H. Toumi. Where tendons and ligaments meet bone: attachment sites ('entheses') in relation to exercise and/or mechanical load. *J Anat.*, 208:471–490, 2006.
- [52] R. G. Golele M. Radzilani, E. D'Alton. Avulsion fracture of the calcaneal tuberosity: A soft tissue complication from delayed treatment. *The Foot and Ankle Online Journal.*, 3, 2010.
- [53] F. Madehkhaksar, Z. Luo, N. Pronost, and A. Egges. *Modeling and Simulating Virtual Anatomical Humans*, pages 137–164. 2014.
- [54] J. Maquirriain. Achilles tendon rupture: Avoiding tendon lengthening during surgical repair and rehabilitation. *Yale Journal of Biology and Medicine*, 2011.
- [55] Mathworks. Delaunay, (accessed July 28, 2020). URL: <https://nl.mathworks.com/help/matlab/ref/delaunay.html>.
- [56] Mathworks. What is matlab?, (accessed July 28, 2020). URL: <https://nl.mathworks.com/discovery/what-is-matlab.html>.
- [57] Mathworks. Working with delaunay triangulations, (accessed July 28, 2020). URL: <https://nl.mathworks.com/help/matlab/math/delaunay-triangulation.html>.

- [58] Mathworks. Volume viewer, (accessed July 31, 2020). URL: <https://nl.mathworks.com/help/images/ref/volumeviewer-app.html>.
- [59] MedicalNewsToday. What to know about enthesopathy, (accessed July 22, 2020). URL: <https://www.medicalnewstoday.com/articles/318987#what-are-the-symptoms-of-enthesopathy>.
- [60] MedicineNet. Heel spurs, (accessed July 22, 2020). URL: https://www.medicinenet.com/heel_spurs/article.htm.
- [61] A. L. Mescher. *Junqueira's Basic Histology: Text and Atlas 15th Edition*. McGraw-Hill Education, New-York, 2018.
- [62] L. Vico E. Dolleans D. Courteix N. Bonnet, N. Laroche and C. L. Benhamou. Assessment of trabecularbone microarchitecture by two different x-ray microcomputed tomographs: A comparative study of the rat distal tibiausing skyscan and scanco devices. *Medical Physics*, 36, 2009.
- [63] J. Williams Chiropractic Dee Why NSW. Plantar fasciitis rehab, (accessed July 20, 2020). URL: <http://jakewilliamschiro.com/2019/09/02/plantar-fasciitis-rehab/#comment-3>.
- [64] M. Öncü O. Beytemür. The age dependent change in the incidence of calcaneal spur. *Acta Orthop Traumatol Turc.*, 2018.
- [65] Ludwig Boltzmann Institute of Osteology. Quantitative backscattered electron imaging (qbei), (accessed August 15, 2020). URL: <https://www.osteologie.at/index.php/14-research/105-quantitative-backscattered-electron-imaging-qbei>.
- [66] OrthoInfo. Calcaneus (heel bone) fractures, (accessed August 15, 2020). URL: <https://orthoinfo.aaos.org/en/diseases--conditions/calcaneus-heel-bone-fractures/>.
- [67] P. Fratzl P. Roschger, E. P. Paschalis and K. Klaushofer. Bone mineralization density distribution in health and disease. *Bone*, 42, 2008.
- [68] J. Kurths G. Beller P. Saporin, J. S. Thomsen and W. Gowin. Segmentation of bone ct images and assessment of bone structure using measures of complexity. *Medical Physics*, 33, 2006.
- [69] Physiopedia. Avulsion fractures of the ankle, (accessed August 15, 2020). URL: https://www.physio-pedia.com/Avulsion_Fractures_of_the_Ankle.
- [70] B. V. Damme G. V.Derperre J. Dequeker T. Hildebrand R. Müller, H. V. Campenhout and P. Rügsegger. Morphometric analysis of human bone biopsies: A quantitative structural comparison of histological sections and micro-computed tomography. *Bone*, 23, 1998.
- [71] T. E. Khassawna G. Schlewitz B. Hürter W. Böcher M. Bobeth A. C. Langhereinrich C. Heiss A. Deutsch R. Müller, M. Kampschulte and G. Cuniberti. Change of mechanical vertebrae properties due to progressive osteoporosis: combined biomechanical and finite-element analysis within a rat model. *Medical Biological Engineering Computing*, 52:405–414, 2014.
- [72] A. T. Azizi V. Vijay R. Vaishya, A. K. Agarwal. Haglund's syndrome: A commonly seen mysterious condition. *Cureus...*, 8, 2016.
- [73] Radiopaedia. Lover's fracture, (accessed August 15, 2020). URL: <https://radiopaedia.org/cases/lovers-fracture-2#:~:text=Lover's%20fracture%20is%20a%20type,from%20the%20lover's%20spouse%20>.
- [74] L. Rossetti, L. Kuntz, E. Kunold, J. Schock, K. Müller, H. Grabmayr, F. Pfeiffer, S. Sieber, R. Burgkart, A. Bausch, and J. Stolberg-Stolberg. The microstructure and micromechanics of the tendon-bone insertion. *Nature Materials*, 16:pp. 664–670, 2017.
- [75] W. Roux. Gesammelte abhandlungen. *Monatshefte für Mathematik und Physik*, 25, 1914.
- [76] D. Ruffoni. Biomechanics, (2016).

- [77] Iowa State University: Materials Science and Engineering. Backscattered electrons, (accessed August 15, 2020). URL: <https://www.mse.iastate.edu/research/sem/microscopy/how-does-the-sem-work/high-school/how-the-sem-works/backscattered-electrons/>.
- [78] Blue Scientific. Bruker micro-ct software – new features of ct-analyser (ctan), (accessed July 28, 2020). URL: <https://www.blue-scientific.com/bruker-micro-ct-software/>.
- [79] A. Sharir, M. Barak, and R. Shanar. Whole bone mechanics and mechanical testing. *Veterinary journal (London, England : 1997)*, 177:8–17, 2008.
- [80] Sports-Health. surgery for insertional achilles tendinopathy, (accessed July 22, 2020). URL: [https://www.sports-health.com/blog/when-heel-pain-caused-bone-spurs#:~:text=Bone%\\$20spurs%\\$20can%\\$20be%\\$20treated,spur%\\$20in%\\$20the%\\$20first%\\$20place.](https://www.sports-health.com/blog/when-heel-pain-caused-bone-spurs#:~:text=Bone%$20spurs%$20can%$20be%$20treated,spur%$20in%$20the%$20first%$20place.)
- [81] Adelaide Ankle Surgery. Achilles speedbridge, (accessed August 15, 2020). URL: [https://www.adelaideankle.com.au/achilles-speedbridge#:~:text=See%\\$20Achilles%\\$20Tendinopathy%\\$20under%\\$20the,months%\\$20of%\\$20non%\\$20surgical%\\$20treatment.](https://www.adelaideankle.com.au/achilles-speedbridge#:~:text=See%$20Achilles%$20Tendinopathy%$20under%$20the,months%$20of%$20non%$20surgical%$20treatment.)
- [82] S. L. Teitelbaum. February 2007.
- [83] A. Tits. Where tendons meet bones: structural and mechanical analysis of achilles tendon insertion into calcaneus, 2018.
- [84] C. Turner. Three rules for bone adaptation to mechanical stimuli. *Bone*, 23, 1998.
- [85] Washington State University. Lab 3: Cartilage bone, (accessed August 15, 2020). URL: <https://undergraduate.vetmed.wsu.edu/courses/vph-308/histology/lab-3-histology-cartilage/cartilage-fibrocartilage.>
- [86] A. Wang. Haglund’s deformity, (accessed July 20, 2020). URL: <http://evergreenfootankle.com/foot-problems/common-problems/haglunds-deformity/>.
- [87] WebMD. Picture of the achilles tendon, (accessed July 20, 2020). URL: <https://www.webmd.com/fitness-exercise/picture-of-the-achilles-tendon#1.>
- [88] WebMD. Enthesopathy and enthesitis, (accessed July 22, 2020). URL: <https://www.webmd.com/arthritis/psoriatic-arthritis/enthesitis-enthesopathy.>
- [89] Wikipedia. Calcaneus, (accessed July 20, 2020). URL: https://en.wikipedia.org/wiki/Achilles_tendon.
- [90] Wikipedia. Long bone, (accessed July 20, 2020). URL: https://en.wikipedia.org/wiki/Long_bone.
- [91] J. Wolff. Das gesetz der transformation der knochen. *DMW - Deutsche Medizinische Wochenschrift*, 1893.
- [92] A. Deymier-Black A. G. Schwartz S. Thomopoulos G. M. Genin Y. Hu, V. Birman. Stochastic interdigitation as a toughening mechanism at the interface between tendon and bone. *Biophysical Journal*, 108:431–437, 2015.